Vaal University of Technology

Your world to a better future

VUT

Adsorption of Cr(VI) by iron oxide functionalized polyethyleneimine (PEI) coated activated carbon-silica composites

A dissertation submitted to the Faculty of Applied and Computer Sciences, Department of Chemistry, Vaal University of Technology, Vanderbijlpark, in fulfilment of the requirements for the degree of **Magister Technologiae**

By

Mpho Cynthia Qhubu

Supervisor: Prof V.E Pakade

Co-supervisor: Prof P.N Nomngongo

DECLARATION

I declare that this dissertation is rightfully mine and was composed by myself being submitted for the first time for the Magister Technologiae Degree to the Department of Chemistry, Vaal University of Technology, Vanderbijlpark and has not been submitted before for any degree or examination to other universities.

……..

Candidate signature

…14th….. day of …December 2020……

ABSTRACT

Water scarcity due to limited resources and pollution of the little available water by organic and inorganic contaminants remains as one of the critical issues of the 21st century. Several treatment methods have been developed, with some being used successfully at industrial scale but many challenges including secondary sludge generation, high operation costs, high maintenance costs and high energy input were observed. In this study, the adsorption process was explored as an effective means for the removal of Cr(VI) ions from aqueous solution due to its economic feasibility and use of abundantly available adsorbents. Amongst the many available adsorbents, this work focused on exploring functionalized activated carbons (ACs) as adsorbents for Cr(VI) ions due to their favorable adsorption characteristics which involve large surface area, high porosity, and high radiant stability. The iron oxide functionalized polyethyleneimine activated carbon-silica composites were prepared through co-precipitation of Fe(II) and Fe(III) over *Macadamia* activated carbon to form the AC-Fe_3O_4 co-shell which was reacted with tetraethylorthosilicate (TEOS) and the polyethyleneimine (PEI). The different adsorbents prepared were labelled AC-Fe_3O_4, AC-Fe_3O_4-SiO_2 and AC-Fe_3O_4-SiO_2-PEI. The adsorbents were further characterized using elemental analysis (CHNS), thermo gravimetric analysis (TGA), scanning electron microscopy (SEM), energy dispersive spectroscopy (EDS), Fourier transform infrared (FTIR) spectroscopy, Brunauer-Emmett-Teller (BET), transmission electron spectroscopy (TEM), X-ray diffraction (XRD) and X-ray photoelectron spectroscopy (XPS). FTIR displayed successful attachment of Fe_3O_4 and SiO_2 with bands at 404 and 786 cm^{-1} being assigned to the asymmetric vibration of Fe-O and Si-O-Si while the asymmetric stretch of Si-OH is observed at 1066 cm^{-1}. XRD showed the presence of magnetite particles in the adsorbents confirmed by the JCPDS 00-019-0629. EDS revealed the presence of Fe, Si, and N atoms which can relate to successful incorporation of the desired functional groups.

Each of these materials were evaluated for their Cr(VI) ion removal through batch adsorption experiments where one parameter at a time was varied while all others were fixed. The parameters investigated included the effect of pH, contact time, initials Cr(VI) concentration, adsorbent dosage concentration and temperature. The optimum conditions were obtained at pH 3, initial concentration 2.5 mg/L, contact time of 120 min for AC-Fe_3O_4-SiO_2-PEI. The optimization of each parameter was done in order to determine the conditions in which the adsorbents work best in the uptake of Cr(VI). All the three studied adsorbents showed acceptable adsorption performance for the removal of Cr(VI) from aqueous solutions. Adsorption isotherms studied confirmed that the adsorption data in all the three adsorbents fitted well into the Langmuir isotherm, demonstrating a homogeneous monolayer coverage. Regarding the kinetic studies, the adsorption data were best described by the pseudo-second order rate model with R^2 values of 0.974, 0.974 and 0.962 for AC-Fe_3O_4, AC-Fe_3O_4-SiO_2 and AC-Fe_3O_4-SiO_2-PEI, respectively. The adsorption capacity observed from the present study (6.62, 3.92 and 5.48 for AC-Fe_3O_4, AC-Fe_3O_4-SiO_2 and AC-Fe_3O_4-SiO_2-PEI, respectively) were satisfactory and suitable as compared to those reported in literature. Thermodynamics data of the adsorption processes revealed a feasible spontaneous endothermic adsorption process which also confirmed that the reaction process occurred through chemisorption.

DEDICATION

I dedicate this work to all the young women in the world who are still trying to figure out life and finding their passion and purpose in life. May this be a sign that when you put your faith in God and keep your eyes on the prize, you will prosper. One step at a time.

ACKNOWLEDGEMENTS

Your mercy, your kindness, your protection, your strength, your love, and your blessings towards me Lord, I can never thank you enough. It is by your grace and not by our own that we are able to do all things and achieve all things.

To my supervisors, Prof V.E Pakade and Prof P.N Nomngongo, I am thankful for your valued opinions and expertise. I would also like to thank you for your guidance, for your patience and support throughout these years. You have equally played a mother and fatherly figure.

My extended gratitude to the National Research Foundation and the Vaal University of Technology for funding my studies.

To Mahadi Lesaoana, thank you so much for your inputs and opinions to this work and for your support both personally and professionally. Words can never be enough to express my gratitude, thank you.

I would like to extend my gratitude to Mr P. Ngoy for assisting me constantly with instrumentation, your efforts and inputs are highly appreciated.

To my mom and dad, thank you so much for your love and support and for your constant prayers and words of encouragements. To Papa and abuti Molefi, thank you for crushing my activated carbon, without you, there wouldn't be any adsorbents.

To Nkgono Maneo, Ntate Dichaba and Mama, thank you for welcoming me in your homes and constantly driving me to campus daily. I am grateful for the love that you have shown me constantly. To the rest of my family, the Khetsis', the Miyas', Dichaba Junior, Khibas' and Qhubus', thank you so much for your constant support and prayers. If it were not of your support and your love, I would have quit a long time ago.

I would love to extent my gratitude to Likeleli Khunyeli, mostly for everything. You have been nothing but an amazing friend. Thank you for accommodating me in your home and for making sure that I get to campus (UJ DFC) safely every day.

To my friend, Zoleka Nqaba, thank you for being you. Thank you for crying with me and laughing with me. Thank you for not only being a friend but also a partner in research.

To my C108 colleagues, thank you for all your efforts and your support, I appreciate you. Lab 3404, thank you so much for accommodating me and making me feel at home. But mostly, thank you for the lunch hour breaks which were filled with laughter. The memories live forever.

To Silindokuhle and Raphael, thank you so much for your kindness and for your constant assistance when needed, may God bless you.

To every researcher and supervisor, especially the NCAP group, I would like to extend my gratitude towards your inputs and opinions. It really takes the whole village to raise a child. Thank you.

TABLE OF CONTENTS

LIST OF FIGURES

LIST OF TABLES

LIST OF ABBREVIATIONS AND ACRONYMS

AAS	Atomic absorption spectroscopy
AC	Activated carbon
BET	Brunauer Emmett and Teller
CHNS	Carbon, hydrogen, nitrogen, and sulfur
DME	Dispersive microextraction
DMF	*N'N*- Dimethylformamide
DPC	1,5'- Diphenyl carbazide
DTA	Derivative thermogravimetric analysis
EA	Elemental analysis
EDS	Energy dispersive spectroscopy
FTIR	Fourier-transform infrared
GPS	3-Glycidoxypropyltrimethoxysilane
IC	Ion chromatography
ICP-OES	Inductive coupled plasma optical emission spectroscopy
MNAC	*Macadamia* nutshell activated carbon
PEI	Polyethyleneimine
PFO	Pseudo first order
PSO	Pseudo second order
SEM	Scanning electron microscopy
SPME	Solid phase microextraction
TGA	Thermogravimetric analysis
UV-Vis	Ultra-violet-visible spectroscopy
VSM	Vibrating sample magnetometer
XRD	X-ray diffraction

CHAPTER 1:
INTRODUCTION

1.1 BACKGROUND

About 1 billion people do not have access to safe consumable water with about 2 million death yearly reported by the World Health Organization attributed to drinking unsafe water (Bai et al., 2013). The little water present on earth's surface is exposed to pollution. Water pollution is being a global concern due to an increase in urbanization. The main cause of water pollution is the discharge of pollutants into water streams. Chemical water pollution is caused by organic and inorganic compounds seepage to water sources from various industries. On one hand, organic compounds can be degraded under proper conditions but metal ions on the other hand are non-biodegradable and toxic to humans and the environment. Also, trace metals are highly soluble and can easily be absorbed by living cells due to their bio-accumulative nature (Roozbeth et al., 2013).

Chromium forms part of the most hazardous metals to human health listed by the U.S Environmental Protection Agency (USEPA). Chromium compounds are introduced into the environment through chrome mining, electroplating, leather tanning, paint and dye manufacturing, natural volcanic activities, and weathering of rock (Niebuhr et al.,1988; Kowalski et al.,1994). Chromium is an oxyanion metal ion that exists in several oxidation states such as +2 ,+3, and +6. The trivalent chromium (Cr(III)) and hexavalent chromium (Cr(VI)) are the two most stable states of chromium. In aqueous media, hexavalent chromium exists in various forms according to the pH level and redox potential. These forms are chromate ($Cr_2O_4^{2-}$), hydro chromate ($HCrO_4^-$) or dichromate ($Cr_2O_7^{2-}$).

Hexavalent chromium is reported to be the most toxic and known to be a Group A carcinogen causing chronic effects in cases of long term exposure, while the trivalent chromium is a micronutrient required for glucose metabolism in mammals (Jaouadi et al., 2017). It, therefore, shows that the two chromium species need to be handled differently. Due to toxicity associated with Cr(VI), it is important for industrial operations to remove or treat chromium(VI) before being discharged into water streams (Yu et al., 2018, Wang et al., 2020b). The South African National Standards (SANS) have set a limit of < 50 mg/L for Cr(VI) in domestic water (SANS 251:2015). The World Health Organization (WHO) on the other hand has set a standard of 0.05 mg/L for the tolerance of Cr(VI) in drinking water and 0.02 mg/L in soil samples (Singh and Prasad, 2019). The National Institution of Occupational Safety and Health has set a tolerance of 10^{-3} mg/m^3 of chromium in water (Adio et al., 2019). Most reported processes focused on removal of Cr(VI) at high initial concentrations (100 to 600 mg/L) and at lower initial concentrations (<20 mg/L) (Adio et al 2019). Bearing in mind the tolerance of Cr(VI) in consumable water and in surface water, the removal processes should have the capacity to remove Cr(VI) at dilute concentrations (<10 mg/L) and above 100 mg/L.

Many physicochemical methods have been studied for the removal of Cr(VI) from aqueous solutions, namely chemical precipitation (Roozbeth et al., 2013), chemical oxidation (Li et al., 2013), ion exchange (Liu et al., 2018), membrane separation (Lawrence Arockiasamy et al., 2017), reverse osmosis (Mnif et al., 2017) as well as electrodialysis (dos Santos et al., 2019). However, these methods are regarded as ineffective due to their high costs, high amount of energy input, generation of toxic secondary sludge which is expensive to dispose and not eco-friendly to the nature (Parlayici et al., 2015, Pakade et al., 2016a).

Adsorption has gained popularity in the removal of Cr(VI) from aqueous solution amongst other methods due to its low cost effectiveness, simplicity of operation, moderate to high adsorption capacities and no secondary pollution generation (Liu et al., 2019a).

Activated carbon is a form of carbon material produced through pyrolysis of biomass material and used in adsorption processes and chemical reactions for removal of chromium (VI). High porosity, high surface area and well-defined microporous structure are some of the properties that make AC superior to other adsorbents (Betzy and George, 2015). Producing a cost-effective activated carbon is one of the main challenges in commercial manufacturing (Betzy and George, 2015). Studies have been carried out to get precursor-sources that will produce AC of good quality. Mainly waste from agricultural activities or sources have received more prominence due to their low cost and available abundance. These agricultural waste materials include chestnut oak shells (Niazi et al., 2018), *Aegle Marmelos* fruit shells (Gottipati and Mishra, 2016), candlenut shell (Taslim et al., 2018), coffee waste (Sunganya and Kumar 2018), medlar seeds (Solgi et al., 2017), mango kernel (Rai et al., 2016), rice straw (Zhang et al., 2018), aloe vera waste leaves (Prajapati et al., 2020), palm shell (Owlad et al., 2010), *Macadamia* nutshells (Hlungwane et al., 2017) among others.

The use of different organic precursors in the preparation of the activated carbon affects the structure and surface of the activated carbon which in turn affects its reactivity as an adsorbent (Lesaoana et al., 2019). Therefore, further improvements on the surface of the adsorbent is required for better sorption capacities and reactivity. The improvements maybe done through pre-treatment or impregnation methods for instance, immersion of AC in activating reagents such as acids, bases, and salt solutions. This can be done in conjunction with heating of adsorbents at elevated temperatures or just at ambient temperatures. In this way the physical and chemical properties of the adsorbents are improved. Because AC are hydrophobic, these

treatment methods often introduce oxygenated functional groups on its surface which then usher a platform for further functionalization (Liang et al., 2017). That is, functionalization introduces heteroatoms to AC surface. Besides the introduction of heteroatoms through pre- and post-treatment, functionalization can improve physical properties like surface area, porosity, and particle size. Methods widely used for separation include filtration and sedimentation (Fatehi et al. 2017). The use of magnetic separation has been gaining attention due to its properties such as an applied magnetic field, high speed, and simplicity (Fatehi et al., 2017). Therefore, magnetic properties are induced on the surface of the activated carbon through co-precipitation of Fe(II) and Fe(III). However, magnetite suffer from instability under ambient conditions and various acidic media due to their high oxidation property (Ta et al., 2016). Support materials are therefore required to protect the magnetite from oxidization and to maintain individual particle stability on its surface. The support materials can be inorganic material such as silica, alumina, chitosan and other ligands with favorable properties such as stability at acidic media, inert to redox reactions and high content of hydroxyl groups on their surfaces allowing functionalization and binding of various ligands to occur easily (Ta et al., 2016).

The use of amino-functionalized AC for improved sorption capacities also serves as one of the support materials in place. These amino functionalized materials are mostly polymers such as polyethyleneimine (PEI), polypyrrole (PPy), polyaniline (PANI), polyamidoamine (PAMA) etc. (Jiang et al., 2018b). These polymers are mostly employed due to their ease of synthesis property, low costs, environmental stability, and regeneration. Their high content of primary and secondary amine groups allows them to adsorb heavy metal ions easily through electrostatic interaction and hydrogen bonding (Jiang et al., 2018b). This in turn results in high adsorption capacities and removal efficiencies of heavy metals including Cr(VI). Also, the

amine groups serve as electron donors that reduce Cr(VI) to less toxic Cr(III) (Liu et al., 2019a). In the present study, PEI compound was grafted on the surface of the magnetic silica coated activated carbon to increase the electrostatic interaction, hydrogen bonding and effective removal of Cr(VI) by the adsorbent.

1.2 JUSTIFICATION

Activated carbon has received wide-spread application in the removal of contaminants from aqueous solutions due to its large surface area and well-defined porous structure. However, commercially activated carbon is expensive and generally employed for the adsorption of organic compounds owing to the hydrophobicity of the pristine activated carbon. The hydrophobicity is due to the high carbon content (about 80%) and the lack of hydrogen bond forming atoms (O, N, H). Even though the hydrophobic nature serves as an advantage for the mitigation of nonpolar organic compounds, it is detrimental for the removal of hydrophilic species like heavy metals. Hence, oxidative secondary treatment methods are used to introduce oxygenated functional groups including -C-O, -C=O, O=C-O to improve the water retention of activated carbons as well as usher platforms for further functionalization such as grafting of specific ligands.

CHAPTER 2:
LITERATURE REVIEW

2.0 SUMMARY

This chapter gives a background review on how chromium is introduced into the environment and its toxicity in general. It also gives a description of what has been done in literature regarding the removal of chromium (VI) by comparing several methods. Detailed descriptions of the adsorption processes, preparations, and modifications of the adsorbents for the removal of Cr(VI) are given.

2.1 ORIGIN OF CHROMIUM

Chromium is one of the most abundant heavy transitional metal on the earth's crust. It has an atomic number of 24 with several oxidation states, but the trivalent and hexavalent forms are the most stable states which are mostly important in the environment and commercialization of products. Trivalent chromium is found in rocks, plants, and soil (Pakade et al., 2016). It is mostly employed as a micronutrient used for glucose and lipid membrane metabolism in mammals by breaking down and storing of fats for energy (Sethy and Sahoo, 2019). Hexavalent chromium on the other hand is introduced to the environment through discharges or leakages from industrial activities such as electroplating, pigment manufacturing, leather tanning, mining and smelter operations (Sethy and Sahoo, 2019).

Hexavalent chromium is more mobile and highly soluble in water as compared to trivalent chromium (Zhang et al., 2018). The mostly known species of Cr(VI) are dichromate ($Cr_2O_7^{2-}$), hydrogen chromate ($HCrO_4^-$) and chromate (CrO_4^{2-}) (Cai et al., 2018; Pakade et al., 2016; Zhang et al., 2018; Sethy and Sahoo, 2019) .

2.2 TOXICITY OF CHROMIUM

Cr(VI) is well-known for its carcinogenic and mutagenic properties, whereas Cr(III) is less toxic and used as a micronutrient. Exposure to Cr(VI) is mainly through inhaling and skin contact during industrial operations through fumes and mists (Gottipati and Mishra, 2016). Although Cr(III) is known to be less toxic, its high concentrations have been related to be harmful effects that include, damages to the red blood cells, DNA's and suppressions to the immune system (Lesaoana et al., 2019). Cr(III) has been reported to have the capacity to oxidize to toxic Cr(VI) facilitated by the presence of manganese (Kononova et al., 2019). Inhaling Cr(VI) may cause nasal suppression affecting sinuses, irritation to eyes and respiratory problems such as asthma. Effects such as, rashes, severe burns, and poisoning can be related to skin irritation. Oral ingestion may result in vomiting, ulcers, abdominal pains, indigestions and diarrhea (Gottipati and Mishra, 2016).

2.2 REMOVAL METHODS OF Cr(VI)

There are several methods that are put in place for the removal of Cr(VI) from aqueous solutions. Ion exchange, membrane separation, chemical precipitation, adsorption, and reverse osmosis are discussed as follows.

2.2.1 Ion exchange

Ion exchange processes can be defined as the exchange of ions between a solid and a liquid phase in a reversible manner aiming to separate ionic contaminants from solution (Richardson et al., 2002). In this process, ionic species from one liquid phase are transferred to another through a solid resin. The analyte's ions are concentrated on the resin while the adsorbing ions are released into the solution (Dizge et al., 2009). Adsorbents commonly used include cross-linking polymers called resins. The resins used as ion exchangers have been reported to have advantages that surpass other sorbents which include mechanical strength, osmotic stability,

regeneration ability and high exchange capacities (Kononova et al., 2015). The solid, insoluble resins also need to be able to adsorb positively or negatively charged ions from the electrolyte solution and release ions equivalently to the solution. It has also been reported that creating long-chained cross-linked agents' resins have resulted in high ionic permeability due to the elasticity of their structure (Kononova et al., 2015).

The ion exchangers can be cationic such as hydrogen or sodium ions exchanging with positively charged ions such as Ni^{2+}, Cu^{2+} or Zn^{2+} or can be negatively charged ions such as hydroxyl and chloride which can be replaced by negatively charged ions such as sulfates, nitrates, chromates etc. Ion exchange has a few downfalls such as fouling of the resins, use of external forces such as heating to maximize efficiencies, ineffective removal of particles and high costs requirements (Gottipatti et al., 2012). The swelling of the polymeric skeleton due to weak mechanical strength make exchange resins to have low selectivity (Rad et al., 2009).

2.2.2 Membrane separation

Membrane separation involves trapping of metal ions on a partially permeable membrane. The separation selectivity depends solely on the type of membrane employed. Different membrane separation processes include, microfiltration (MF), nanofiltration (NF), ultrafiltration (UF) and reserve osmosis (RO) (Kucurek et al., 2014). Table 2.1 displays specifications of the mentioned techniques. Microfiltration and ultrafiltration are mainly used in pre-treatment methods and in the removal of suspended solids, colloids, bacteria, viruses etc. (Kucurek et al., 2014). Nanofiltration and reverse osmosis have a similar principle, however, nanofiltration possesses lower separation effects compared to reverse osmosis (Kucurek et al., 2014). Corazza et al. (2012) employed multi-walled nanotubes for the removal of Cr(VI). It was observed that 95 to 99% of Cr(VI) was removed at pressures of 20, 30 and 90 psi implying no significant effect on removal as pressure changed. However, the permeate flux decreased with an increase in

pressure which mostly results in membrane fouling. In the study by Rad et al. (2009) reverse osmosis membrane was employed and there was an increase in removal percentages with an increase in pressure flow. This implies that reverse osmosis depends on high pressure flow. Membrane separation techniques are disadvantaged due to fouling of the membrane, mostly high-pressure flows are required, high maintenance costs, low chemical, and thermal stability (Gottipatti et al., 2012).

Table 2.1: Pressure-driven membrane separation process (Kucurek et al., 2014)

Separation process	Particle size	Operating pressure
Microfiltration	>0.1 μm	<500 kPa
Ultrafiltration	10-100nm	500-1000 kPa
Nanofiltration	1-10 nm	1-4 MPa
Reverse osmosis	0.1-1 nm	3-10 MPa

2.2.3 Chemical precipitation

Chemical precipitation involves formation of a solid substance (precipitate) and using it for removal of heavy metal ions in solution. For example, silver ions from a soluble ion such as silver nitrate are precipitated by adding ions such as chlorides (sodium chloride). When these two ions combine, they form an insoluble silver chloride (Augustyn et al., 1998). This method depends on the pH of the solution, the temperature applied, and the precipitation agents added (Tarooq et al., 2010). Ramakrishnaiah and Prathima (2016) compiled a study of removal of Cr(VI) through chemical precipitation. The Cr(VI) was first reduced to a less toxic Cr(III) using sodium metabisulphite then precipitating agents (sodium hydroxide, calcium hydroxide and polymer MF 207) were used to form the precipitate. About 99.7% of the Cr(III) was removed. Although the method has been reported to be effective in removing Cr(VI) and immobilization

of Cr(III), it also has a downfall of generating large amounts of sludge that form a secondary pollutant which is costly and difficult to dispose of (Farooq et al., 2010). Alternatively, Cr(VI) can be reduced to Cr(III) before the use of a precipitating agent (Hu, 2017). In the study by Hu, Cr(VI) was reduced to Cr(III) by Fe^{2+} using $Fe(NH_4)_2(SO_4).6H_2O$. The sludge formed was therefore $Fe(OH)_3/Cr(OH)_3$ which increased by 10% (Hu, 2017).

2.2.4 Adsorption

Adsorption occurs when atoms, molecules, ions, or electrons of an adsorbate adhere to the surface of an adsorbent. The adsorbent and the adsorbate may be a gas, a liquid or even a solid. The adsorption process is mostly applied in water treatment for the removal of contaminants such as trace metals. It has widely been studied by researchers for the removal of Cr(VI) from aqueous solutions. It is highly recommended due to its special characteristics which include high selectivity, ease of operation and flexibility, low cost effect, low energy employment, use of widely available adsorbents and regeneration of the adsorbents (He et al., 2019). The adsorption process can occur in two ways namely (i) chemisorption and/or (ii) physisorption.

(i) Chemisorption involves chemical bonding between the adsorbate and the adsorbent entailing the transfer or sharing of electrons. Chemisorption is usually irreversible since the chemical bonds formed are stronger and hard to break. High adsorption heats ranging from 40 to 400 kJ/mol, high activation energies and temperatures are required in chemisorption (Qiu et al., 2015). Chemisorption also depends on the number of binding sites and the surface area of the adsorbent which can be occupied by the metal ions of interest. Chemisorption mainly occurs over a homogenous surface resulting in a monolayered coverage.

(ii) Physisorption involves physical interaction between the adsorbate and the adsorbent mainly through Van der Waals forces. This type of adsorption is reversible and does not require high activation energies. Low energy inputs are required with energies ranging between 20 to 40 kJ/mol. It also occurs over low temperatures and decreases with an increase in temperature (Qiu et al., 2015). Physisorption occurs over a heterogenous surface and results in a multi-layered coverage.

2.3 THE USE OF ACTIVATED CARBON AS AN ADSORBENT

Activated carbons are carbon materials that have a large carbon content, high surface areas and porous structure. They have high heat resistance and widely used in purification of liquid and removal of toxic heavy metals from water streams. AC's are regarded as cost-effective adsorbents due to their abundant, readily available sources used to prepare them such as agricultural biowaste materials (Gottipati et al., 2012). These precursors usually contain high amounts of carbon and used for the preparation of AC which include; palm kernel shells (Anyika et al., 2017), termite feces (Demarchi et al., 2019), peanut shells (Cai et al., 2018), chestnut oak shells (Niazi et al., 2018), oil palm (Hesas et al. 2013), endocarp (Beltrame et al. 2018), bamboo bark (J. Li et al. 2018) and *Macadamia* nutshells (Pakade et al., 2016b). These biowaste precursors are mostly chosen due to their high carbon content and low ash content making them applicable for preparation of AC (Sunanya and Kumar 2018). The use of these precursors is not only useful for the purification of wastewater but also assists in environmental waste control by turning them into useful products (Sunanya and Kumar 2018).

The precursors have garnered different characteristics towards the adsorption of Cr(VI) depending on their preparations, surface morphology, surface areas and porosity. Activated carbon can be prepared in two simple activation methods which are (i) physical activation method and (ii) chemical activation method. In physical activation, the material is burnt in the absence of air to make it rich in carbon and pores (carbonization) whereas in chemical activation the material is exposed to activating agents such as acids and bases at low temperatures (Dula, Siraj, and Kitte 2014).

2.3.1 Physical activation

The physical activation process takes a two-way step which include carbonization through increased temperatures ranging from 300 to 900℃ followed by activation in the presence of inert gases with temperatures ranging from 700 to 1000℃ (Gottipati et al., 2012). The mostly used oxidizing gases include carbon dioxide, oxygen, steam or even air (Lesaoana et al., 2019). Most disadvantages related to physical activation include damage to the surface of the adsorbent due to high pyrolysis temperatures that damage the lignin of the precursors leading to loss of natural functional groups. Low quantity of adsorbent is obtained through each process due to burn out during pyrolysis.

In the study by Norouzi et al. (2018b) activated carbon was prepared from date press cakes through a two-way physical preparation method. Firstly, the date press cakes were carbonized at high temperatures (450-650℃) followed by chemical activation with solid NaOH pellets at different ratios. Figure 2.1 depicts the best activation energy and ratio of NaOH:AC obtained in the study for the adsorption of Cr(VI). It was stated that as the activation temperature increased, there was an increase in adsorption capacity of the AC on Cr(VI). This was supported by pore diffusion of NaOH molecules on the surface of AC as the temperature increased resulting in more porous surface. However, extensive increase in activation

temperature and ratio of NaOH:AC resulted in a decline in adsorption capacity of Cr(VI). This was attributed to the change in porosity of the AC due to high temperatures from a microporous to a mesoporous or even macroporous which results in change in surface area of the AC.

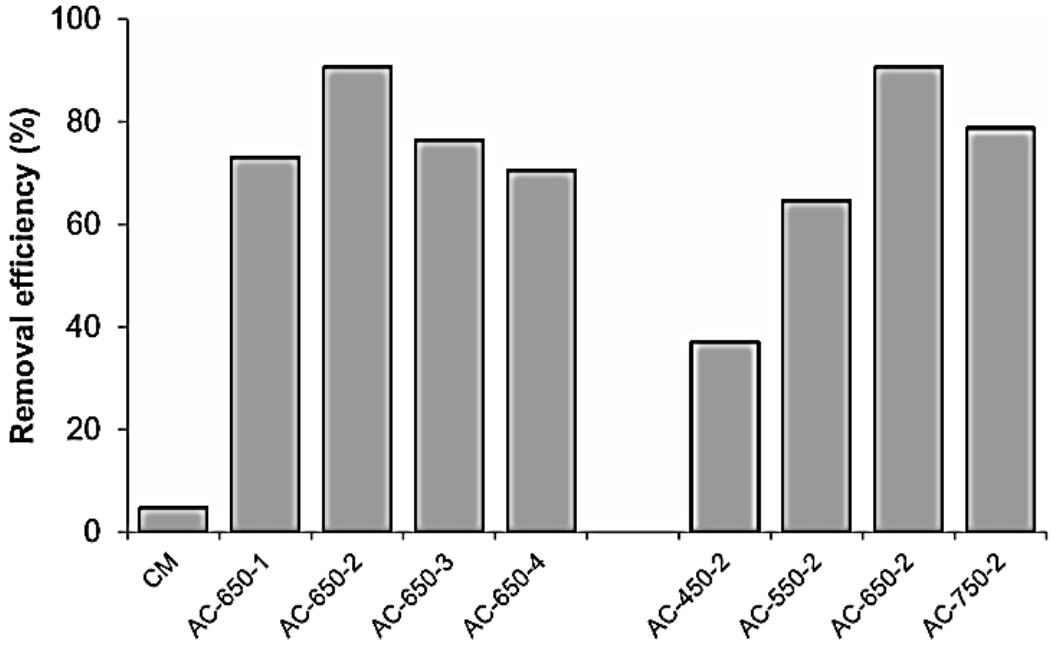

Figure 2.1: Effect of NaOH Effect of NaOH:AC and activation temperature on the removal efficiency of Cr(VI) (Norouzi et al., 2018b).

The best conditions of preparation of AC from date press cake were at 650 ℃ with a ratio of 2:1 NaOH:AC for chemical activation. The AC displayed high surface area of 2025.9 m^2/g and adsorption capacity of 282.8 mg/g for the removal of Cr(VI) from aqueous solutions.

Temperature is the one of the parameters with an effect on the behaviour of the AC on the adsorption process. The type of chemical activation agent used for the preparation of the AC also plays a role in the surface nature of the AC which affects the adsorption capacity intake of the AC on the adsorbate. Chemical activation may include acid activation, basic activation, and thermal activation.

Valentin-Reyes et al. (2019) explored all three activation methods using nitric acid for acidic activation, ammonium hydroxide for basic activation and nitrogen gas for thermal activation. An increase in acidic conditions resulted in a decrease in pore sizes and surface area. This was attributed to the collapse of AC walls due to strong acidic conditions. Increase in basic conditions however, resulted in increased porosity and surface area. An increase in temperature resulted in decrease in acidic functional groups with complete removal at higher temperatures.

Prajapati et al. (2020) prepared AC from aloe vera leaves through a two-way step of pyrolysis and chemical activation. In this study, sulfuric acid and nitric acid were employed as chemical activating agents at a ratio of 1:3 w/v of carbonized raw aloe vera leaves powder and each acid. It was observed that the surface area increased as modification occurred. Sulfuric acid treated AC (AL-SAT-AC) had the largest surface area of 359.74 m^2/g followed by nitric acid treated (AL-NAT-AC) with 277.3 m^2/g as compared to raw aloe leaves (RALP) with 10.57 m^2/g surface area. However, AL-NAT-AC had a slightly higher adsorption capacity of 59.83 mg/g as compared to AL-SAT-AC with 58.83 mg/g. The use of strong acids as chemical activating agents resulted in more, large deep surface pores which were able to be occupied by the Cr(VI) anions.

Thermodynamics were also explored in this study to understand the adsorption behavior of the prepared adsorbents on Cr(VI). It was observed that there was a decrease in removal efficiency with an increased temperature. It was explained that this observation was due to breakage of chemical bonding between the Cr(VI) anion and the acidic surface functional groups of the adsorbents. The adsorption process therefore followed an exothermic reaction for both the studied adsorbents. The reaction mechanism however, revealed that the oxygenated groups on the surface of the adsorbent resulted in reduction of Cr(VI) to Cr(III). The Cr(III) was adsorbed via complexation mechanism (Prajapati et al., 2020).

2.3.2 Chemical activation

In chemical oxidation, carbonization and activation occur simultaneously through one step. Chemical activation is well-known for its advantageous characteristics of lower activation temperatures with shorter activation times and high yields of AC (Açıkyıldız et al., 2014). Different activating agents such as H_2SO_4, H_3PO_4, KOH, HNO_3, HCl, $FeCl_3$, and $ZnCl_2$ have been studied (Solgi et al., 2017). However, the type of activating agent used determines the outcome of the characterized functional groups and surface morphology of the AC. Gottipatti & Mishra (2016) prepared a microporous activated carbon from *Aegle Marmelus* fruit shells through chemical activation using $ZnCl_2$. High surface area of 1339 m^2/g and pore volume of 0.48 cm^3/g together with an adsorption capacity of 43.54 mg/g were obtained.

Solgi et al. (2017) prepared AC from *Medlar* seeds through chemical activation with KOH at different temperatures. The surface area of the prepared AC was recorded as 198.6, 433.5, 1006, 1021 m^2/g for each adsorbent prepared at temperature 450, 550, 650 and 750℃ respectively. The surface area increased with an increase in temperature suggesting that the use of KOH as an activating agent requires high temperatures as recorded in literature. These results also displayed that high temperatures showed no harsh effect on the surface of the adsorbent leading to damages of the morphology of the adsorbent (Solgi et al., 2017). The maximum adsorption capacity obtained was 200 mg/g. The high adsorption capacity therefore represents a favorable adsorbent.

Niazi et al. (2018) investigated chestnut oak shells derived activated carbon for the removal of Cr(VI) from aqueous solutions. The activated carbon was prepared through chemical activation using 80% (v/v) H_3PO_4 solution. The chestnut shell powder's capability was also compared to that of the H_3PO_4-treated AC. It was observed that the surface area and pore volume increased as the activation occurred. Surface area and pore size of 40.90 m^2/g and 0.026 cm^3/g increased to 989.4 m^2/g and 0.71 cm^3/g for the chestnut shell powder and activated carbon, respectively. The increased surface area and porosity was attributed to the activation and carbonization process which resulted in larger porosity and surface area. The Cr(VI) adsorption capacities of 4.44 and 33 mg/g for chestnut shells powder and activated carbon were obtained. The increased adsorption capacity was attributed to increased acidic functional groups on the surface of the AC due to chemical activation with H_3PO_4 which increased electrostatic interactions and hydrogen bonding between the adsorbate and the adsorbent.

H_3PO_4 and H_2SO_4 were individually experimented as an activating agents for the conversion of Fox nutshells and wood apple shells precursors into activated carbon which was used for Cr(VI) adsorption (Doke and Khan, 2012; Kumar et al., 2017). The surface areas for the Fox nutshells and apple shells were found to be 2636 m^2/g and 1898 m^2/g with adsorption capacities of 74.95 mg/g and 151.51 mg/g, respectively. The results showed that although H_3PO_4-treated shells exhibited larger surface area, its adsorption capacity was lower compared to H_2SO_4-activated carbons. The lower surface area of wood apple shells was probably due to harsh treatment of AC by strong acid H_2SO_4 destroying the nature of the pristine AC. Such results suggest that not only does the surface area play a role in the adsorption capacity but other surface functionalities on the AC also determine the uptake of the Cr(VI) by the AC.

2.4 PORE SIZE CLASSIFICATION OF ACTIVATED CARBON

The nature of activated carbons employed in adsorption affects the adsorption capacity and the sorption process. The Brunuaer-Emmet-Teller can be used as one of the instruments that calculates the surface area and pore size of the AC. Depending on the size of the pores, an adsorbent can be regarded as microporous (< 2nm), mesoporous (2 – 50 nm) and macroporous (>50nm) (Zhang et al., 2016). The classification of pore distribution can therefore be used to determine the type of adsorption using the relative pressure P/P_o.

2.4.1 Types adsorption isotherms

Type I adsorption isotherms are usually achieved with microporous solids with relatively small external surfaces and pore sizes below 2 nm. They exhibit a convex upward shape as displayed in Figure 2.2 and can be best described using Langmuir isotherms. Such isotherms are characterized by a horizontal plateau which is parallel to the relative pressure P/P_o axis (Al-Ghouti and Da'ana, 2020). The plateau is the equilibrium point. Gottapi et al (2012) stated that narrow pores are not being able to accommodate any molecular layer. Examples of Type I adsorbents are activated carbons and zeolites (Zhang et al., 2016).

Type II isotherms represent monolayer-multilayered adsorptions involving nonporous or macroporous adsorbents (Gottapi et al., 2012). They take a concave shape at low P/P_o which is almost linear and then take a convex shape afterwards. The point marked with an arrow represents a stage where the monolayer coverage is complete and the inception of a multilayer adsorption (Zhang et al., 2016). Type III and Type V adsorption isotherms are mostly similar and are not common and form a convex shape throughout the entire P/P_o range.

These types occur where the adsorbate-adsorbate interaction is bigger than the adsorbent-adsorbate interaction which results in small adsorption at low relative pressure (Al-Ghouti and Da'ana, 2020).

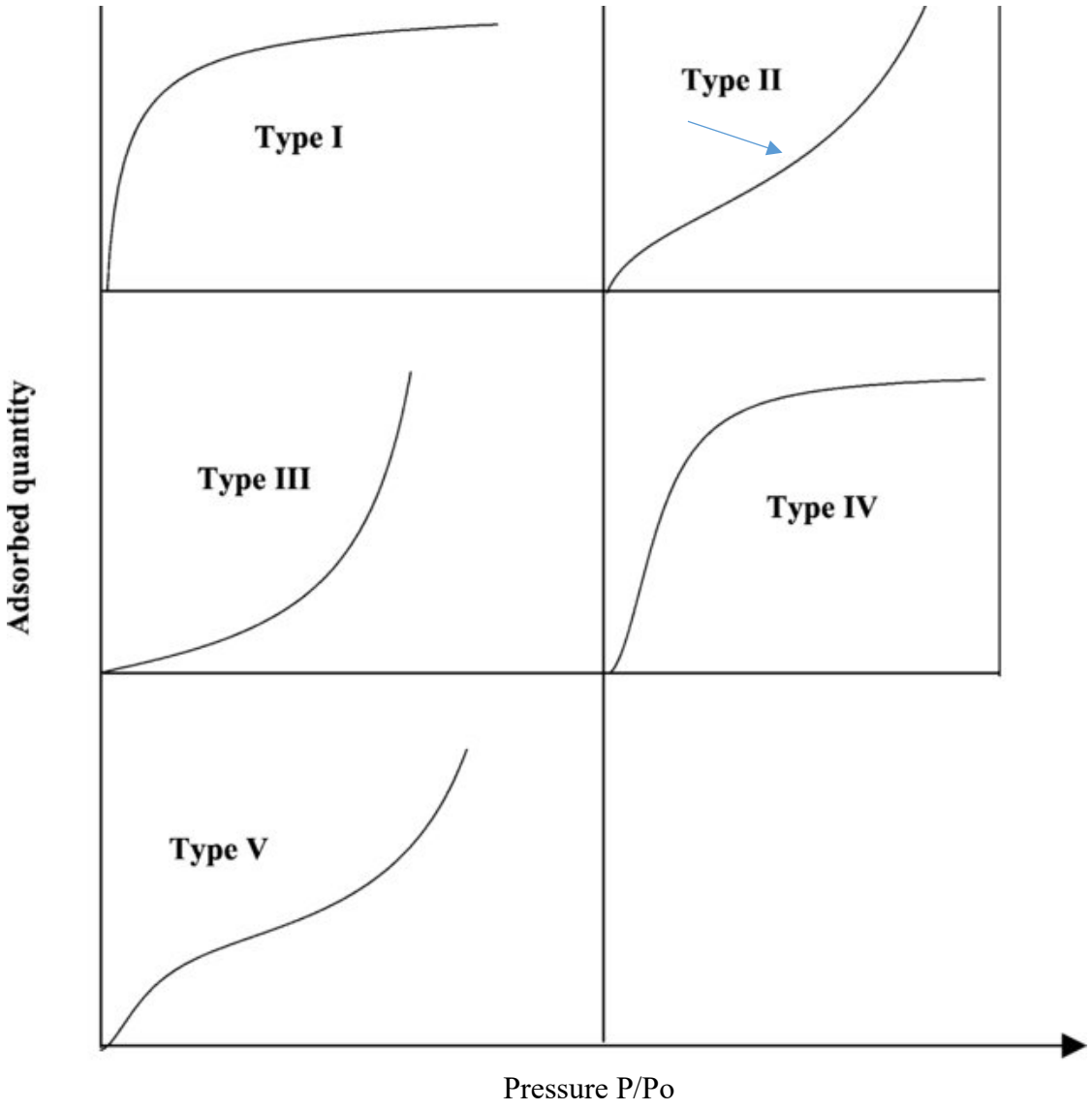

Figure 2.2: Five types of adsorption isotherms (Khalfaoui et al., 2003).

Type III are mostly common in nonporous adsorbents where else Type V are common in microporous and mesoporous adsorbents where the adsorbate-adsorbent interactions are weak. Type IV isotherms are formed due to capillary condensation in mesopores. They display a hysterical loop at higher relative pressures. It commonly represents adsorption-desorption

hysteresis and is more prevalent in oxide gels and mesoporous carbon materials (Gottapi et al., 2012).

2.4.2 Hydrophobicity of AC

Although AC's have recorded successful removal of Cr(VI) from aqueous solutions, they have been reported to be hydrophobic, making them less suitable for the removal of inorganic pollutants from water. To avert such challenges, AC have been modified using numerous methods. The inclusion of magnetic properties to the AC is one of the methods used to functionalize them for ensuring their suitability in inorganic contaminant removal (Zhao et al., 2016). The separation of the AC adsorbent from solutions therefore becomes a problem (particularly when powdered AC is used) and improper removal of spent AC from water may result in secondary pollutants. Scientists have therefore employed the use of magnetic separation due to induced magnetic properties on the surface of the activated carbon. Magnetic separation involves impartation of magnetic properties on the surface of the AC through the embedment of Fe_3O_4 nanoparticles on AC surface. The resultant material acquires magnetic properties making its separation from water easy through the application of an external magnet (Wang et al., 2020a). Magnetic separation therefore assists in improving the regeneration of the AC after adsorption preventing secondary pollution by the AC (Wang et al., 2020b). Magnetic activated carbons can be prepared in different procedures including: pyrolysis, co-precipitation, hydrothermal methods, solvothermal method etc. (Feng and Li, 2017). These methods have been marked to effective at producing magnetic activated carbons however, the debate as to preparing magnetite with uniform magnetic properties, high surface area, high adsorption capacities and selectivity towards Cr(VI) has evolved (Wang et al., 2020a).

2.4.2.1 Preparation of magnetic activated carbon through pyrolysis

Synthesis of magnetic activated carbon through pyrolysis include thermal decomposition of both the AC and iron salts at different temperatures in the absence of oxygen. Magnetic nanoparticles are induced on the surface of the AC either through a chemical or physical treatment, then pyrolysis at different temperatures in absence of oxygen (Anyika et al., 2017). Pyrolysis aims to develop micropores on the surface of the magnetic activated carbon by heating at high temperatures which results in loss of water components from dehydration (Li et al., 2017). The larger pores result in increased removal of adsorbate which are trapped in the pores during adsorption process. Although, elevated temperatures in pyrolysis result in large pore sizes, they have also been reported to damage the porosity of the AC which results in decreased surface areas (Li et al., 2017). Increased temperatures not only destroy the porous structures of the adsorbents but also affects the natural functional groups on the surface of the adsorbent by damaging the lignocellulose of the AC.

Wang et al. (2020) employed *Enteromorpha prolifera* for the preparation of magnetic biochar for the adsorption of Cr(VI). The *Enteromorpha prolifera* powder was pyrolyzed at different temperatures ranging from 400 to 800℃. However, 400 and 800℃ was picked as the suitable temperatures based on their surface areas. Electron paramagnetic resonance (EPS) was used to study the presence of environmental persistent free radicals (EPFR) on the surface of the prepared adsorbents and the spectra are displayed in Figure 2.3. No signals were observed for EPFR for BCF800 however, at lower temperatures, stronger signals for EPFR were observed. At higher temperatures, the EPFR are easily consumed by transition metals (in this instance Fe(III)). It was also reported that as temperature was increased, the surface area also increased. BCF800 had the highest surface area of 780.14 m^2/g and therefore was explored as an adsorbent for the adsorption of Cr(VI). The maximum adsorption capacity of 95.23 mg/g was obtained

which was fairly higher than the compared adsorption capacities of previously reported studies (Han et al., 2016) with adsorption capacity of 77.54 mg/g using magnetic peanut hull biochar as an adsorbent. A relatively low adsorption capacity of 13.83 mg/g using magnetic pine sawdust biochar was observed (Reguyal et al.,2017) as compared to the reported study.

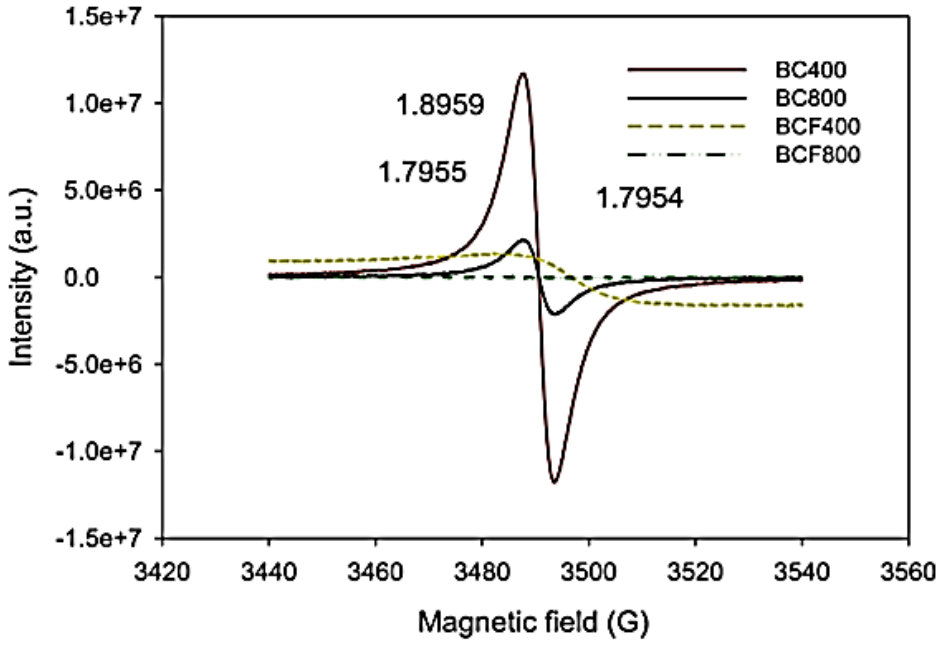

Figure 2.3: Electron paramagnetic resonance (EPS) spectra of magnetic biochar and pristine biochar (Wang et al., 2020).

Yitong et al. (2016) prepared magnetic activated carbons from peanut hulls by a pyrolysis method using ferric chloride solution as a source of magnetization. The temperature was varied from 400, 450, 500, 550, 600 and 650℃ as to determine the optimum conditions for the preparation of AC with better sorption properties. The saturated magnetization increased with increased temperatures as follows 0.20, 4.28, 36.79 emu/g for BC400mag, BC450mag and BC650mag. These results revealed that temperatures below 400℃ were not able to form strong magnetization and therefore, temperatures above 450℃ were recommended. Large surface area values of 209.5 m^2/g for BC650mag and 180 m^2/g for BC450mag were reported. The large

surface and saturated magnetization of the adsorbent prepared at 650℃ resulted in it being the employed adsorbent for the removal of Cr(VI) (Han et al., 2016).

2.4.2.2 Preparation of magnetic activated carbon through co-precipitation

In chemical co-precipitation, two or more compositions of cations are obtained in a homogenous solution (Jiang et al., 2018b). The resulting product usually contains a large number of small particles that are highly insoluble. The co-precipitation method is simple, rapid and does not require complicated experimental setup. The iron oxide can be produced through co-precipitation of Fe^{3+} and Fe^{2+} under inert gas flow through a simple reflux procedure. High adsorption capacities have been reported for the adsorbents prepared through this method (Fatehi et al., 2017). However, the magnetic activated carbon prepared from co-precipitation has a tendency of forming agglomeration, which affects the surface area and morphology of the AC. Trends of reduced surface area as the Fe_3O_4 nanoparticles are being attached to the AC have also been observed (Qiu et al., 2016, Fatehi et al., 2017). Furthermore, Fe_3O_4 oxidizes in the air resulting in decreased magnetic character and even total loss of magnetism (Ta et al., 2016). Modification and functionalization of magnetite nanoparticles through the use of supporting materials such as SiO_2, alumina oxides, and chitosan have been explored (Jiang et al., 2018b).

Xitong et al. (2014) prepared magnetic cellulose nanocomposites through co-precipitation of Fe^{3+} and Fe^{2+} followed by functionalization of the composites with amino groups. The prepared adsorbents were found to be super magnetic with saturating magnetization values of 12.3 and 10.1 emu/g for MSC (Fe_3O_4@SiO_2@cellulose) and MSCGE (amino functionalized Fe_3O_4@SiO_2@cellulose), respectively. The decrease in magnetic property was ascribed to the coverage of the surface by the amino group chains. The surface area was 69.5 m^2/g and 46.4 m^2/g for MSC and MSCGE, respectively. The decrease in surface was due to the

attachment of chained glycidyl methacrylate and ethylenediamine to the MSC causing blockage of pores. Although the surface area declined, the adsorption capacity of Cr(VI) was high valued at 171.5 mg/g.

2.4.2.3 Preparation of magnetic activated carbon through hydrothermal synthesis

Hydrothermal synthesis is defined as a chemical reaction in aqueous solutions occurring above the boiling point of water (Feng and Li 2017). Thus, it involves a chemical reaction of a mineral containing a crystallizing substance such as Fe above boiling point of water under high pressures. A steel pressure vessel such as an autoclave is used in this process. The demand for the use of an external equipment (autoclave) which is costly serves as a disadvantage amongst many other reasons including safety issues and inability to monitor the reaction (Rane et al., 2018). Cai et al. (2018) revealed that although the hydrothermal process results in high adsorption capacity and removal efficiencies, other factors affecting the surface of the prepared adsorbents render the use of this method to be unfavorable. In the study by Cai et al. (2018), three adsorbents (magnetic peanut shell activated carbon (MPAC), peanut activated carbon (PAC) and commercial activated carbon (CAC) were prepared and their adsorption capacities were compared. High adsorption capacity of 98.88 mg/g was reported for MPAC as compared to 87.7 mg/g of PAC and 87.69 mg/g of commercially activated carbon. High magnetic separations were also observed visually using a magnet showing black precipitate from the solution being attached to the magnet placed outside the reacting vessel container. However, the saturation magnetization value of 8.06 emu/g was recorded and described as low compared to values reported in literature. The decrease in saturation magnetization in this study was explained through the composite of tightly anchored Fe_3O_4 particles on the non-magnetic PAC (Cai et al., 2018).

Elsewhere, commercial carya peels based activated carbon was used to prepare cobalt/iron oxide nanocomposites ($Co/Fe_3O_4/AC$) for the removal of Cr(VI) (Qiu et al., 2016). In this study, a hydrothermal method was employed using a thermal kettle for the preparation of the composites. The composite was prepared using a ratio 1:2:150 for Co^{2+}: Fe^{3+}:AC and a slight decrease in surface area of AC from 1243.35 m^2/g to 1064.05 m^2/g for the nanocomposite was observed. Although there was a decrease in surface area, the pore diameter did not show any significant difference (0.08 cm^3/g) which implied that the pores were not blocked to a large extent by the nanocomposites. The saturated magnetization of the $Co/Fe_2O_4/AC$ was 6.93 emu/g showing acceptable magnetic properties which were able to cater for applied magnetic fields and separations. The adsorption capacities of the pristine AC and the $Co/Fe_2O_4/AC$ were compared and found to be 76.923 and 83.33 mg/g, respectively. This implied that the functionalization of magnetic nanoparticles on the surface of the AC resulted in increased adsorption capacities.

2.4.2.4 Preparation of magnetic activated carbon through solvothermal synthesis

Solvothermal method is similar to the hydrothermal method since an external device such as an autoclave is used. In solvothermal synthesis, organic solvents such as oleic acid, hexamethylenetetramine, ethanol amine, or polyethylene glycol are used as surfactants instead of water (Shi et al., 2018). The magnetic nanoparticles are prepared in a sealed vessel (autoclave) by boiling the solvents above their boiling point.

Solvothermal method therefore allows for controlled size, shape distribution, and crystallinity of the nanoparticles by simply changing the experimental parameters such as, temperature, pressure, reaction time and solvent type (Ren et al., 2019). In the study by Shunquan et al. (2018) $Fe_3O_4@SiO_2\text{-}NH_2$ nanoparticles were prepared using solvothermal method with polyethylene glycol, sodium acetate, and PEG_{400}. The prepared nanoparticles

were then loaded on the surface of the AC through sonication. The obtained adsorption capacity of Cr(VI) was 27.2 mg/g and the saturated magnetization was 23 emu/g. The high magnetic property showed that the method was suitable as further functionalization of the nanoparticles to the AC did not cause damage to the magnetic particles.

Similarly, Ren et al. (2018) prepared Fe_3O_4@Carbon composites using a one-step solvothermal method with $Fe(NO_3)_3$, cyclodextrin and urea in an autoclave. Fairly high surface area of 112.91 m^2/g and adsorption capacity of 33.35 mg/g for Cr(VI) and 262.72 mg/g for Congo red were achieved. The adsorption isotherm depicted for this adsorbent was a Type IV inferring to a mesoporous structured adsorbent with weak adsorbent-adsorbate interaction. Although solvothermal is cost-effective due to a one-step reaction, the adsorption capacities recorded for Cr(VI) are a bit lower compared to those in literature (Ren et al., 2018).

2.4.3 The use of supporting reagents

Magnetic materials are known to be unstable under ambient conditions due to their high oxidation state making them prone to oxidize in air and in various acidic solutions (Ta et al., 2016). Their high surface energy often leads to aggregation which in turn minimizes the surface area due agglomeration. Non-magnetic supporting materials are therefore used to provide individual particle stability and durability. Inorganic silica (SiO_2) is one such supporting material that can be used due to its favorable characteristics of being stable under acidic conditions, inertness to redox reaction and high content of hydroxyl groups on its surface that allows for further functionalization, ease binding and attachment of ligands (Ta el al., 2016).

Fatehi et al. (2017) incorporated magnetite nanoparticles onto almond shell activated carbon through co-precipitation of Fe(II) and Fe(III) supported with SiO_2 for further functionalization of amino groups to the magnetite for the removal of Pb(II) and Cr(VI) from saline solutions. The main functional groups responsible for the uptake of Pb(II) and Cr(VI) from aqueous solution were the –COOH and $–NH_2$. However, there was a decrease in surface area related to the iron and silica penetration into the pores of the adsorbent causing blockage of pores. Although there was a decrease in surface area, the composite activated carbon showed a significantly higher amount of acidic functional groups (1.73 mequiv/g) indicating the presence of oxygen groups which were ideal for the removal and adsorption of heavy metals from water systems. Therefore, although physical blockage of pores is experienced, adsorption can still occur through chemical interaction through the functionalization of –COOH and $–NH_2$ on the surface of the adsorbent resulting in better removal efficiencies (Fatehi et al., 2017).

Dutta and Nath (2018) prepared SiO_2/Carbon nanocomposites and nanoporous carbon from corncob bio waste material and used as an adsorbent for methylene blue dye, uranium (VI) and chromium (VI) in wastewater systems. For all three toxicants, SiO_2/CCNC showed higher adsorption capacity compared to the CCNC. This was attributed to high surface area and pore volume on the SiO_2/CCNC compared to the CCNC. The BET displaced 715.22 m^2/g and 430.17 m^2/g for SiO_2/CCNC and CCNC, respectively. The leaching out of SiO_2 by addition of NaOH to form the CCNC disrupts the microstructure of the composites which reduces the porosity of the sample and its surface area. Nanoporous silica has a high surface area and porous structure making it stable at higher thermal and hydrothermal conditions, hence better sorption capacities.

2.4.4 Functionalization with amino groups

The use of organic polymers such as m-phenylenediamine, CM-dextran and chitosan to create a polymer core shell around the magnetite for protection has been explored (Shunquan et al., 2018). The use of organic polymer core shells did not only protect the Fe_3O_4 particles but also immobilized the Cr(III) formed through reduction of toxic Cr(VI) as the amino groups acted as Lewis bases and formed complexes with the Cr(III) (Shunquan et al., 2018). The amine(-NH) containing polymers have been extensively used for the removal of toxicants due to their porous structure, chemical reduction ability, environmental stability and their high content of amine groups (Jiang et al., 2018).

Amine functional groups can easily be protonated, thus allowing electrostatic interactions between their positively charged binding sites and anionic metal ions such as Cr(VI). Removal of metal ions can easily occur through hydrogen bonding contained amine groups giving rise to removal efficiencies (Luo et al., 2017). Different conducting polymer composites such as polyethyleneimine (PEI), polypyrrole (PPy), and polyaniline (PANI) are being used for better sorption capacities due to their abundant amino group content (Jiang et al., 2018b). In the study by Uyioso et al. (2018), magnetic nanocomposites were coated with polypyrrole and used as an adsorbent for the removal of Cr(VI). Adsorption capacities as high as 208.77 mg/g were obtained with saturation magnetization of 23 emu/g. The high magnetic property supported that polypyrrole was successful in supporting the shell from leaching out and oxidizing.

Luo et al (2017) functionalized PEI on corn bract activated carbon for the removal of chromium (VI) from aqueous solution. PEI contains large amounts of primary and secondary amine groups which provide hydrogen binding sites and electrostatic interaction with the negatively charged species. The adsorption kinetics of this study followed a pseudo second order rate

model with an optimum adsorption capacity of 438 mg/g. The adsorption modelling on the other hand was best fit for Langmuir isotherm indicating a monolayered adsorbent on a homogenous surface. The chemical composition of the adsorbent (PEI-CB) before and after adsorption was studied using high resolution XPS. The characteristic peaks at 398.6 and 397.9 eV displayed before adsorption were assigned to $–NH_2$ and =N of the PEI in the adsorbent. However, a new peak was observed after adsorption to 400.1 eV assigned to protonated $–NH_3^+$ supporting that Cr(VI) was bonded through protonation onto the amine groups of the PEI.

In the study by Liu et al (2019) polyamidoamine dendrites (GP/PAMAM's) were functionalized on graphene oxide for the removal of Cr(VI). The adsorption mechanisms drawn from the study showed three steps (i) the Cr(VI) was adsorbed by binding to the protonated amine groups of the GP/PAMAM's (ii) the reduction of Cr(VI) to Cr(III) through the π-π electrons on the carbocyclic six-membered ring of the GO and (iii) the release of Cr(III) into solution due to repulsion forces between the Cr(III) and the protonated amine groups. The adsorption capacity was recorded to be 211.4 mg/g fairly high compared to other studies. Other studies such as Zhang et al (2018) have reported similar adsorption mechanisms where the main mechanism was due to electrostatic interaction between the Cr(VI) and the adsorbent (Fe_3O_4-PEI-SERS) and the second one being the reduction of Cr(VI) to Cr(III) due to protonation of the amine groups (-NH-/-NH_2).

Polyethyleneimine functionalized on corn bract have also been explored by Luo et al (2017) for the adsorption of Cr(VI) from aqueous solutions. The adsorption mechanism from this study showed that the Cr(VI) was firstly adsorbed through the protonation of the amine groups from the PEI, followed by the reduction process through electron donors from the biomass which finally resulted in the reduction of Cr(VI) in solution to Cr(III). The XPS results displayed in

Figure 2.4 were used to further explain the adsorption mechanism. The two peaks at 3.97.9 and 398.6 eV before adsorption (B) were attributed to =N- and $–NH_2$ of the PEI which decreased in intensity after adsorption displaying a new peak at 400.1 eV representing the protonated $–NH_3^+$. This proved that the Cr was bound to the protonated amine groups. The adsorption was declared to have occurred through electrostatic interactions and hydrogen bonding between the amine groups with the oxygen of the $HCrO_4^-$. Adsorption capacities as high as 438 mg/g were discovered (Luo et al., 2017).

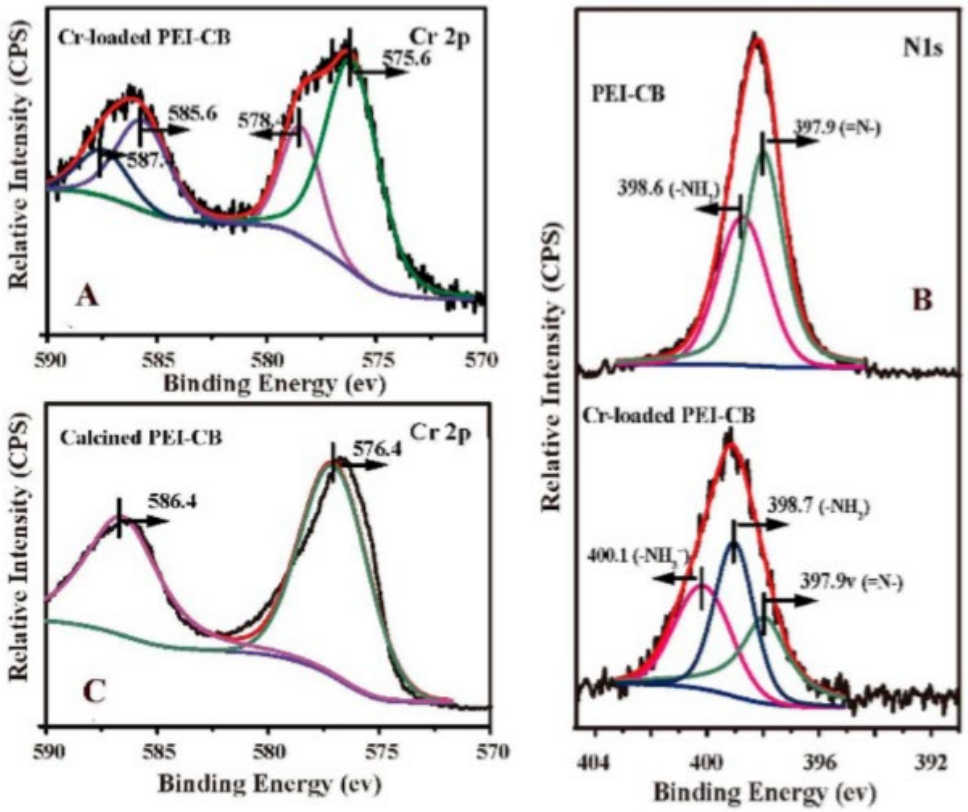

Figure 2.4: XPS spectra before and after adsorption (Luo et al., 2017).

Similarly, protonation of amine group of PANI -NH was changed to amine group –N= after the adsorption of Cr(VI). The reaction mechanism for this reported study is displayed in Figure 4. In this study polyaniline (PANI) functionalized adsorbent was explored for the removal of Cr(VI) form aqueous solutions. It is observed that the reaction mechanism took a three-way

path number one being, electrostatic interaction or ion exchange between oxyanion Cr(VI) ions and protonated amine groups on the surface of the adsorbent. The second step involved the reduction of the remaining Cr(VI) ions to Cr(III) while other amine groups are also oxidized to quinoid amines. The third reaction mechanism involves partial binding of the Cr(III) to oxidized quinoid amines of the PANI.

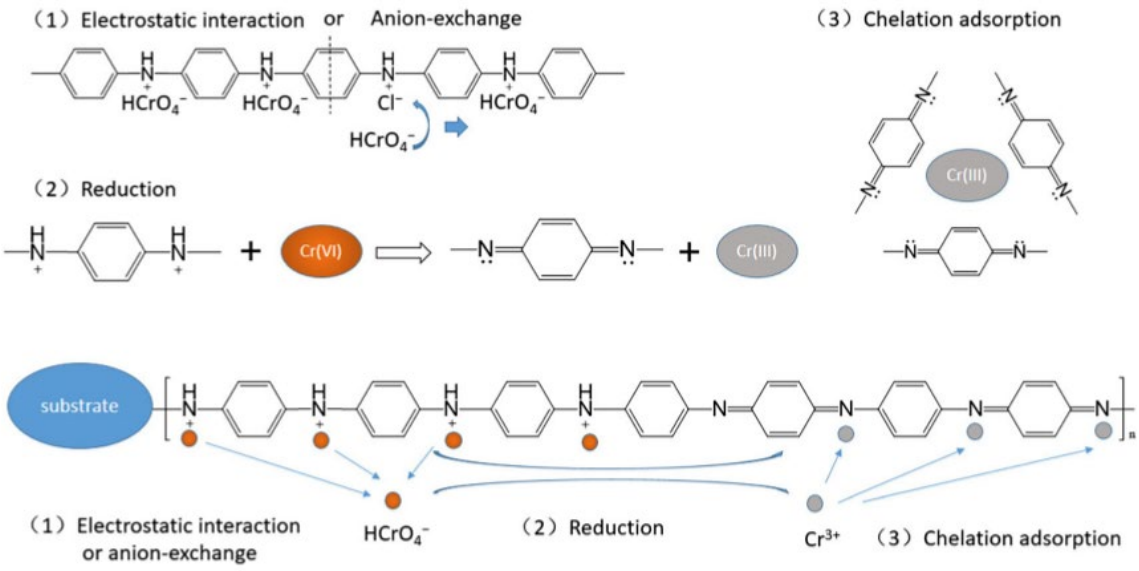

Figure 2.5: Reaction mechanism of Cr(VI) removal by polyaniline (PANI) (Jiang et al., 2018).

Polyethyleneimine (PEI) functionalized have been repeatedly reported with a downfall of the adsorbents facing decreased surface areas and pore diameters due to blockage of pores by gelatinous structure of the PEI. Similarly Junhua et al., (2020) showed decreased surface area of 345.2 m^2/g for iron functionalized multiwalled carbon nanotubes (MWCNT/γFe_2O_3) to 285.7 m^2/g for PEI-iron functionalized multiwalled carbon nanotubes (MWNT-PEI/γFe_2O_3) due to blockage of pores by PEI. However, the adsorption capacity was increased as functionalization occurred. MWCNT/γFe_2O_3 had an adsorption capacity of 208.1 mg/g where else MWCNT-PEI/γFe_2O_3 resulted in 285.7 mg/g adsorption capacity. The high adsorption

capacity related with PEI functionalized adsorbent was attributed to chelation and complexation between the amino groups of the PEI with the Cr(VI) species.

Protonation of amino group during the adsorption process occurs in different manners depending on the functional groups and ion charges present on the surface of the adsorbent. Cai et al (2019) functionalized hexamethylenediamine (HDA) on magnetic peanut halls biochar through hydrothermal method. The reaction mechanism between the MPHC-HDA and Cr(VI) is displayed:

$X\text{-}2NH_2 + 2H^+ + Cr_2O_7^{2-} \rightarrow X\text{-}NH_3^+ - Cr_2O_7^{2-}$

$X\text{-}2NH_2 + H^+ + HCrO_4^- \rightarrow X\text{-}NH_3^+ - HCrO_4^-$

$X\text{-}2COOH + 2H^+ + Cr_2O_7^{2-} \rightarrow X\text{-}2COOH^+ - Cr_2O_7^{2-}$

$X\text{-}OH + H^+ + HCrO_4^- \rightarrow X\text{-}OH_2^+ - HCrO_4^-$

The amino groups ($–NH_2$) of the HDA were protonated to form NH_3^+ to allow for the electrostatic uptake of negatively charged Cr(VI) ions. Then oxygenated functional groups present on the surface of the MPHC-HDA curtesy to biochar including COOH and OH- are also protonated to form $–OH_2^+$ and $–COOH_2^+$ under acidic conditions. The increase in possibilities of electrostatic interactions therefore resulted in high adsorption capacity of 142.86 mg/g. The kinetics isotherms supported that the adsorption reaction occurred through chemisorption either by electrostatic interaction or hydrogen bonding which followed pseudo-second order rate law.

Yang el al. (2018) explored polypyrrole for decoration of magnetic corncob biochar and explored it for the adsorption of Cr(VI). The reaction mechanism in this study followed a three-way step where firstly the Cr(VI) anions were adsorbed on the surface of the adsorbent through ion exchange and electrostatic interaction. The second step included the reduction of Cr(VI) to

Cr(III) by the amine group (-NH-) and the hydroxyl groups (C-OH-) on the surface of the adsorbent (MBC-PPy). The third step included the immobilization of the Cr(III) cation by precipitation and chelation while some parts were released to the solution due to repulsion forces. Adsorption capacities obtained from this study was 19.23 mg/g. Although not all the Cr(VI) anions were not totally removed, the MBC-PPy catered for reduction of Cr(VI) to less toxic Cr(III) and the immobilization of the generated Cr(III) (Yang et al., 2018).

Amino groups can be classified as primary (1°), secondary (2°) or tertiary (3°) depending on the hydrogen atoms being replaced by the carbon atoms. Primary amine groups are known to have higher removal capacities compare to the secondary and tertiary due to their short chain lengths and low basicity (Lee et al., 2020). However, Lee at al. (2020) displayed higher adsorption capacity of 260.74 mg/g for pssN-GO adsorbent as compared to 208.22 and 189.47 mg/g of psN-GO and pN-GO, respectively. The psN was related to primary amine group binding to silane supported graphene oxide which contained one amine, where else psN-GO was secondary amine and pssN-GO was secondary amine containing three amino groups. The high adsorption capacity experienced by secondary amine group (pssN-GO) depicted that in this study, the number of the amine present in the adsorbent played a higher role as compared to the efficiency of the amine group itself (Lee et al., 2020).

CHAPTER 3:

3.0 INTRODUCTION

Based on the literature reviewed in Chapter 2, this chapter gives a full description of the problem statement, aim and objectives of the study.

3.1 PROBLEM STATEMENT

Chromium (VI) is considered as one of the most toxic trace metals causing contamination and subsequently health related problems like skin irritation, lung cancer, kidney, lung, and gastric damage. Chromium (VI) is introduced in the environment through careless disposal and improper treatment of effluents from industrial activities such as leather tanning, electroplating, mining and so forth. The methods in place for the removal of Cr(VI) are considered to be ineffective because they are costly, require high energy inputs and generate sludge which is expensive to dispose of. The use of activated carbon as an adsorbent in industrial processes has increased based on its large porous structure, large surface area, and high removal efficiency. However, activated carbon has poor selectivity and sorption for inorganic compounds due to its hydrophobicity. To make activated carbon more compatible (hydrophilic) for inorganic ions, functionalization through the impartation of oxygenated functional groups on its surface is usually carried out. In addition, to improve the separation of activated carbon adsorbents from aqueous solution after adsorption, the AC surface is modified by inducing the magnetic properties onto the adsorbent.

3.2 AIM

Exploring the adsorption of Cr(VI) using the prepared iron oxide functionalized PEI activated carbon-silica composites.

3.2.1 Specific objectives

1. To modify commercial activated carbon (AC) with potassium hydroxide solutions.
2. To prepare the magnetic activated carbon (AC-Fe_3O_4) using co-precipitation method.
3. To prepare the magnetized silica-coated activated carbon (AC-Fe_3O_4-SiO_2) through reflux set up using tetraethylorthosilicate (TEOS).
4. To prepare the magnetized amino functionalized activated carbon silica composites (AC-Fe_3O_4-SiO_2-PEI).
5. To characterize AC-Fe_3O_4, AC-Fe_3O_4-SiO_2 and AC-Fe_3O_4-SiO_2-PEI with elemental analysis (EA), thermogravimetric analysis (TGA), scanning electron microscopy (SEM), Fourier transform infrared (FTIR) spectroscopy, Brunauer-Emmett-Teller (BET), X-Ray diffraction (XRD), transmittance electron microscopy (TEM), X-ray photoelectron spectroscopy (XPS) and zeta potential.
6. To investigate the effects of parameters such as the pH, time, concentration, temperature, amount of adsorbent and reusability on adsorption of Cr(VI).
7. To study the equilibrium, kinetics and thermodynamics adsorption process aspects using adsorption isotherms and models.
8. To compare the adsorption capacities of the current study to those in literature

3.3 HYPOTHESIS

- Iron oxide-PEI functionalized activated carbon-silica composites can be used to remove Cr(VI) and total chromium from aqueous solutions.
- Magnetic separation through functionalizing Fe_3O_4 nanoparticles on the AC can be used for separation of the adsorbent from the aqueous solution.
- Iron-PEI functionalized activated carbon-silica can be employed for the removal of Cr(VI) and Cr(III) through electrostatic interaction, proton donors and physical interactions.

CHAPTER 4:
RESEARCH METHODOLOGY

4.0 INTRODUCTION

The chapter outlines the chemical reagents used in the synthesis and preparation of standard solutions, adsorbent material preparation and modification procedures as well as instrumentation methods adopted.

4.1 REAGENTS AND MATERIALS

Table 4.1 lists the chemicals used in the study, their purity, and suppliers they were sourced from. All chemicals were of reagent grade and were utilized without further treatment or purification. Commercial *Macadamia* activated carbon was supplied by Innovation Carbon Pty LTD (Johannesburg, South Africa).

Table 4.1*:* The list of chemicals used and their grades.

Chemicals	**Purity**	**Supplier**
Potassium hydroxide (KOH)	98%	Glassworld
Sodium hydroxide (NaOH)	98%	Glassworld
Iron (III) chloride ($FeCl_3.6H_2O$)	99%	Glassworld
Iron (II) chloride ($FeCl_2.4H_2O$)	98%	Glassworld
Potassium dichromate ($K_2Cr_2O_7$)	99.0%	Merck
1,5'-Diphenylcarbazide (DPC)	+ 97%	Alfa Aesar
Methanol	98%	Glass world
Hydrogen peroxide	35%	Labochem

Ethanol	99%	Labochem
Acetic acid	99%	Glassworld
Hydrochloric acid	33%	Glass world
Sulphuric acid	98%	Labochem
Tetraethylorthosilicate (TEOS)	98%	Sigma Aldrich
N,N'- Dimethylformamide (DMF)	99.8%	Sigma Aldrich
3-glycidyloxypropyltrimethoxysilane (GPS)	98%	Sigma Aldrich
Polyethyleneimine (PEI) branched	Mw 25000	Sigma Aldrich

4.1.2 Preparation of stock solutions and working solutions

All stock solutions and working standards were prepared using ultrapure water from Labostar equipment (Warrendale, Pennysylvia, USA). A 1000 ppm chromium stock solution was prepared by dissolving 2.8289 g of $K_2Cr_2O_7$ in ultrapure water. This stock solution was used to prepare working solutions and standards by known dilution amounts.

4.2 PREPARATION OF ADSORBENTS

4.2.1 Pre-treatment of *Macadamia* nutshell activated carbon (AC-KOH)

Virgin activated carbon produced from steam physical activation were immersed into a solution of potassium hydroxide for secondary treatment. Chiefly, a known amount of *Macadamia* nutshell activated carbon (MNAC) was crushed and sieved between 300 and 150 µm screens for grain size control. That is, about 10 g of the sieved MNAC was dispersed in 100 mL solution of 5 M potassium hydroxide and stirred for 3 h on a magnetic orbital shaker at ambient temperature. The product was then filtered and washed several times with ultrapure water. The sample was further neutralized with 1% acetic acid. Finally, the recovered sample was then dried in an oven at 60℃ for 24 h and labelled AC-KOH.

4.2.2 Preparation of iron oxide functionalized activated carbon (AC-Fe_3O_4)

A method reported by Fatehi et al. (2018) was used to prepare both magnetized and silica coated activated carbon. Magnetized activated was prepared through co-precipitation of Fe(III) and Fe(II). Briefly 10.812 g of $FeCl_3.6H_2O$ and 3.987 g of $FeCl_2.4H_2O$ were dissolved in 300 mL ultrapure water and refluxed at 70℃ under inert nitrogen flow for 2 h. About 5 g of AC-KOH was added to the Fe^{2+}/Fe^{3+} solution to obtain a 1:1 ratio and stirred for 30 min. The pH was maintained between pH 10 and 11 using 5 M NaOH for formation of black precipitated AC-Fe_3O_4. The precipitated AC-Fe_3O_4 was separated with a magnet after 24 h, washed several times with deionized water and ethanol and dried at 60℃ overnight. The adsorbent was labelled AC-Fe_3O_4. The formation of the magnetite nanoparticles is summarized in the expression:

$$2FeCl_3 \cdot 6H_2O + FeCl_2 \cdot 4H_2O + 8NaOH \rightarrow Fe_3O_4 + 8NaCl + 14H_2O$$

4.2.3 Preparation of iron oxide functionalized-silica coated activated carbon (AC-Fe_3O_4-SiO_2)

About 5 g of the recovered AC-Fe_3O_4 was refluxed in a 500 mL water and ethanol solution of 4:1 ratio at 60℃ under nitrogen flow. Tetraethylorthosilicate (TEOS) was added dropwise to the solution to form a brownish colored AC-Fe_3O_4-SiO_2. The pH was again adjusted to basic conditions (pH 9 to 11) using 5 M NaOH solution. The adsorbent was separated magnetically from the solution after 6 h, washed several times with distilled water and ethanol and dried at 60℃ overnight. The product was labelled AC-Fe_3O_4-SiO_2.

4.2.4 Preparation of epoxy coated activated carbon (AC-Fe_3O_4-SiO_2-GPS)

In order to bind the 3-glycidocypropyltrimethoxysilane (GPS) on AC-Fe_3O_4-SiO_2, the material was first hydroxylated using a method reported by Thi et al (2016) to increase the hydroxyl groups on the surface of silica particles. A 500 mL piranha solution (3:1 sulfuric acid and hydrogen peroxide) was prepared and allowed to cool for 24 h. About 5 g of AC-Fe_3O_4-SiO_2

was then added to the solution and sonicated for 10 min under nitrogen flow. The sample was then separated through centrifuge and washed several times with ultrapure water and ethanol. The adsorbent was dried at 60℃ for 12 h. This sample was labelled hydroxylated AC-Fe_3O_4-SiO_2. Hydroxylated AC-Fe_3O_4-SiO_2 was then reacted with 10 mL of GPS and 20 mL toluene at 70℃ for 8 h under nitrogen flow. The adsorbent was then washed and separated from the solution by a centrifuge, washed several times with distilled water and ethanol and dried at 60℃ overnight. This adsorbent was labelled AC-Fe_3O_4-SiO_2-GPS.

4.2.5 Preparation of amino modified adsorbent (AC-Fe_3O_4-SiO_2-PEI)

About 5 g of AC-Fe_3O_4-SiO_2-GPS was refluxed in 5% solution of branched polyethyleneimine (100 mL) at 70℃ for 12 h. The material was then filtered and washed several times with deionized water and ethanol. The adsorbent was then dried at 60℃ in an oven overnight.

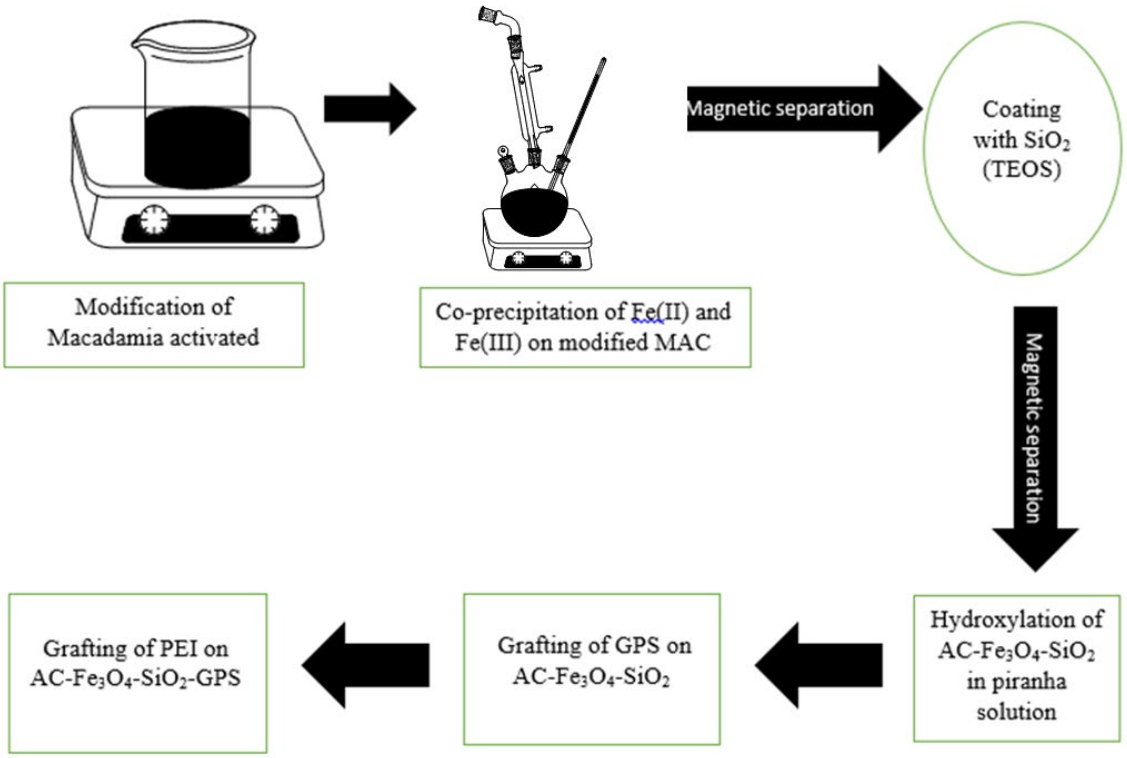

Figure 4.1: Schematic diagram of preparation of adsorbents.

4.3 CHARACTERIZATION OF ADSORBENT

4.3.1 Elemental analysis

The elemental analysis of all the adsorbents were conducted on an Elementar vario EL cube ThermoFlash 2000 series CHNS/O Organic Elemental Analyser. The percentage of carbon, hydrogen, nitrogen, sulfur, and oxygen were determined using combustion analysis by heating the adsorbents in access oxygen. CO_2, H_2, N_2 and SO_x gases were collected as products. These gaseous products were then separated, purified and each component was analyzed.

4.3.2 Thermal analysis

The decomposition patterns and thermal stability of the prepared adsorbents were acquired using a Perkin Elmer TGA 4000 thermogravimetric analyzer (Waltham, USA). A nitrogen purge gas flowing at 30 mL/min and heating temperature running from 30 to 900℃ were used with a constant bar pressure of 3.2. The change in the weight of the sample was recorded against temperature.

4.3.3 Surface morphology

The surface morphology and pore formation of all adsorbents were studied using scanning electroscope microscope (SEM, TESCAN VEGA 3 XMU, LMH, Czech Republic). The SEM was equipped with energy dispersive X-ray spectroscopy (EDS) which was used to determine the elemental composition. The accelerating voltage of 20 kV was used, and the nitrogen gas was purged. The non-electrical conducting adsorbents were firstly sputter coated with ultra-thin coating layer of carbon. Insulation tape was placed on a metal sample holding plate and the sample was molded onto the tape. Carbon was purged into a vacuum cycle (Quorum Q300T ES) using a turbo pump. The sample were then loaded into the chamber and scanning images were captured.

4.3.4 Functional groups accession by Fourier transform infrared spectroscopy (FTIR)

The FTIR spectroscopy was employed to detect the functional groups in each adsorbent using Thermo Scientific NICOLET IS50 FT-IR (Waltharn MA, USA). Both the diamond and germanium accessories were used to analyze all the adsorbents and all the spectra were recorded in a range of 400- 4000 cm^{-1} and resolution of 4 cm^{-1}. Briefly a spatula tip of an adsorbent was loaded on top of the diamond/germanium crystal center and locked down using a gauge arm force. The specific functional groups were therefore recorded in a range of 400-4000 cm^{-1} by sampling clicking "collect sample" on the computer.

4.3.5 Porosity and surface area analysis

The porosity of the adsorbents and specific surface area were determined using a Micromeritics ASAP 2020 (Aachen, Germany) surface area and porosity analyzer at a recording temperature of -196℃. The samples were first degassed at 120℃ for 12 h using N_2 to apply the adsorption/desorption. The surface area and the pore sizes of the adsorbent were then recorded at -196℃

The specific surface area of the adsorbent was calculated using equation below:

$$\frac{p/p_o}{v\,(1-p/p_o)} = \frac{1}{v\,(p/p_o - 1)} = \frac{1}{v_m c} + \frac{c-1}{v_m} * \frac{p}{p_o} \quad (4.3.5a)$$

$$v_m = \frac{1}{(s=1)} \quad (4.3.5b)$$

$$C = \frac{s}{i} + 1 \quad (4.3.5c)$$

Where p is there adsorbate pressure, p_o is the vapor pressure, v is the adsorbed volume, v_m is the monolayer volume and c is the heats of adsorption and liquefaction quantity.

4.3.6 Surface crystallinity analysis using X-ray diffraction spectroscopy

X-ray diffraction was used to study the crystallinity size and phase of the adsorbents using an X-ray diffractometer supplied by Shimadzu-XRD 700 equipped with a Cu Kα radiation

(ƛ- 1.154056 Å) monochromator with a scan speed of 1°/min, 30 mA current and 40 kV voltage.

4.3.7 Surface morphology analysis using transmittance emission microscopy

Transmittance emission microscopy images were acquired using a Jeol JEM-2100F Emission Electron Microscope instrument (JEOL Inc., Akishima, Japan) equipped with a LaB6 source at an accelerating voltage of 200 kV. The samples were prepared by dropping the as-prepared AC samples onto a TEM copper grid of 200 mesh size and coated using a lacy carbon film. A digital charge coupled device (CCD) camera connected to the TEM was used to verify the images of the prepared samples.

4.3.8: Surface elemental composition determination using X-ray photoelectron spectroscopy (XPS)

X-ray photoelectron spectroscopy supplied by Thermo ESC Alab 250 Xi was used to extract photoelectrons and to measure the binding energies of the extracted electrons to identify the elements and compounds present in the sample. The instrument is equipped with an Al Kα radiation (1486.7 eV) monochromator with an X-ray power of 300 W, 900 µm spot size, 20-100 eV pass energy and a pressure < 10^{-8} mBar. The detection limit of the XPS ranges at approximately 0.1 at% with an escape depth of the phot-electrons ranges from 2 to 10 nm. The surface of the adsorbent was sputtered with argon ions while the binding energy regions of specific elements were being monitored. In this manner, information from subsequent layers beneath the outer surface are obtained.

4.4 ADSORPTION STUDIES

Cr(VI) adsorption studies were conducted using AC-Fe_3O_4, AC-Fe_3O_4-SiO_2 and AC-Fe_3O_4-SiO_2-PEI adsorbents in batch mode. In all cases, duplicate experiments were conducted. For each pair of experiment, 0.05 g of the adsorbent was added to 30 mL solution of chromium

(VI). An ultrasonicator (Scientech ultrasonic cleaner 703) was used to conduct all adsorption experiments. The sonicator was set to low frequency H1 and kept constant throughout. The total chromium and chromium (VI) remaining after adsorption was determined using a flame atomic absorption spectrometer (AAS) and UV-Vis respectively.

The effects of different parameters pH 1, 3, 5, 7, 9, 12, contact time (5, 10, 20, 40, 60, 90, 120 and 150 min), mass of adsorbent (0.05, 0.10, 0.15, 0.20, 0.25 and 0.30 g), initial Cr(VI) concentration (1, 2.5, 5, 7.5, 10 and 12,5 mg/L) and temperature (25 , 35 and 45℃), on the removal of Cr(VI) were studied. Firstly, the pH of the solution was varied from pH 1, 3, 5, 7, 9 and 12 using 0.1 M HCl and 0.1 NaOH while keeping other parameters constant (5 ppm initial concentration, 0.05 g mass of adsorbent, 120 min contact time). Similar procedure was carried out for each of the remaining parameters by keeping all other parameters constant while only the parameter being investigated was varied. The percentage removal (%R) and adsorption capacity (q_e) were calculated using Eqn 4.1 and 4.2, respectively.

$$\%R = \frac{C_o - C_e}{C_o} \text{ x } 100 \qquad (4.4.1)$$

$$q_e = \frac{(C_o - C_e) * V}{M} \qquad (4.4.2)$$

where, C_o is the initial concentration (mg/L), C_e is the final concentration (mg/L), M is the mass of the adsorbent (g) and V is the volume of the eluent (L).

4.4.1 AAS instrumentation set up and preparation

A flame atomic absorption spectrometer equipped with an autosampler was used for the analysis of total chromium before and after adsorption. A chromium lamp with a wavelength of 357.9 nm and slit width of 0.7 nm was used. Acetylene was used as a purge gas. Solutions were analyzed without any dilution.

Table 4.2: AAS instrumentation set up.

Parameters	Conditions
Flame type	Air- C_2H_2
Fuel gas flow rate	2.8 (L/min)
Support gas flow rate	15.0 (L/min)
Burner height	9 (mm)
Pre-spray time	3 (s)
Integration time	5 (s)
Response time	1 (s)
Reading repetition	3

4.4.2 UV-Vis experimental set up and sample preparation

All calibration standards and initial concentration solutions were diluted to 100 mL by taking 2 mL of the raw sample. For analysis, 2 mL of the sample, 2 mL of the DPC solution and 0.2 mL of the sulfuric acid were added to 15 mL centrifuge vials. Depending on the colorization, further dilution can be done to 15 mL and the dilution factor can be calculated as:

$DF = V_2 / V_1$

where V_2 = Total volume of the solution and V_1 = Volume of the eluent.

The calibration curve therefore needs to be recalculated due to the dilution through the formula: $C_1V_1 = C_2V_2$ in order to get the exact Cr(VI) concentration prior to dilution. The wavelength of the UV-Vis was then set to 540 nm to obtain the absorbance values. From the absorbance value the concentration of the Cr(VI) can therefore be calculated. The 0.01 M 1,5'-diphenylcarbazide (DPC) solution was prepared by dissolving 0.242 g of DPC in 100 mL acetone and 10% sulfuric acid.

4.4.3 Surface charge analysis

The pH solution of deionized water was varied from pH 1, 3, 5, 7, 9 and 12 in 15 mL centrifuge tubes and recorded on paper. The experiment was conducted in duplicates. About 0,2 mg of the adsorbent was added to each water and the samples were sonicated at room temperature for 1 h. A Zetasizer nanoseries supplied by was used to analyze the sample by measuring the conductivity (mS/cm) and the isoelectric charge (mV) with respect to change in pH. The instrumental parameters were set at an applied voltage of 10 V, count rate of 222.58 K/count and the measuring conductivity of 3.218 mS/cm. The zeta potential versus pH graph was therefore plotted in order to determine the isoelectric charge of the sample.

4.4.4 Reusability studies

The reusability studies were conducted using 0.1 M NaOH and 0.1 M HCl solutions as desorbing solutions. All experiments were done in duplicates for each adsorbent. Briefly 5 mg/L solution of Cr was loaded on the adsorbents by sonication 0.15 g of the adsorbents in 30 mL solution of 5 mg/L Cr for 120 min at 25^{o}C. The solutions were then centrifuged at the speed of 5000 rpm and decanted allowing the filtered adsorbents to dry overnight at 105^{o}C in an oven. The dried Cr loaded adsorbents were then sonicated in 30mL solution of 0.1 M NaOH and 0.1 M HCl solution for 1 h. The solutions were then centrifuged at a speed of 5000 rpm, filtered and analyzed on the ICP to determine the content of Cr in solution. The centrifuged adsorbents were therefore allowed to dry overnight in the oven and prepared for the next cycle of desorption. This procedure was repeated three times in order to measure the reusability cycle of the prepared adsorbents.

4.5 ADSORTION ISOTHERMS

The two-parameter adsorption models, Langmuir and Freundlich isotherms, which describe the relationship between the adsorbate and the adsorbent were used to determine the removal

mechanisms and adsorption behavior of all adsorbents in this study. The Langmuir suggests that the adsorption interaction between the adsorbent and the adsorbate occurs over a homogenous surface and cannot occur beyond a monolayer coverage. The equation used in Langmuir isotherm (Langmuir 1918), is given as (Eqn 4.5.1):

$$q_t = \frac{q_m b C_e}{(1+bC_e)} \quad (4.5.1)$$

where, b is the Langmuir isotherm constant (L/mg), and q_m is the adsorption capacity at equilibrium (mg/g). The Langmuir separation factor (R_L), which gives information about the nature of adsorption, can be calculated using Equation (4.5.2). If the calculated R_L values lie between 0 and 1, the adsorption process is deemed favorable, but when $R_L > 1$ the adsorption of the adsorbate is characterized as unfavorable and a linear adsorption is predicted when $R_L = 1$.

$$R_L = \frac{1}{(1+bC_o)} \quad (4.5.2)$$

Freundlich isotherm on the other hand depicts that adsorption occurs over heterogenous surface with a multi-layered coverage (Freundlich, 1906). A non-linear form equation of Freundlich is displayed as (Eqn 4.5.3):

$$q_e = K_f\, Ce^{1/n} \quad (4.5.3)$$

where K_f is Freundlich's constant (L/g), n is the Freundlich adsorption intensity exponent which describes the adsorption driving force or the surface heterogeneity. The adsorption process is regarded as favorable when the n value is found to be between 1 and 10 (Mashile et al., 2020).

4.6 KINETICS MODELING

To investigate the rate controlling steps and the adsorption mechanisms of Cr(VI) by AC-Fe_3O_4, AC-Fe_3O_4-SiO_2 and AC-Fe_3O_4-SiO_2-PEI, pseudo-first order (Eqn 4.6.1) and pseudo-second order (Eqn 4.6.2) kinetic models were used.

$q_t = q_{e\ (1-exp1^{-kt})}$ (4.6.1)

$q_t = \frac{tk_{2\ .qe^2}}{(1+\ k_2\ tq_e}$ (4.6.2)

Where q_t (mg/g) is the adsorption capacity of the adsorbate at time t, k_1 (1/min) is the PFO is the adsorption and K_2 is the PSO rate constant.

4.7 ELOVICH MODEL

The Elovich model is mostly applied to chemisorption data and expressed as in Eqn 4.7.1.

$q_t = \frac{1}{\beta} \ln (1 + \alpha\beta t)$ (4.7.1)

where β (mg/g) denotes the desorption rate, α (mg/g.min) is the initial adsorption rate and t is the time (min).

4.8 ZETA POTENTIAL

To determine the isoelectric charge, 0.2 mg of each adsorbent was measured into 6 5 mL sample holders. The pH of ultrapure water was then adjusted between 1, 3, 5, 7, 9 and 12 and 10 mL of each suited pH level was added to the 0.2 mg samples. The samples were then sonicated for 1 hour at room temperature. ZetasizerNano series instrument was used to measure the zeta potential of the solution pH and the zeta potential (mV) versus pH was plotted and used to determine the isoelectric point charge of the adsorbent.

4.9 INTRA-PARTICLE DIFFUSION

To further understand the reaction mechanisms and the rate controlling steps of the adsorption of Cr(VI) by these adsorbents, the Weber and Morris (1963) model was used.

$q_t = K_{id}\ t^{0.5} + C$ (4.9.1)

Where ki_d (mg/(g $min^{0.5}$)) is the intra-particle rate constant and C (mg/g) is the intercept that represents the boundary layer thickness. If the plot of q_t versus $t^{0.5}$ passes through the origin then intra-particle diffusion is the rate-limiting step (Tran et al., 2017).

4.10 THERMODYNAMICS

The thermodynamics studies for the adsorption of Cr(VI) by the AC-Fe_3O_4, AC-Fe_3O_4-SiO_2 and AC-Fe_3O_4-SiO_2-PEI adsorbents were conducted at three different temperatures, 25, 35 and 45℃. Parameters such as Gibb's free energy change (ΔG^o), the enthalpy change (ΔH^o) and the entropy change (ΔS^o) were calculated from Eqns 4.10.1 – 4.10.3.

$$\Delta G° = - RT\ln K_d \quad (4.10.1)$$

Where R is the universal gas constant (8.314 J/mol/K), T is the temperature (K) and K_d is the partial coefficient calculated using:

$$K_d = q_e/C_e * v/m \quad (4.10.2)$$

$\Delta H°$ and $\Delta S°$ can be calculated using equation 4.10.3 by plotting Van't Hoffs plot (the graph of $\ln K_d$ against 1/T)

$$\ln K_d = (- \Delta H°) /RT + (\Delta S°)/R \quad (4.10.3)$$

CHAPTER 5
RESULTS AND DISCUSSION

5.0 SUMMARY

This chapter discusses the outcomes obtained from the characterization analyses and adsorption studies described in Chapter 4. The physical and chemical characteristics of adsorbents are discussed in Section 5.1. Section 5.2 outlines the effects of influential adsorption parameters such as the solution pH, time, initial concentration, temperature, adsorbent dosage and reusability on the removal of Cr(VI) by the prepared adsorbents. Kinetic and isotherm adsorption data is discussed in Section 5.3. Section 5.4 presents the thermodynamic parameters while Section 5.5 compares the performance of the prepared adsorbents with some found in literature.

5.1 CHARACTERIZATION OF ADSORBENTS

The prepared adsorbents were characterized using, the elemental analysis, thermogravimetric analysis, scanning electron microscope, Fourier-transform infrared spectroscopy, Brunauer–Emmett–Teller, X-ray powder diffraction, transmission electron microscope and X-ray photoemission spectroscopy.

5.1.1 Elemental analysis

Table 5.1 presents the elemental composition of AC-KOH, AC-Fe_3O_4, AC-Fe_3O_4-SiO_2, hydroxylated-AC-Fe_3O_4-SiO_2, AC-Fe_3O_4-SiO_2-GPS and AC-Fe_3O_4-SiO_2-NH_2. Notably, the KOH modified activated carbon (AC-KOH) exhibited the highest carbon content of about 79.9% and 2% hydrogen content revealing that the material was highly carbonized. This high content in carbon was similar to that obtained by Lesaoana et al. (2019) for untreated AC. The study reported 84.54% C for virgin AC which decreased upon treatment of the AC with

different acidic solutions. The percentage carbon after functionalization of AC with Fe_3O_4 nanoparticles (NPs) decreased with 35%. The decrease in %C was attributed to the high mass ratio of Fe_3O_4 in comparison to carbon atom as demonstrated by the high % residual (55.69) due to Fe and O atoms. Incorporation of SiO_2 to the AC-Fe_3O_4 material led to an increase in %C to 68.30% and in %H to 1.79% while the % residual decreased to 29.47%. The increase in %C and %H was attributable to the attachment of CH_3-CH_2- branches of tetraethyl orthosilicate (TEOS) to the AC-Fe_3O_4 to produce AC-Fe_3O_4-SiO_2 adsorbent. The sulfur content from these samples was <0.1% showing that there were no sulfur present in preparation methods. Hydroxylation of AC-Fe_3O_4-SiO_2 and attachment of GPS and PEI led to an increase in %C and %H. This increase in %C and %H was attributed to the attachment of CH_2- chains of the GPS and the branched PEI. The increase in %N to 3.00% for AC-Fe_3O_4-SiO_2-PEI represents the successful grafting of amine groups of the PEI on the adsorbent. Both the GPS and PEI AC had the highest content of %H as compared to AC-Fe_3O_4 and AC-Fe_3O_4-SiO_2 attributed to the CH_2 bonds.

Table 5.1: Elemental composition analysis of all adsorbents.

Adsorbents	**%C**	**%H**	**%N**	**%S**	**%Residual**
AC-KOH	79.91	2.00	0.41	<0.1	17.68
AC-Fe_3O_4	44.03	1.41	0.25	<0.1	55.69
AC-Fe_3O_4-SiO_3	68.30	1.79	0.44	<0.1	29.47
Hydroxylated- AC-Fe_3O_4-SiO_3	24.90	0.99	0.13	-	73.98
AC-Fe_3O_4-SiO_3-GPS	36.68	6.23	0.045	-	57.05
AC-Fe_3O_4-SiO_3-NH_2	38.54	6.72	3.00	-	51.74

5.1.2 Thermal decomposition studies

The thermogravimetric analysis (TGA) and derivative thermogravimetric analysis (DTA) results for AC-KOH, AC-Fe_3O_4, AC-Fe_3O_4-SiO_2, hydroxylated-AC-Fe_3O_4-SiO_2, AC-Fe_3O_4-SiO_2-GPS and AC-Fe_3O_4-SiO_2-NH_2 are displayed in Figure 5.1. The curves show the thermal stability and decomposition patterns of the adsorbents at varied temperatures. AC-KOH and AC-Fe_3O_4 showed two decomposition patterns whereas AC-Fe_3O_4-SiO_2 showed three decomposition patterns. The first decomposition step in all the materials was observed at around 100℃ and was quantified to 3%, 2% and 6% weight loss for AC-KOH, AC-Fe_3O_4 and AC-Fe_3O_4-SiO_2, respectively. This decomposition state was attributed to loss of moisture or absorbed water. Slight mass gain was observed for AC-KOH around 300℃ while mass loss was observed around the same temperature for AC-Fe_3O_4 and AC-Fe_3O_4-SiO_2. The weight gain on AC-KOH could be attributable to complete oxidation of some intermediate groups that were not fully oxidized by the KOH treatment (Norouzi et al., 2018b). The mass losses for AC-Fe_3O_4 and AC-Fe_3O_4-SiO_2 could be attributed to loss of volatile compounds from the surface of the AC (Fatehi el a., 2017).

The weight loss stages were much more pronounced for the SiO_2 modified adsorbents probably because of organic molecules/compounds used during attachment of SiO_2 to the AC-Fe_3O_4 material. The volatiles could be SO_2, CH_2, CO, CO_2, NO_2, and aldehydes (Lesaoana et al., 2019). Both AC-KOH and AC-Fe_3O_4 exhibited slow mass loss starting from 350 to 900℃ credited to slow disintegrating of the carbon (Wang et al., 2020).

Besides the slow degradation of AC structure from 350 to 900℃, another small decomposition peak was observed for AC-Fe_3O_4-SiO_2 at around 650℃ attributable to loss of TEOS structure (Wang et al., 2020).

As the AC-Fe_3O_4-SiO_2 was further treated with piranha solution and functionalized with GPS and PEI, the thermal stability and chemical composition of the adsorbents changed. Three decompositions were observed with hydroxylated AC-Fe_3O_4-SiO_2, AC-Fe_3O_4-SiO_2-GPS and AC-Fe_3O_4-SiO_2-PEI, respectively. The first being the dehydration stage occurring between 0 and 400℃ with 10%, 2% and 5% for hydroxylated AC-Fe_3O_4-SiO_2, AC-Fe_3O_4-SiO_2-GPS and AC-Fe_3O_4-SiO_2-PEI, respectively.

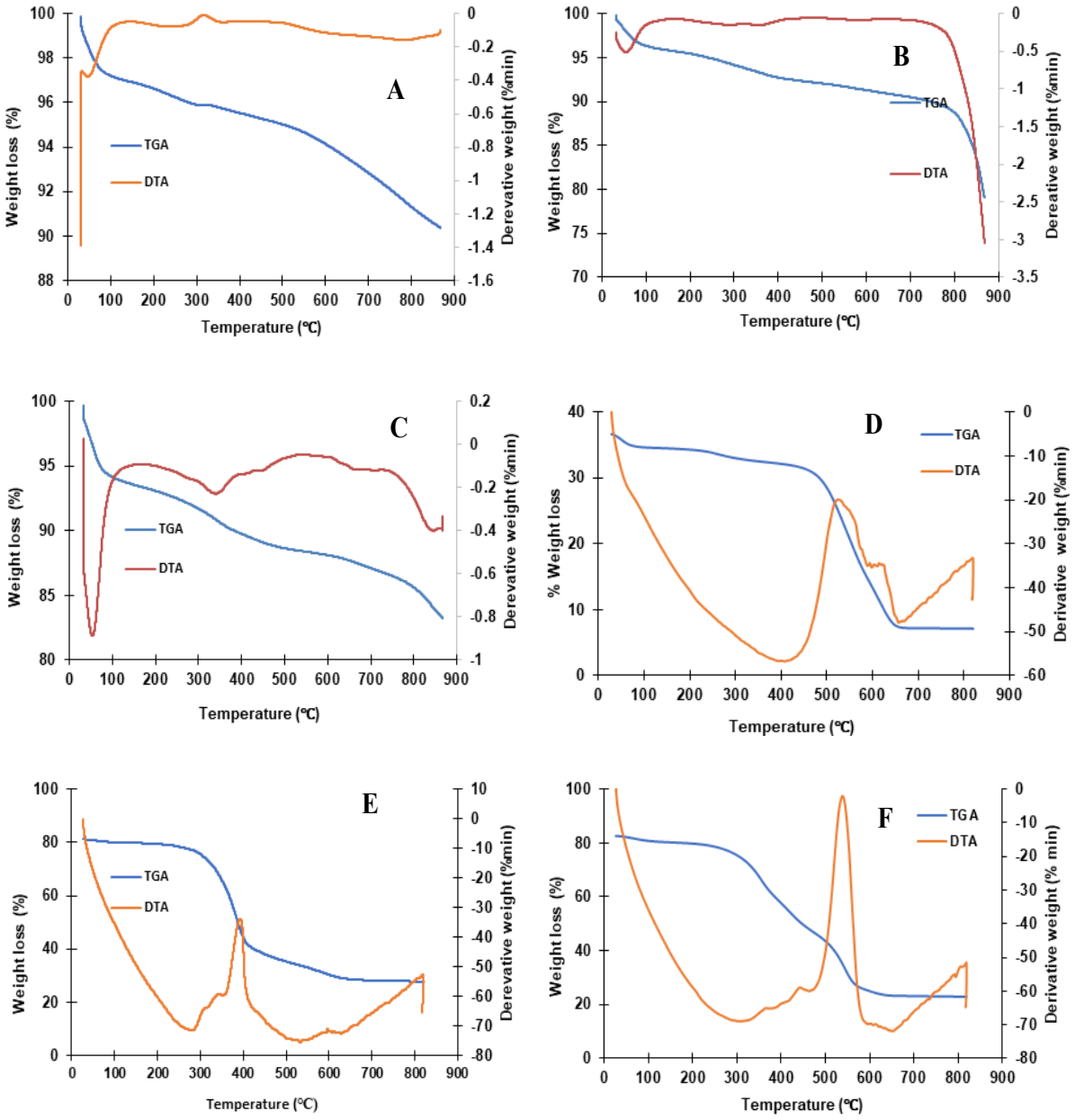

Figure 5.1*:* TGA and DTA of A); AC-KOH; B) AC-Fe_3O_4; C) AC-$Fe_3O_4SiO_2$; D) AC-Fe_3O_4-SiO_2;E) AC-Fe_3O_4-SiO_2-GPS and F) AC-Fe_3O_4-SiO_2-PEI.

The high %weight loss observed with hydroxylated AC-Fe_3O_4-SiO_2 was attributed to high content of –OH groups formed by treatment of the adsorbent with sulfuric acid and hydrogen peroxide. The second decomposition occurred between 400 and 500°C with %weight loss of 10%, 20% and 20% for hydroxylated AC-Fe_3O_4-SiO_2, AC-Fe_3O_4-SiO_2-GPS and AC-Fe_3O_4-SiO_2-PEI. The high %weight loss experienced at this stage was attributed to loss of hemicellulose and volatile compounds. The last decomposition was attributed to loss of lignin structure of the adsorbent.

5.1.3 Surface morphological analysis

SEM images and EDS data of AC-KOH, AC-Fe_3O_4, AC-Fe_3O_4-SiO_2, hydroxylated AC-Fe_3O_4-SiO_2, AC-Fe_3O_4-SiO_2-GPS and AC-Fe_3O_4-SiO_2-PEI are displayed in Figure 5.2 to 5.7. A well-developed microporous structure on irregular shaped AC particles was observed (Figure 5.2). The EDS spectrum showed that the material contained about 95% carbon and 3% potassium. The high %C corroborates that the material is highly carbonaceous while the %K was attributed to the KOH used for modification. Similarly Taslim et al. (2018) reported that the increased porous nature was due to the impregnation of KOH on the AC resulting in larger porous surfaces (Taslim et al., 2018).

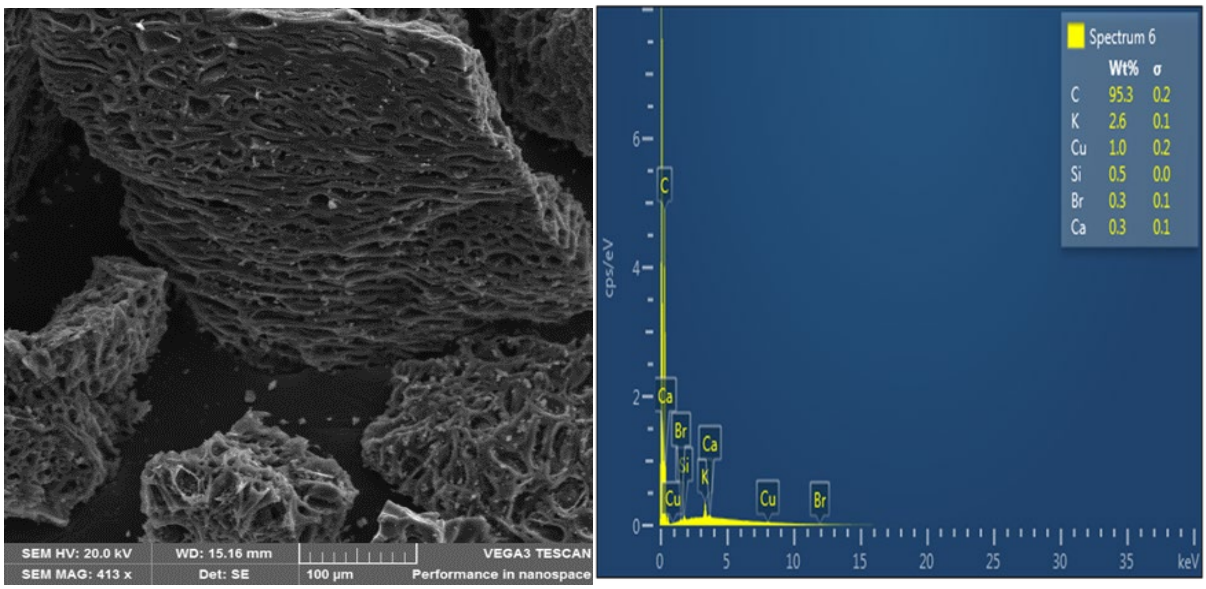

Figure 5.2: SEM image and EDS spectrum of AC-KOH

Figure 5.3 shows a SEM image of AC-Fe_3O_4. The material exhibits high porous nature and small deposits on the surface and pores. The small deposits displayed within the pores were ascribed to the existence Fe_3O_4 precipitates of the magnetite. These deposits were also observed by Cai et al. (2018) as uniform Fe_3O_4 microspheres in the pores of the PAC. These postulations were corroborated by the presence of 10.5% Fe in the EDS spectrum (Figure 5.3) suggesting the successful attachment of Fe_3O_4 nanoparticles to the AC surface.

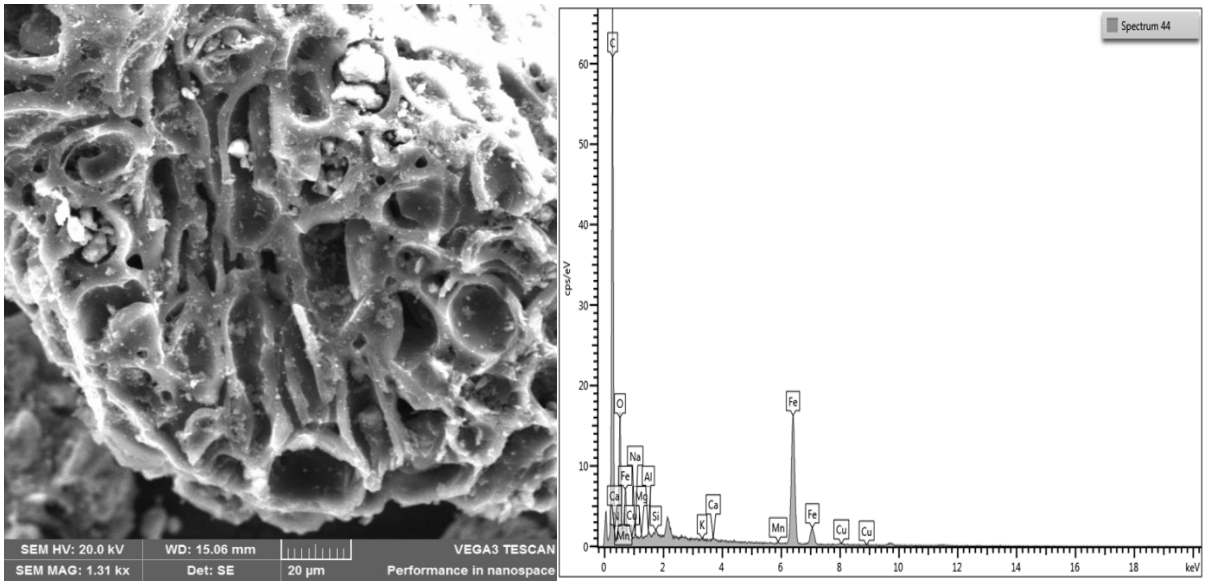

Figure 5.3: SEM image and EDS spectrum of AC-Fe_3O_4

The SEM image of AC-Fe_3O_4-SiO_2 demonstrated an increased precipitation inside the AC pores as well as amorphous structures. The amorphous structure was attributable to the incidence of silica nanoparticles. The presence of 12.7% Si in EDS data (Figure 5.4) confirmed the incorporation of SiO_2 on the surface of AC-Fe_3O_4. Furthermore, the existence of 17.1% Fe and 25.4% O signified that Fe_3O_4 particles were still intact on the surface of AC after the attachment of SiO_2 onto AC-Fe_3O_4.

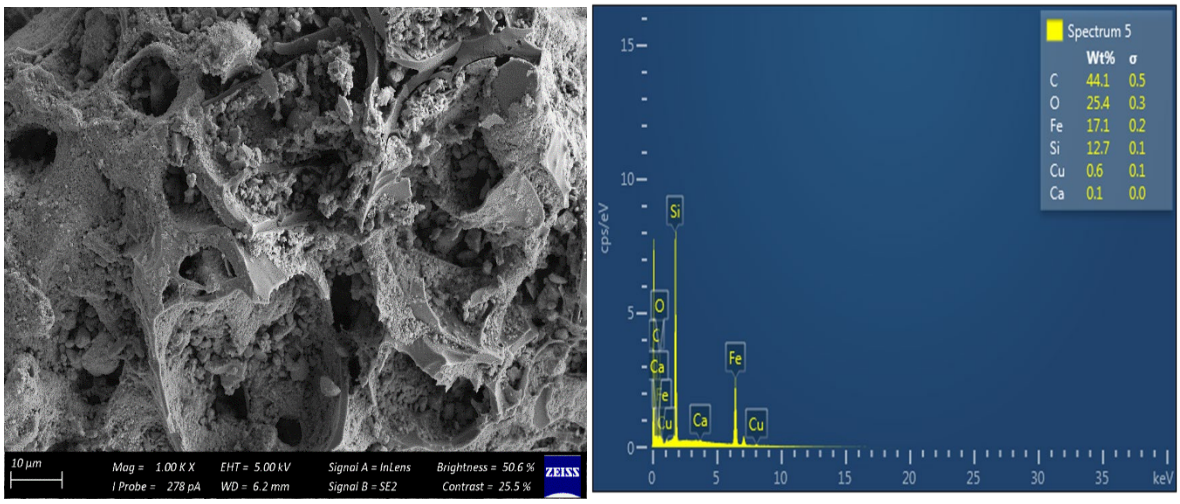

Figure 5.4: SEM image and EDS spectrum of AC-Fe_3O_4-SiO_2

Figure 5.5 illustrates the SEM micrograph and EDS spectrum of hydroxylated AC-Fe_3O_4-SiO_2. The SEM image showed rough flake-like particles inside the pores of the AC depicting the silica layer covering the blackish precipitates of Fe_3O_4. The presence of Si (14.9%) and Fe (9.5%) was confirmed by the EDS spectrum. The decrease in %Fe content was due to the hydroxylation with piranha solution which perhaps have leached some of the Fe_3O_4 precipitates from the composite. An increase in O content from 25.4% for AC-Fe_3O_4-SiO_2 to 39.2% for the hydroxylated AC-Fe_3O_4-SiO_2 inferred successful attachment of -OH groups to the silica-magnetite particles.

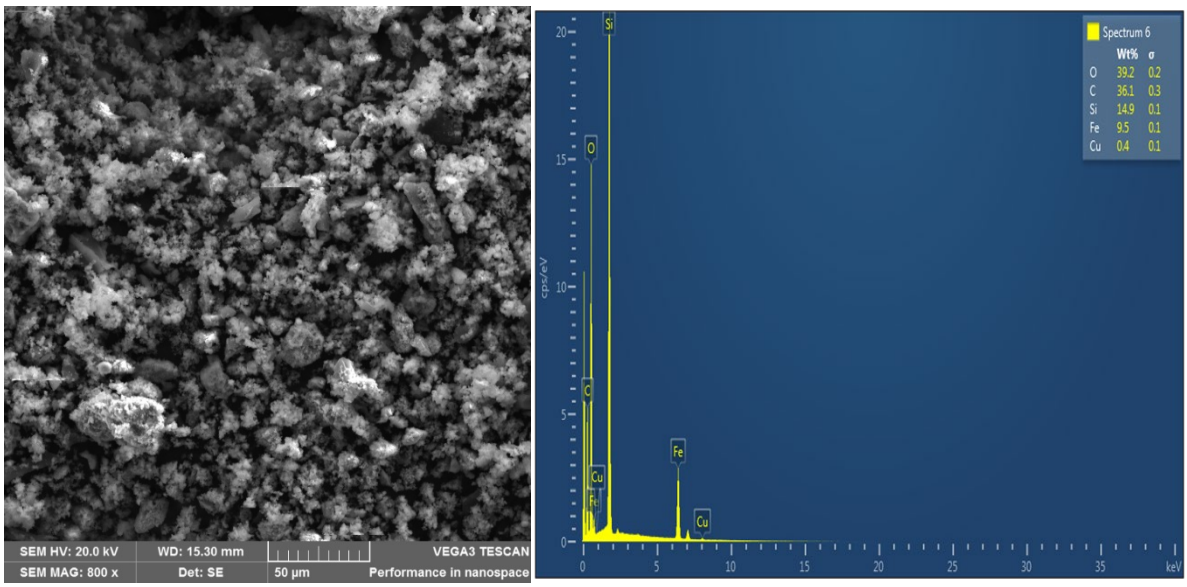

Figure 5.5: SEM image and EDS spectrum of hydroxylated AC-Fe_3O_4-SiO_2.

The SEM image and EDS data of AC-Fe_3O_4-SiO_2-GPS are referred in Figure 5.6. A visibly smooth surface of AC with pores and white precipitates is observed. These surface changes were attributable to the attachment of the 3-glycidoxypropyltrimethoxysilane (GPS) ligand. The increased %C from 36.1% to 48.6% after GPS addition signified its successful attachment. It also seems the attachment of the GPS resulted in leaching or replacement of Fe_3O_4 layer by SiO_2.

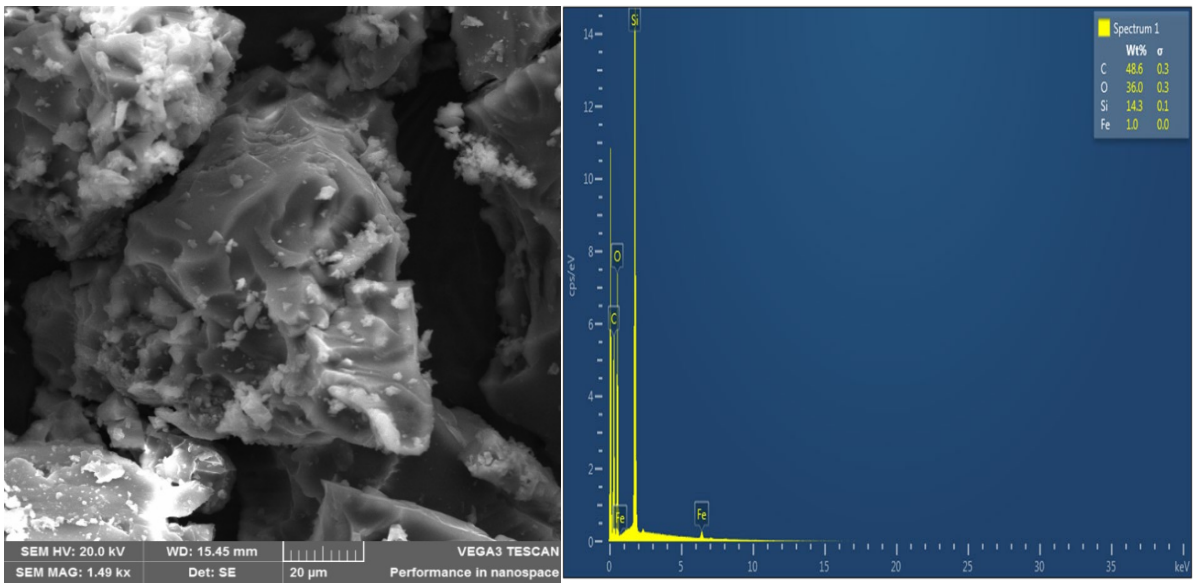

Figure 5.6: SEM image and EDS spectrum of AC-Fe_3O_4-SiO_2-GPS.

AC-Fe_3O_4-SiO_2-PEI SEM image and EDS data are shown in Figure 5.7. The surface of the particles appeared smooth signifying their coverage by a gelaceous layer of PEI and less precipitation was observed. The EDS data showed increased carbon percentage to 51.0% which was due to the alkane branches of the PEI. No nitrogen and hydrogen percentages were observed on the EDS due to their low detection limits on the EDS. Similarly, Adio et al. (2019) could not detect %H on EDS due to low detection limits with %N being below 0.5% (Adio et al., 2019).

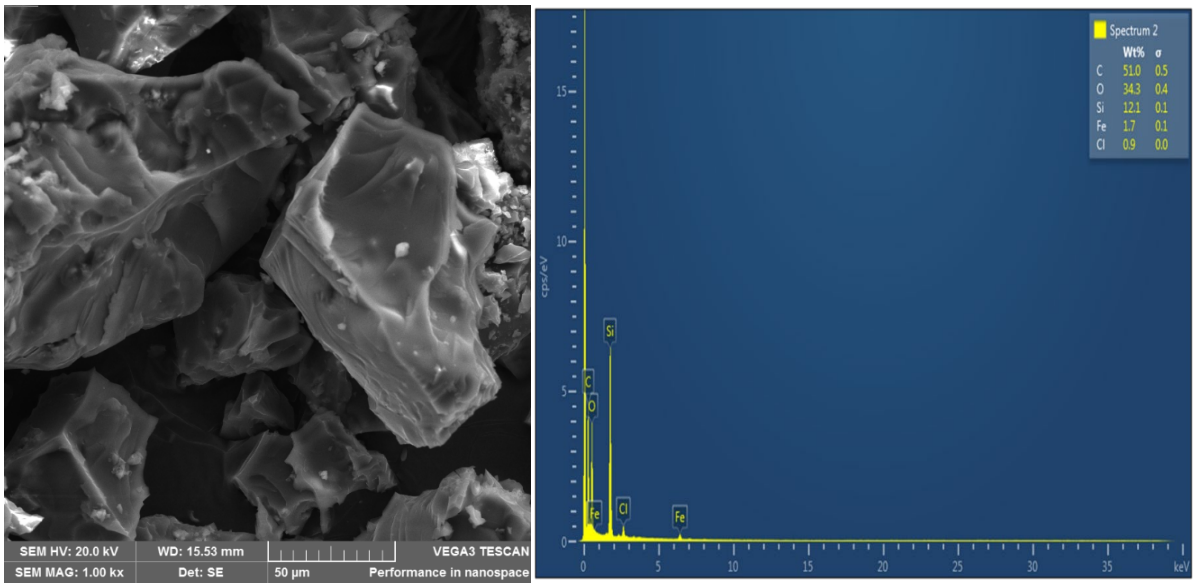

Figure 5.7: SEM image and EDS spectrum of AC-Fe_3O_4-SiO_2-PEI.

5.1.4 Fourier transform infrared (FTIR) spectroscopy results of adsorbents

Figure 5.8A depicts the FTIR spectrum of potassium hydroxide treated activated carbon. The FTIR spectrum showed a lack of oxygenated functional groups such as OH, C=O, and C-O. This was also evident in the EDS data where no O% was recorded. The FTIR spectra of AC-Fe_3O_4 and AC-Fe_3O_4-SiO_2 are depicted in Figure 5.8B and C. In Figure 5.8B and 5.8C, the peaks at 533 to 405 cm^{-1} were assigned to the vibration of Fe-O of the magnetite whereas the peak at 1054 cm^{-1} (Figure 5.8D) was assigned to the symmetric stretch of Si-OH and the 791 cm^{-1} peak was assigned to the symmetric Si-O-Si of the SiO_2 (Fatehi et al., 2018). The presence of the mentioned peaks proved that Fe_3O_4 and SiO_2 were successfully attached on the surface of the AC. Hydroxylation of AC-Fe_3O_4-SiO_2 yielded two new peaks at 3269 cm^{-1} and 1624 cm^{-1} attributable to OH- stretching vibration and bending, respectively. Figure 5.8E relates the FTIR spectrum of the AC-Fe_3O_4-SiO_2-GPS. The characteristic peaks at 1250, 890, and 800 cm^{-1} were assigned to the epoxy and oxirane rings showing successful attachment of the GPS on the AC. The absorption peaks at 2937 and 2869 cm^{-1} were assigned to the C-H stretches from the 3-glycidoxypropyltrimethoxysilane (GPS). The peak at 1010 cm^{-1} of the Si-OH turned

into a shoulder as the GPS was attached showing that the aminopropyl groups were bonded and incorporated to the silicate groups of the SiO_2 (Fellenz et al., 2017). Figure 5.8F shows the spectrum of AC-Fe_3O_4-SiO_2-PEI. The peak at 3289 cm^{-1} was assigned to the –OH stretch that overlapped with the N-H stretch of the primary amine groups of PEI. The absorption peaks at 1657-1568 cm^{-1} were assigned to the N-H amide bands while the peaks at1030 cm^{-1} were assigned to the C-N stretch (Lee et al., 2018). The grafting of PEI resulted in complete removal of the Si-OH peak which were substituted by the aminopropyl groups of the GPS which therefore became a binding path for the amine groups of the PEI. The 1010 cm^{-1} shoulder was therefore replaced by primary amine groups with peaks 1092 and 1030 cm^{-1} (Lee et al., 2020). These peaks are a well representative of the amino groups from the polyethyleneimine (PEI) showing effective attachment. The peaks at 2940 and 2821 cm^{-1} were allocated to the stretching vibrations of the C-H bonds while peaks at 1568 and 1458 cm^{-1} were allotted to the vibration of C-C and bending C-H of the molecular chains of the PEI (El-Sayed and Nada, 2017). The presence of abundant amine groups, carbonyl groups and oxygenated functional groups suggested that adsorption process will occur through chemical interactions.

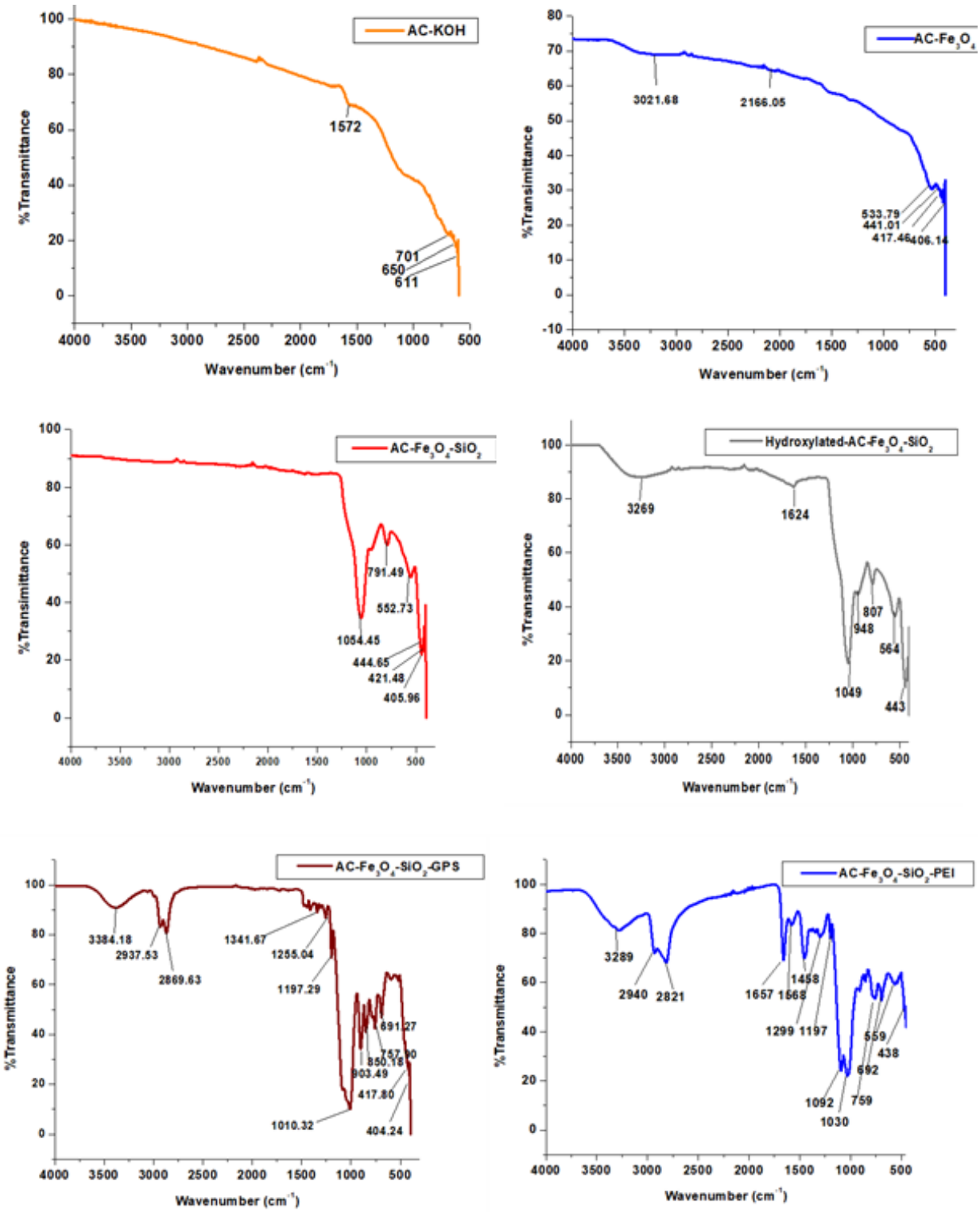

Figure 5.8: FTIR spectra of AC-KOH, AC-Fe_3O_4, AC-Fe_3O_4-SiO_2, AC-Fe_3O_4-SiO_2, AC-Fe_3O_4-SiO_2-GPS and AC-Fe_3O_4-SiO_2-PEI.

5.1.5 Surface area and pore sizes analysis

Table 5.2 portrays the BET specific surface area, pore volume and pore size of the adsorbents. High BET surface area (436 m^2/g) typical of AC was observed for AC-KOH but decreased evidently following functionalization of AC with Fe_3O_4 (387 m^2/g). This can be explained on the basis that Fe_3O_4 nanoparticles occupied and filled the AC pores, thus resulting in lower surface area. A further decrease in surface area (235 m^2/g) was observed upon treatment of AC-Fe_3O_4 by SiO_2. Hydroxylation of AC-Fe_3O_4-SiO_2 resulted in further decrease of surface area to 134 m^2/g. GPS and PEI functionalized AC exhibited surface area values below 1 m^2/g. Interestingly, the pore size of GPS and PEI functionalized AC's were 5- fold higher than that of AC-KOH. It was suspected that the carbon treated AC is lost its morphology completely covered by gelaceous layers of GPS and PEI. Similarly, Cai el al. (2018) observed a decrease in surface area as Fe_3O_4 was loaded on peanut shell activated carbon (MPAC).

The MPAC revealed a surface area of 2430 m^2/g (1.33 cm^3/g pore volume) and to PAC with 3051 m^2/g (1.7 cm^3/g). The decrease in surface area and pore size was explained on a basis of combination of the carbonaceous composition of high surface area of the AC being blocked by spherical Fe_3O_4 particles (Cai et al., 2018). In all adsorbents the pore sizes were above 2 nm [AC-KOH (4.022 nm), AC-Fe_3O_4 (7.85 nm), AC-Fe_3O_4-SiO_2 (5.75 nm), hydroxylated AC-Fe_3O_4-SiO_2 (8.24 nm), AC-Fe_3O_4-SiO_2-GPS (26.5 nm) and AC-Fe_3O_4-SiO_2-PEI (26.9030 nm)], showing that the adsorbents exhibited a mesoporous structure. The smaller pore sizes correlate to the small pore volumes justifying for blockage of pores on the surface of the adsorbent.

Owlad et al (2010) reported a decreased pore volume from 354 cm^3/g for modified palm shell activated carbon to 32.0 cm^3/g for PEI loaded palm shell activated carbon accounting to about 11-fold decrease. The blockage of pores by the loaded PEI onto the surface of the AC was given as one of the reasons for the observed decline in pore volume. The BET results together with the FTIR analysis confirmed the effective incorporation of Fe_3O_4, SiO_2 and PEI on the surface of the AC. The decrease in porosity together with the surface area as displayed by the BET and SEM predicts that the uptake of Cr(VI) by the prepared AC is less likely to occur through the diffusion of the adsorbate to the internal pores of the adsorbent as the porosity is lost as functionalization of ligands occurs on the surface of the AC. Consequently, the adsorption process will less likely occur through physical interactions.

Table 5.2: Porous characteristics of activated carbon.

Adsorbent	**BET surface area (m^2/g)**	**Pore volume (cm^3/g)**	**Pore size (nm)**
AC-KOH	436	0.249	4.02
AC-Fe_3O_4	387	0.294	7.85
AC-Fe_3O_4-SiO_2	235	0.149	5.75
Hydroxylated AC-Fe_3O_4-SiO_2	134	0.107	8.24
AC-Fe_3O_4-SiO_2-GPS	0.0358	0.267	26.5
AC-Fe_3O_4-SiO_2-PEI	0.1491	0.268	26.9

Figure 5.9 illustrates the nitrogen gas adsorption/desorption graph of all the adsorbents. From the graph, the type of adsorption isotherm can be concluded. AC-KOH showed a shape being parallel to the relative pressure (p/p_o) which is typical of a microporous solid sample. The P/P_o is << 1 showing a monolayer adsorption related to a Type I adsorption-desorption isotherm (Zhang et al., 2016). AC-Fe_3O_4, AC-Fe_3O_4-SiO and hydroxylated AC-Fe_3O_4-SiO_2 displayed a hysterical loop as the relative pressure increased to 0.9. This is typical of a mesoporous structure of the adsorbent and is related to a Type II isotherm with a monolayer-multilayer adsorbent. A much larger hysterical loop related to mesoporous structures of AC-Fe_3O_4-SiO_2-GPS and AC-Fe_3O_4-SiO_2-PEI was also observed which denotes a Type IV adsorption-desorption isotherm. Zhang et al. (2016) explained this phenomenon as adsorption occurring on a mesoporous multilayer which is followed by capillary condensation.

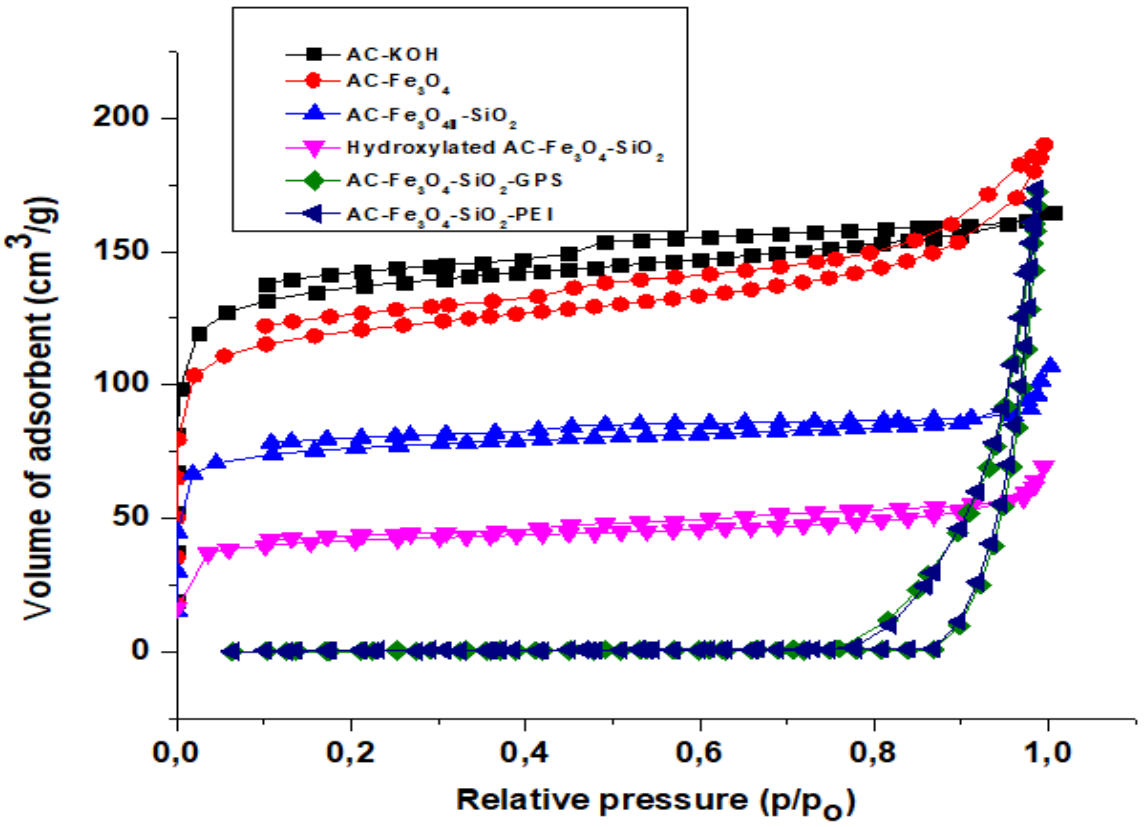

Figure 5.9: N_2 adsorption/desorption isotherms of AC-KOH, AC-Fe_3O_4, AC-Fe_3O_4-SiO_2, hydroxylated AC-Fe_3O_4-SiO_2, AC-Fe_3O_4-SiO_2-GPS and AC-Fe_3O_4-SiO_2-PEI.

5.1.6 Surface crystallinity

The X-ray diffraction patterns of AC-KOH, AC-Fe_3O_4, AC-Fe_3O_4-SiO_2, hydroxylated AC-Fe_3O_4-SiO_2, AC-Fe_3O_4-SiO_2-GPS and AC-Fe_3O_4-SiO_2-PEI are demonstrated in Figure 5.10. The AC-KOH showed an amorphous peak at 2θ = 25° relating to the activated carbon. The amorphous peak of the carbon decreased following the functionalization of AC by the Fe_3O_4, SiO_2 and PEI. AC-Fe_3O_4 and AC-Fe_3O_4-SiO_2 showed five characteristic peaks at 2θ of 30°, 35°, 48° and 65° which were related to 220, 311, 400, 511 and 440 planes according to Bragg's reflection (Cai et al., 2018). These peaks correlate to the magnetite reference with a job card 00-019-0629 showing that Fe_3O_4 was effectively attached on the activated carbon (Fatehi et al., 2018). The peak intensity decreased after hydroxylation but in addition to the five characteristic peaks apportioned to the presence of Fe_3O_4 on the surface of the AC, one peak at 2θ = 15° was observed in hydroxylated AC-Fe_3O_4-SiO_2. The amorphous peak was attributed to the presence of hydroxyl groups. AC-Fe_3O_4-SiO_2-GPS showed an amorphous peak related to the silica from the GPS together with the activated carbon. Traces of Fe were still visible on this adsorbent with 3 Bragg's diffraction peaks at 220, 311 and 422 of the 00-019-0629 magnetite reference (Zhang et al., 2018).

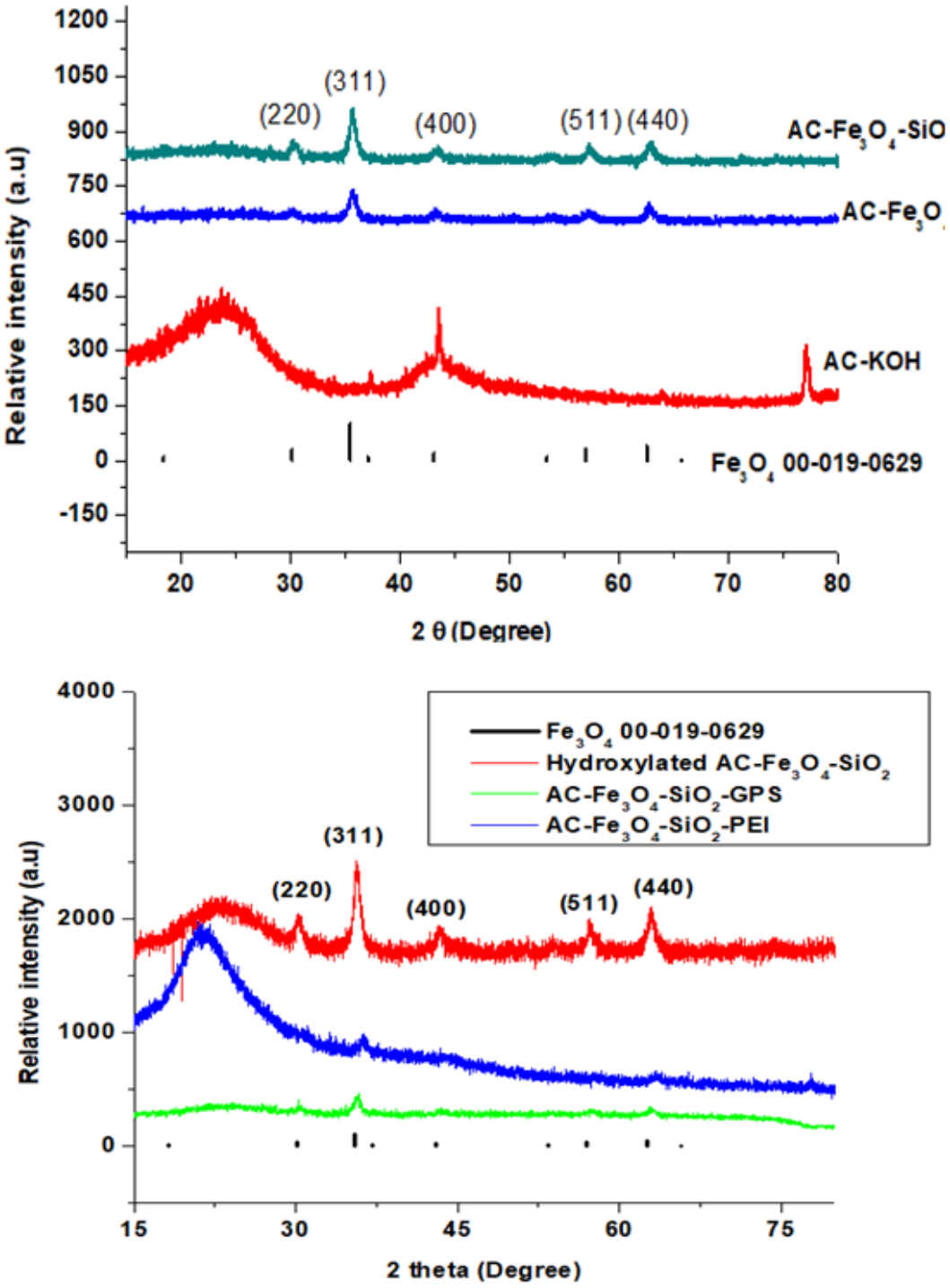

Figure 5.10: X-ray diffraction spectra of AC-KOH, AC-Fe_3O_4, AC-Fe_3O_4-SiO_2, hydroxylated AC-Fe_3O_4-SiO_2, AC-Fe_3O_4-SiO_2-GPS and AC-Fe_3O_4-SiO_2-PEI.

The Scherrer equation was used to calculate the crystal size of the Fe and the results were recorded in Table 5.4.

Scherrer equation: $D = \frac{k\lambda}{\beta cos\theta}$ (5.1)

where, D is the crystalline diameter (nm), K is the dimensionless shape (sphere = 0.89), λ is the X-ray wavelength (Cu, λ=0.154), β is the line broadening at half intensity and θ is the Bragg angle. The crystalline diameters of Fe_3O_4 on activated carbons ranged at 9.5 to 10 nm for AC-Fe_3O_4 and AC-Fe_3O_4-SiO_2 showing efficient loading of Fe_3O_4 on the activated carbon. Hydroxylated AC-Fe_3O_4-SiO_2, AC-Fe_3O_4-SiO_2-GPS and AC-Fe_3O_4-SiO_2-PEI had crystal sizes below 3 nm showing that the adsorbent lost some its magnetic property due to oxidation as functionalization occurred. The decreased crystalline sized were related to the decrease in %Fe from the EDS and surface areas in BET analysis.

Table 5.3: Crystalline diameter D (nm) of all adsorbents based on Scherrer equation.

Adsorbent	**Crystalline diameter (d) (nm)**
AC-KOH	20.42
AC-Fe_3O_4	9.48
AC-Fe_3O_4-SiO_2	9.68
Hydroxylated AC-Fe_3O_4-SiO_2	0.10
AC-Fe_3O_4-SiO_2-GPS	2.62
AC-Fe_3O_4-SiO_2-PEI	0.16

5.1.8 Surface morphology and porosity

Transmission electron microscopy (TEM) was further used to study the morphology and the internal porosity of the prepared adsorbents. It is observed in Figure 5.11A that the AC-Fe_3O_4 displayed darker black particles which were those of the Fe_3O_4 crystallites on top of the AC surface. The lighter particles displayed in Figure 5.11B were attributed to the SiO_2 which covered some of the dark black particles. The AC-Fe_3O_4-SiO_2-PEI showed a different pattern as compared to AC-Fe_3O_4 and AC-Fe_3O_4-SiO_2. Larger crystal shaped spheres were displayed in Figure 5.11C attributed to those of the PEI branches. No black and white crystallites were displayed predicting that the Fe_3O_4 and SiO_2 were completely covered by the gelatinous character of the PEI. Similarly, Geng et al. (2019) relayed presence of layered structures with certain thick shapes as the PEI was attached to the surface of the GO as shown in Figure 5.11D demonstrating that the large shapes are those of the PEI character.

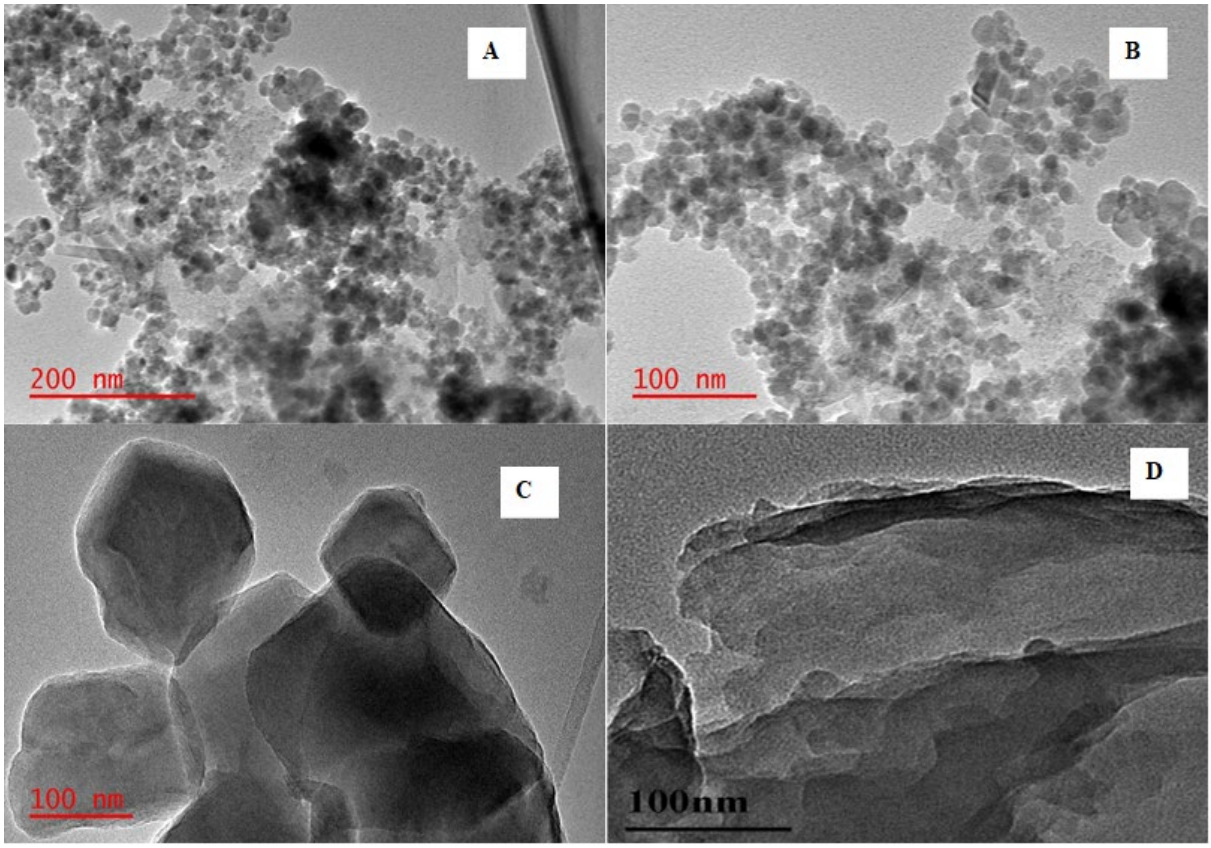

Figure 5.11: TEM image of A) AC-Fe_3O_4; B) AC-Fe_3O_4-SiO_2; C) AC-Fe_3O_4-SiO_2-PEI and D) GO-2PEI (Geng et al., 2020).

5.1.9 Surface elemental composition

The surface compositions of AC-Fe_3O_4-SiO_2-PEI before and after desorption are illustrated in Figure 5.12 - 5.14. The survey spectra (Figure 5.12) showed characteristic peaks of N1s, Cs, Si2p and Cr2p. The Cr2p peak was observed at 561.5 eV after desorption although not as pronounced as other peaks. The diminished nature of this peak was attributed to the low initial concentration of Cr(VI) (5 mg/L) used and its subsequent remnants being left on adsorbent surface after desorption. Geng et al. (2019) also observed the Cr peak at around the same region. The peaks at 284.4, 286.3 and 288.8 eV were assigned to carbon (C1s) representing the bonds of C-C, C-O and O-C=O, respectively in both samples. The similar peaks were observed by Geng et al. (2019) and assigned to the structural backbone of the graphene oxide. The O1s

peak at 529.5 eV represents the metal oxide (Fe_3O_4) attached to the AC. The presence of Si (Si2p 101.5 organic silica) and N (N1s 399.7 organic nitrogen) signified that the attached ligands (SiO_2 and NH_2) were still intact before and after desorption although organic O (O1s at 532.1 eV) was of 30.0% which could be due to SiO_2 and Fe_3O_4 content. However, AC-Fe_3O_4-SiO_2-PEI before desorption displayed no Fe present just as it was observed by the EDS, XRD and FTIR attributing to complete coverage of the AC-Fe_3O_4-SiO_2 surface by gelatinous PEI character. Si (Si2p organic) on the other hand was attributed to the presence of Si in 3-glycidoxypropylmethoxysilane (GPS) which was used for bonding the PEI to the adsorbent surface. Therefore, as the traces of the SiO_2 (Si-OH at 1010 cm^{-1}) from the TEOS was used to attach the GPS, some Si (Si-O-Si 1010.32) was introduced through attachment of the GPS (Fellenz et al., 2017).

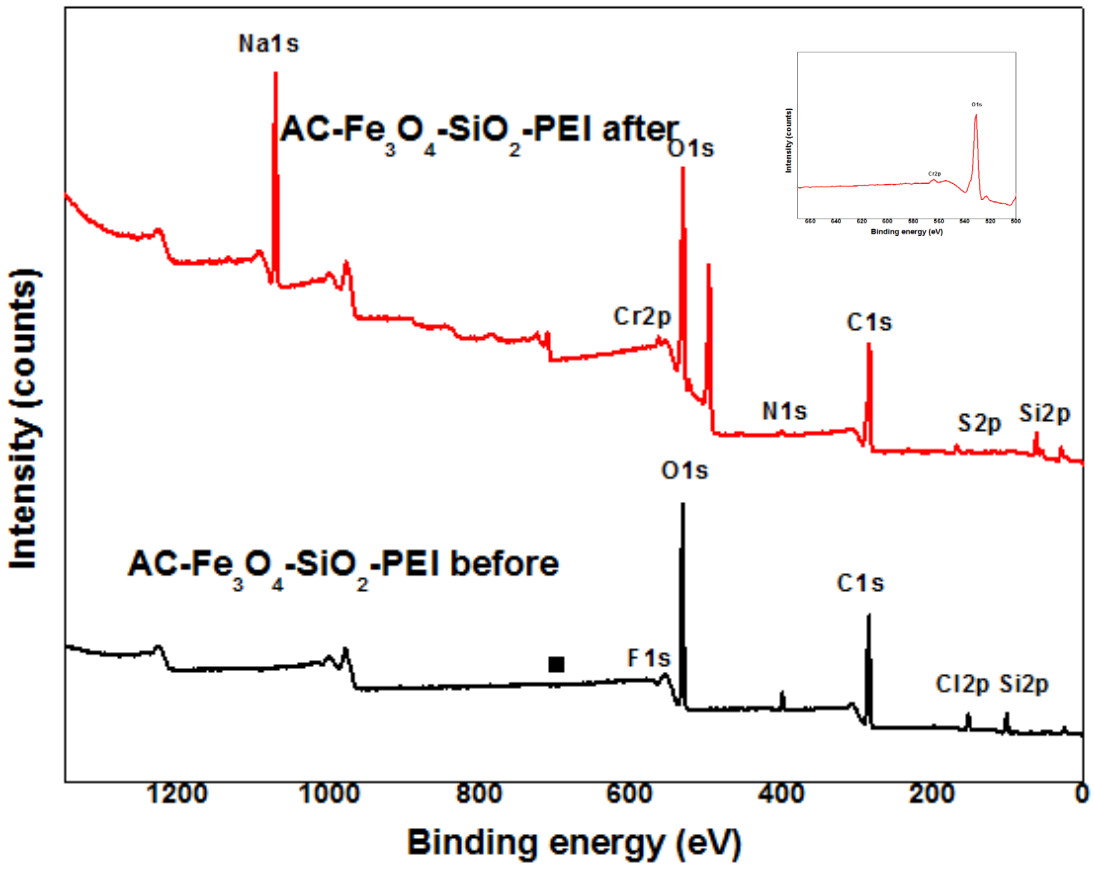

Figure 5.12: Survey XPS spectra of AC-Fe_3O_4-SiO_2-PEI before and after desorption.

The quantity of the Si after desorption also decreased from 8.4% to 0.6%. The gelatinous nature of the AC-Fe_3O_4-SiO-PEI was lost allowing the Fe presence to be observed at 711 eV representing Fe 2p3 Fe_2O_3. This was attributed to the oxidization and leaching of Fe_3O_4 as desorption with NaOH also due to multiple steps occurring before the attachment of PEI which may lead to the oxidization of Fe_3O_4. Three characteristic peaks at 529.5, 531.3 and 533.3 eV were observed and attributed to O 1s metal oxide (4.4%), O 1s C-O (28.0%) and O 1s C=O (4.2%), respectively. The high content of organic O displayed before desorption therefore resulted in formation of these three O bonds predicting that as desorption occurred, the coverage of the Fe_3O_4 and SiO_2 by gelatinous PEI was lost. AC-Fe_3O_4-SiO_2-PEI before adsorption displayed N1s of organic N at 399.8 eV with atomic % of 4.1. After desorption, the

organic N was reduced to atomic% of 1.0 and a new characteristic peak was displayed at 397.9 eV. This peak was attributed to cyanides and azides with atomic % of 0.4 predicting that the polymeric nature of the PEI was converted to cyanides and azides after desorption of Cr(VI) by NaOH.

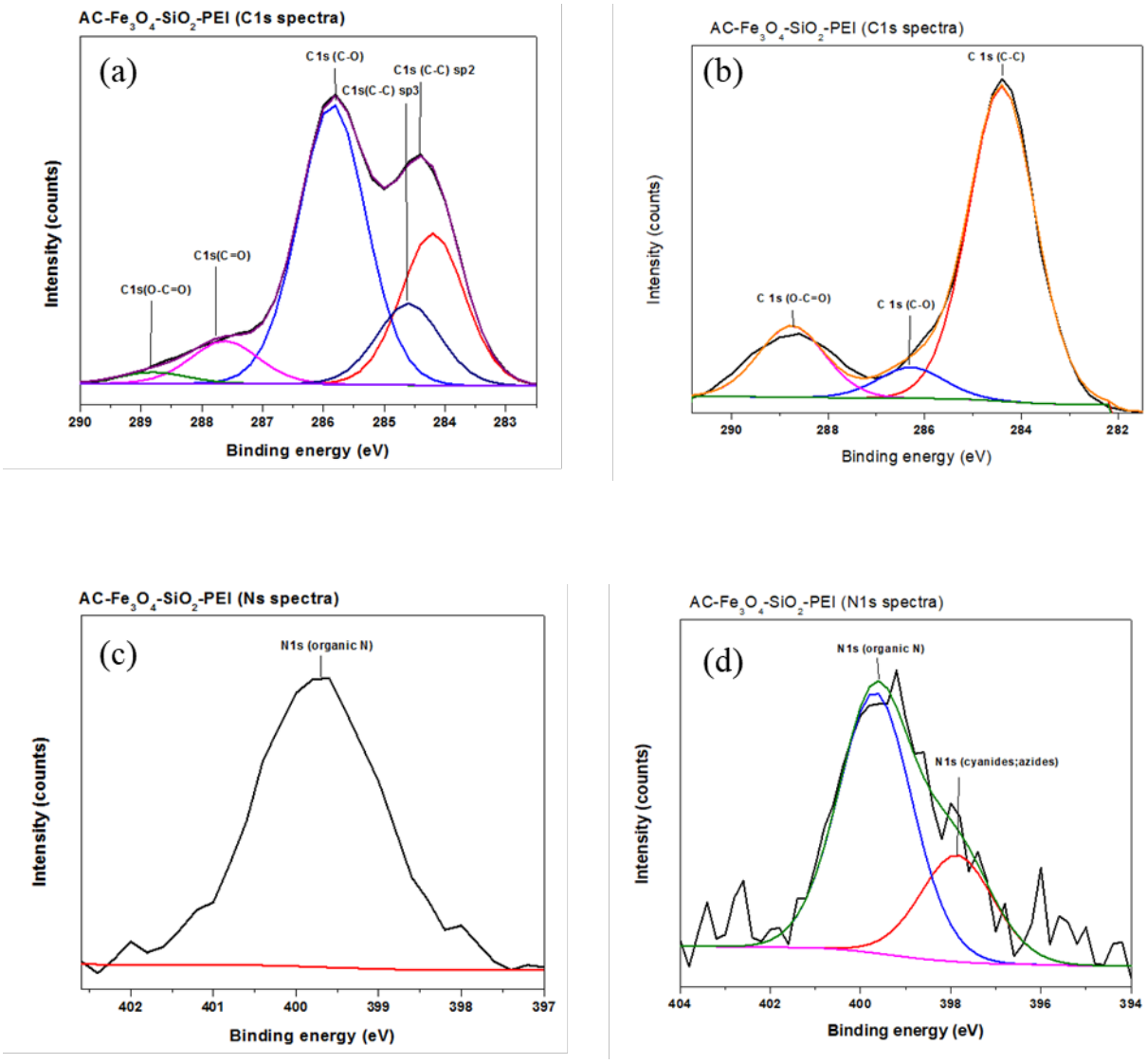

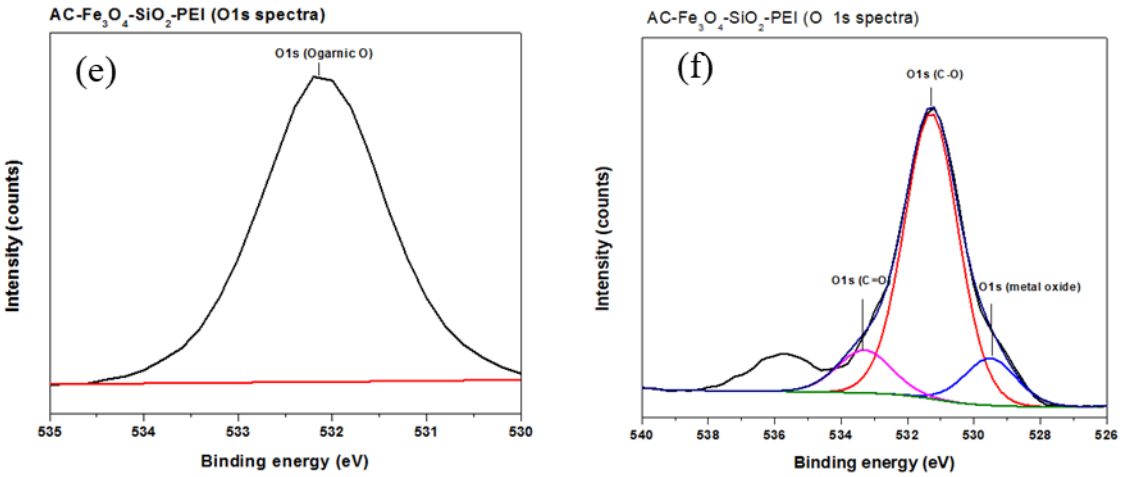

Figure 5.13: XPS spectra of AC-Fe_3O_4-SiO_2-PEI before and after desorption using 0.1 M NaOH solution.

Figure 5.14 shows the Si 2p and Fe 2p spectra of AC-Fe_3O_4-SiO_2-PEI confirming the incorporation of the silica and iron oxides moieties into the structural backbone of the material.

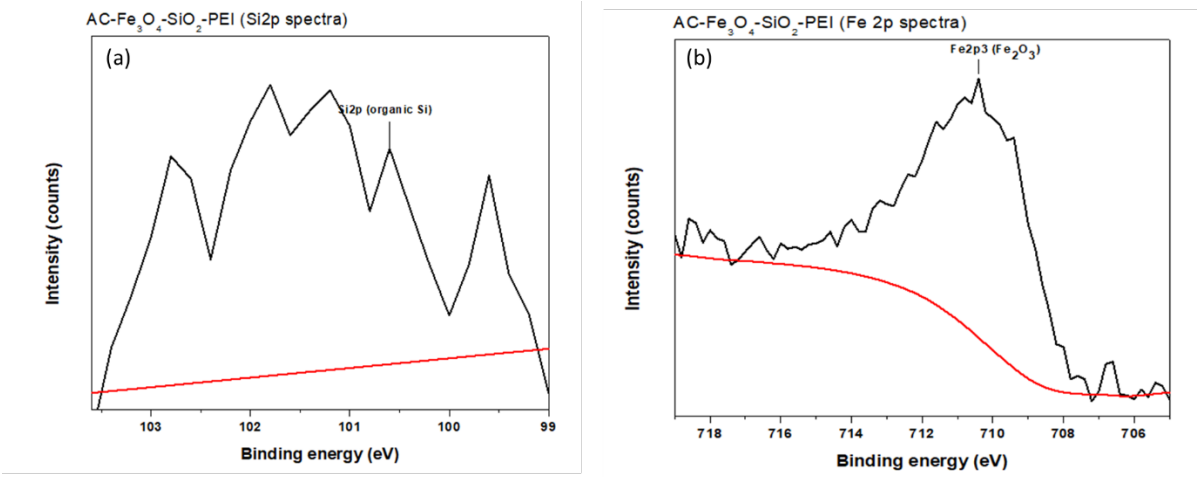

Figure 5.14: XPS spectra of AC-Fe_3O_4-SiO_2-PEI after desorption of Cr(VI) using 0.1 M NaOH solution.

5.2 ADSORPTION STUDIES

In the present study, the adsorption of Cr(VI) by AC-Fe_3O_4-SiO_2-PEI and its intermediate products AC-Fe_3O_4 and AC-Fe_3O_4-SiO_2 was evaluated by adopting a method where one parameter at a time was varied for each of the functional parameters which includes the effect of pH, initial concentration, contact time, and adsorbent dosage concentration. The obtained results are discussed fully in the subsections that follow.

5.2.1 Effect of solution pH

The influence of initial solution pH on the removal of Cr(VI) by AC-Fe_3O_4, AC-Fe_3O_4-SiO_2 and AC-Fe_3O_4-SiO_2-PEI is referred in Figure 5.15A-C. In all the graphs, the % Cr(VI) and Cr(III) removal decreased as the initial solution pH of Cr(VI) was varied from pH 1 to pH 11. In Figure 5.15A (AC-Fe_3O_4) the highest % Cr(VI) removal was observed between pH 1 and 3, with magnitude of 100% and 96%, respectively. For AC-Fe_3O_4-SiO_2 (Figure 5.15B) and AC-Fe_3O_4-SiO_2-PEI (Figure 5.15C) the highest % Cr(VI) removal was observed at pH 1 with quantitative values of 89% and 71%, respectively. The high Cr(VI) removal at acidic conditions (pH 1-3) for all the investigated adsorbents can be explained on the basis that Cr(VI) exists as an oxyanion ($HCrO_4^-$, CrO_4^{2-} and $Cr_2O_7^{2-}$) at acidic conditions and becomes electrostatically attracted to the positively charged surface functional groups of the adsorbent (Yan et al., 2017). Protonation of COOH to $COOH_2^+$, OH to OH^+, and NH_2 to NH_3^+ at acidic conditions results positively charged surface sites (Lesaoana et al., 2019). Besides the electrostatic attraction of Cr(VI) to the positively charged functional groups of the adsorbents at low acidic solutions, reduction of Cr(VI) to Cr(III) due to the presence of electron donating groups like OH, NH_2, SH, COOH and oxidation of Fe^{2+} to Fe^{3+} are other mechanisms of Cr(VI) removal at acidic conditions (Chen et al., 2018).

The higher removal exhibited by AC-Fe_3O_4 compared to AC-Fe_3O_4-SiO_2 and AC-Fe_3O_4-SiO_2-PEI at acidic conditions could be attributed to the effects of adsorption and reduction of Cr(VI) to Cr(III) by Fe^{2+} ions on the surface of AC-Fe_3O_4. The same can be said of silica containing adsorbent (AC-Fe_3O_4-SiO_2). The presence of PEI could enhance repulsion of Cr(VI) due to hydrophobicity of PEI, hence low adsorption. At high pH conditions the NH_2 of the PEI undergo deprotonation resulting in formation NH_2-----OH^- which increases repulsion forces between the negatively charges Cr(VI) and deprotonated NH_2 on the surface of the adsorbent (Zhao et al., 2016). On the other hand, the low removal efficiencies at high pH levels are due repulsion between negative sites on the adsorbent's surface and the anionic Cr(VI) ions in solutions. The negative sites on adsorbent surfaces are caused by the presence of a high concentration of OH^- ions resulting from NaOH solution used for the pH adjustments. These OH^- ions compete for adsorption sites with Cr(VI) ions. The optimum pH used in succeeding studies for AC-Fe_3O_4, AC-Fe_3O_4-SiO_2 and AC-Fe_3O_4-SiO_2-PEI were pH 3, pH 1 and pH 1, respectively.

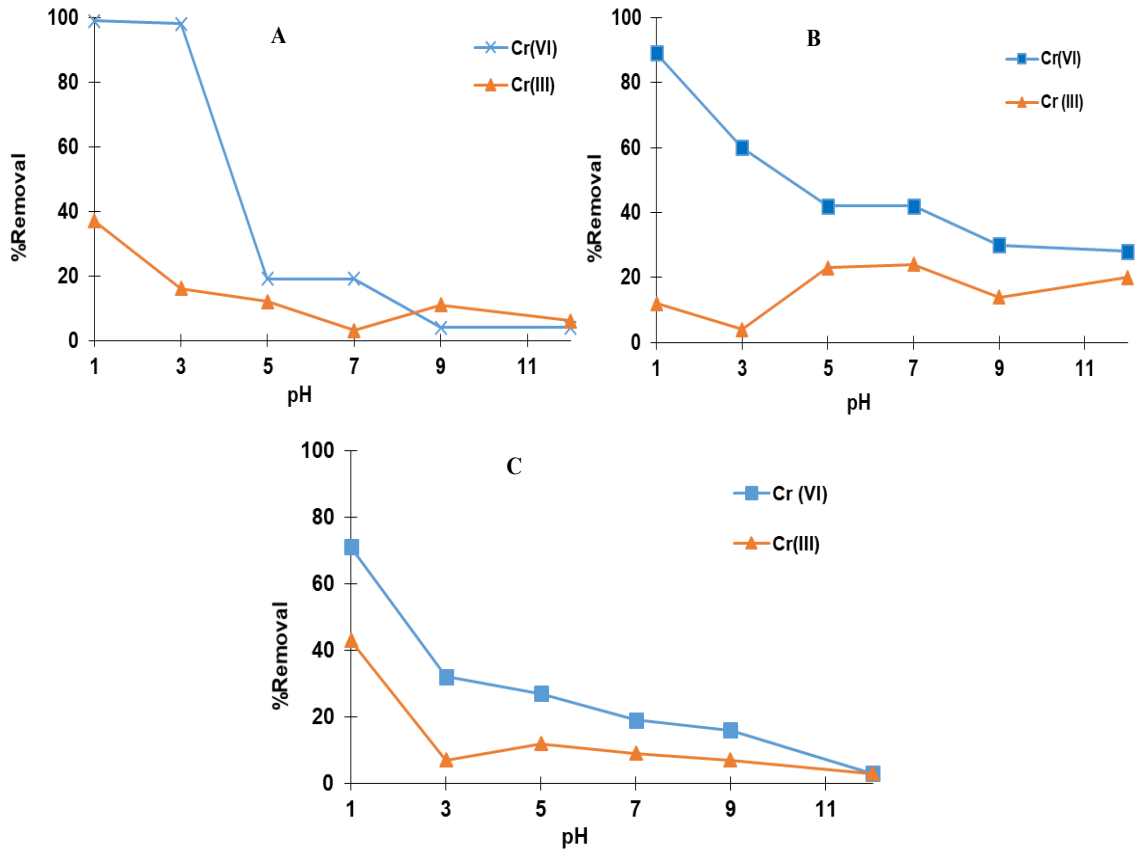

Figure 5.12: Effect of solution pH on the removal of Cr (VI) by A)AC-Fe_3O_4; B) AC-Fe_3O_4-SiO_2 and C) AC-Fe_3O_4-SiO_2-PEI. Experimental conditions: initial concentration 5 mg/L, 60 minutes contact time, 0.05 g amount of adsorbent 25°C temperature and 30 mL solution volume.

5.2.2 Surface charge analysis

The zeta potential versus pH of AC-Fe_3O_4, AC-Fe_3O_4-SiO_2 and AC-Fe_3O_4-SiO_2-PEI is shown in Figure 5.16. The isoelectric point can be determined from the graph as the pH point at which the surface of the adsorbent is zero. It also depicts the point on the internal surface where the adsorbent is positively charged and negatively charged. It is observed that the zeta potential (mV) decreases with increased pH. The isoelectric point (IEP) was found at pH 4.95, 3.53 and 11.69 for AC-Fe_3O_4, AC-Fe_3O_4-SiO_2 and AC-Fe_3O_4-SiO_2-PEI, respectively. AC-Fe_3O_4 and AC-Fe_3O_4-SiO_2 had larger negative zeta potential as compared to AC-Fe_3O_4-SiO_2-PEI. This

was attributed to the presence of functional groups such as Si-O, Fe-O, C=O, C-O, and OH- on the surface of the AC which undergo ionization (Li et al., 2017). The high IEP (pH 11.69) observed for AC-Fe_3O_4-SiO_2-PEI was attributed to the cationic characteristic of PEI (Chen et al., 2016).

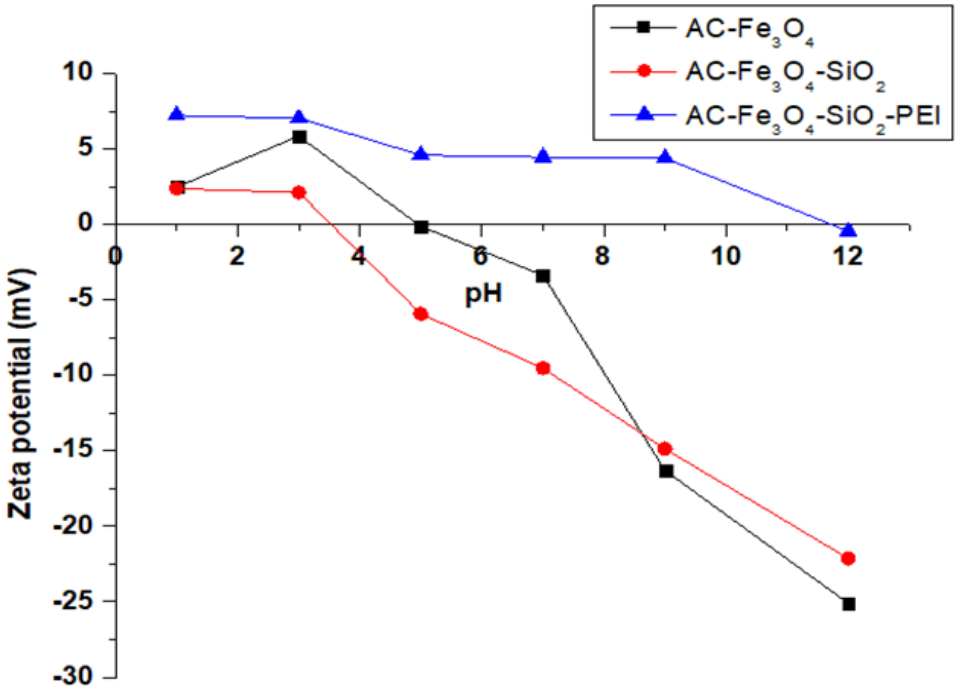

Figure 5.13: Zeta potential of AC-Fe_3O_4, AC-Fe_3O_4-SiO_2 and AC-Fe_3O_4-SiO_2-PEI.

5.2.2 Effect of time

The effect of contact time on the removal of Cr(VI) by AC-Fe_3O_4, AC-Fe_3O_4-SiO_2 and AC-Fe_3O_4-SiO_2-PEI is presented in Figure 5.17. The contact time was varied from 5 to 150 min while keeping other parameters constant. A similar trend of an increase in removal percentage with an increase in contact time was observed for all three adsorbents. From 5 to 10 min the percentage Cr(VI) removal increased from 50 to 70% for AC-Fe_3O_4 and from 40 to 66% for AC-Fe_3O_4-SiO_2 while for AC-Fe_3O_4-SiO_2-PEI the increase ranged from 36 to 45%. The rapid increases for AC-Fe_3O_4, AC-Fe_3O_4-SiO_2 and AC-Fe_3O_4-SiO_2-PEI were quantified to 17.5,

26% and 10%, respectively, for the first 10 min. The rapid uptake of Cr(VI) at these initial times was attributed to onset adsorbent surface coverage by Cr(VI) ions. From 10 to 15 min, there was a slow uptake of Cr(VI) characterized by the diffusion into internal pores. The percent Cr(VI) removal from 10 to 90 min corresponded to 70-83%, 66-75% and 45-64% for AC-Fe_3O_4, AC-Fe_3O_4-SiO_2 and AC-Fe_3O_4-SiO_2-PEI, respectively achieved from 90 min to 150 min.

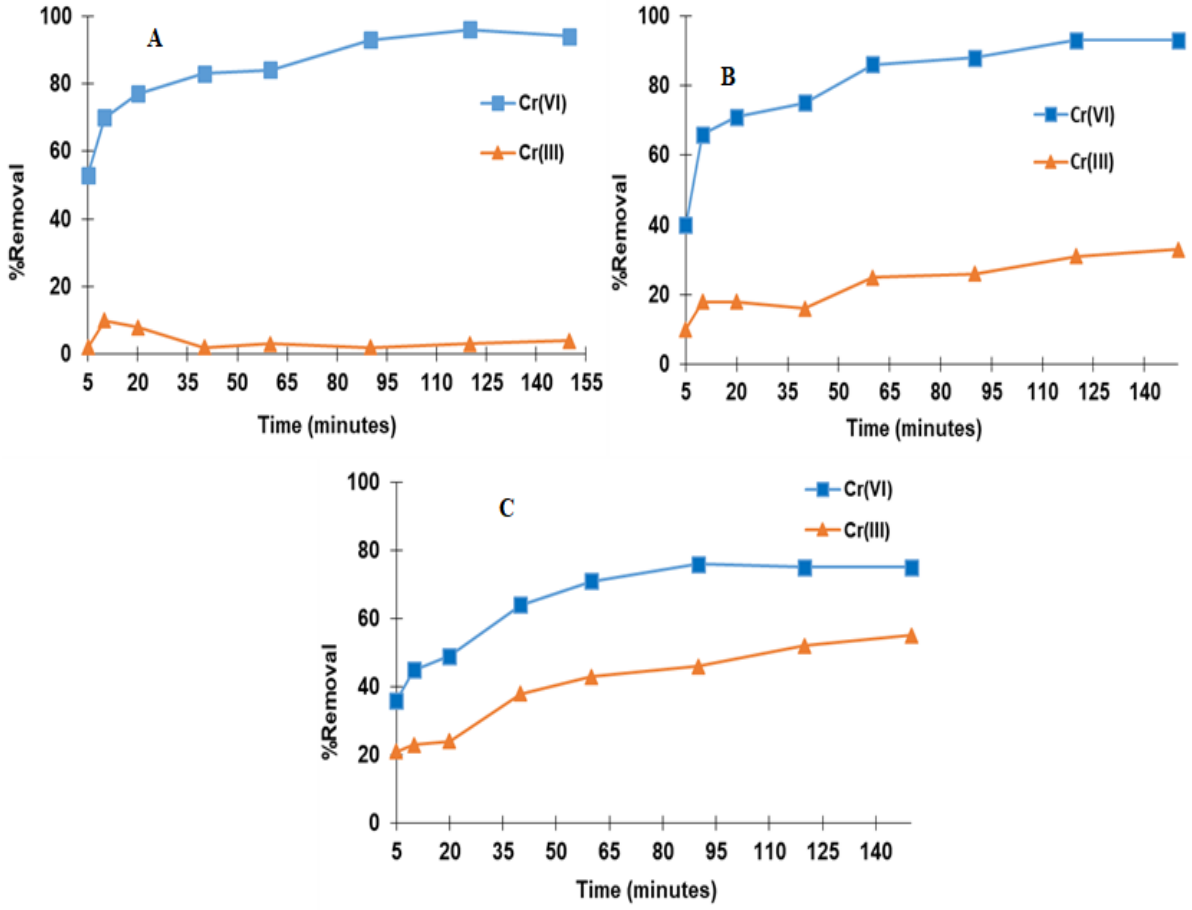

Figure 5. 14: Effect of contact time on the removal of Cr(VI) by A)AC-Fe_3O_4; B) AC-Fe_3O_4-SiO_2 and C) AC-Fe_3O_4-SiO_2-PEI. Experimental conditions: pH 3, 5 mg/L initial concentration, 0.05 g adsorbent mass, 25℃ temperature and 30 mL solution volume.

The maximum Cr(VI) percent removal for each adsorbent was 96% for AC-Fe_3O_4, 93% for AC-Fe_3O_4-SiO_2 and 75% AC-Fe_3O_4-SiO_2-PEI. Low concentration of Cr(III) was observed in Figure 5.17a denoting that there was less Cr(VI) reduction in the presence of AC-Fe_3O_4 but

Figures 5.17A and B show an increase in Cr(III) removal as Cr(VI) removal increased. Such observations could lead to the conclusion that the magnitude of Cr(VI) reduction to Cr(III) was more pronounced when using AC-Fe_3O_4-SiO_2 and AC-Fe_3O_4-SiO_2-PEI adsorbents. Thus, the latter adsorbents have more electron donating capacity than AC-Fe_3O_4.

5.2.3 Effect of initial Cr(VI) concentration and temperature

The influence of initial concentration and temperature on the removal of Cr(VI) by AC-Fe_3O_4, AC-Fe_3O_4-SiO_2 and AC-Fe_3O_4-SiO_2-PEI was studied, and the results are shown in Figure 5.18A-C. The initial concentration was varied from 1 to 12.5 mg/L and the temperature from 25, 35 and 45℃. All other parameters were kept constant. It can be observed that the removal efficiencies for all 3 adsorbents decreased with an increase in Cr(VI) initial concentration. The high removal efficiencies at low concentrations are due less adsorbate molecules to the ratio of adsorbent binding sites, hence 100% removal of Cr(VI) was achieved. At higher concentrations, the number of moles of adsorbate are greater than that of the binding sites in the adsorbent. This results in saturation of binding sites and more Cr(VI) ions available in solution after adsorption leading to lower percentage removal. Temperature seemed to have played no effect on the removal of Cr(VI) however, at higher concentrations (7.5 to 12.5 mg/L) the AC-Fe_3O_4 displayed higher removal efficiencies at 45℃ compared to other temperatures and therefore was chosen as an optimum temperature. The AC-Fe_3O_4-SiO_2 had a constant removal efficiency at all 3 temperatures at 12.5 mg/L concentration. For AC-Fe_3O_4-SiO_2-PEI, the Cr(VI) removal was 100% in all the concentration range studied and to prove this, UV-Vis scans which showed no peak at 540 nm were provided (Figure 5.18D). The scans were done from 400 to 700 nm. However, the FAAS analysis showed that there was still chromium present in the samples after adsorption. This was attributed to the reduction transformation of Cr(VI) to Cr(III) during adsorption. The Cr(III) results show that the percent removal decreased with increasing initial Cr(VI) concentration and was affected by temperature.

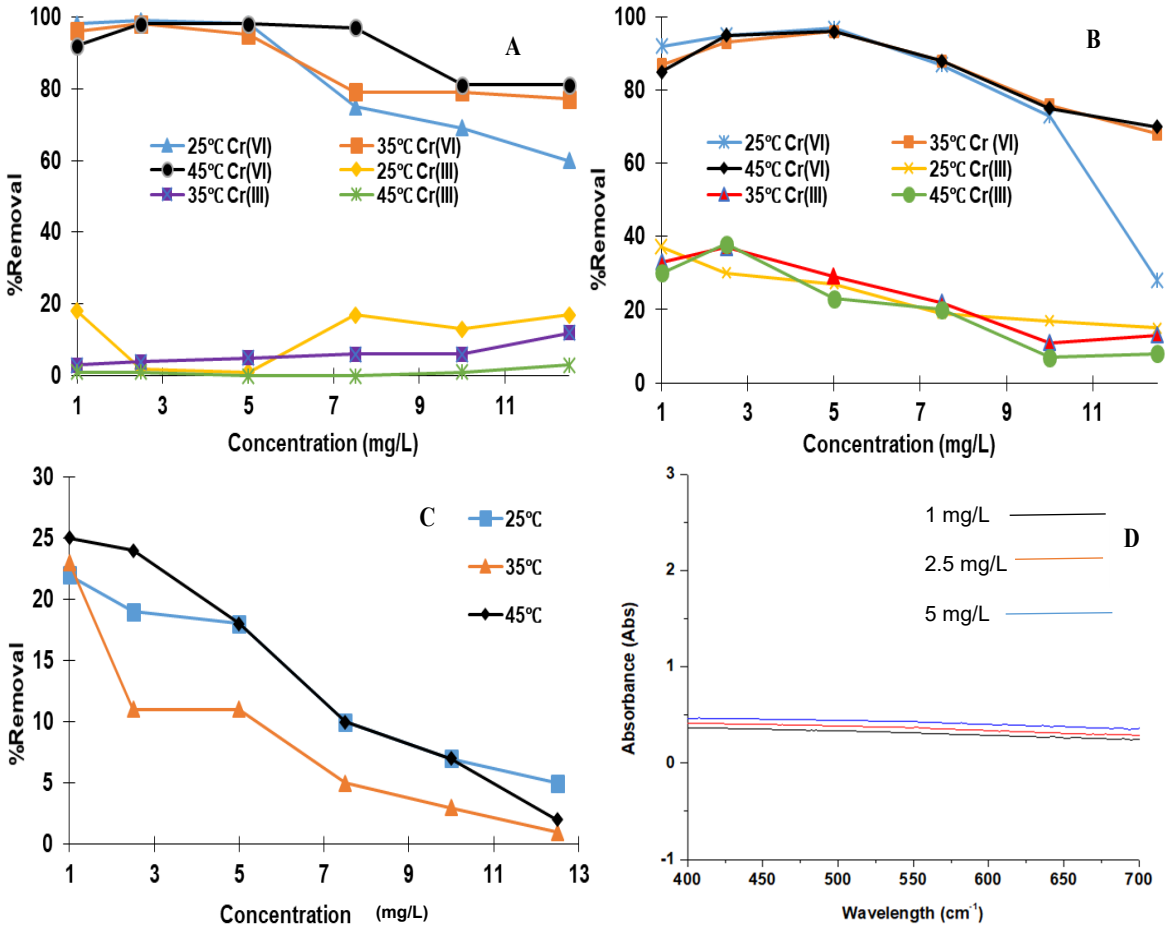

Figure 5.15: Effect of initial concentration and temperature by A)AC-Fe_3O_4; B) AC-Fe_3O_4-SiO_2 and C) AC-Fe_3O_4-SiO_2-PEI on the removal of Cr (VI). Experimental conditions: pH 3, 120 min contact time, 0.05 g adsorbent mass and 30 mL solution volume. D) UV-Vis spectra for the effect of initial concentration and temperature on the removal of Cr (VI) by AC-Fe_3O_4-SiO_2-PEI.

5.2.4 Effect of adsorbent mass

Figure 5.19 shows the influence of adsorbent mass on the removal of Cr(VI) by AC-Fe_3O_4, AC-Fe_3O_4-SiO_2 and AC-Fe_3O_4-SiO_2-PEI. The mass of the adsorbent was varied from 0.05 to 0.30 g while other parameters were kept constant. In all the experiments, the % Cr(VI) removal was almost constant at 100%. The presence of Cr(III) illustrated the extent of Cr(VI) reduction under the studied conditions with the different adsorbents. The removal efficiency increases with an increase in mass of the adsorbent. As the mass of the adsorbent was increased, the adsorption sites for binding of the adsorbate also increased. The optimum mass of the adsorbent was 0.15 g for all 3 adsorbents. The AC-Fe_3O_4 showed less reduction of Cr(VI) to Cr(III) compared to AC-Fe_3O_4-SiO_2 and AC-Fe_3O_4-SiO_2-PEI. The low reduction of Cr(VI) to Cr(III) by AC-Fe_3O_4 was due to the increased Fe ions on the adsorbent which increased the electrostatic attraction resulting in complete uptake of Cr(VI) ions other than reduction. AC-Fe_3O_4-SiO_2 and AC-Fe_3O_4-SiO_2-PEI showed high reduction of Cr(VI) to Cr(III). This can be supported by the decrease in surface area as functionalization occurs as observed by BET surface area. Although the amount of the binding sites increased as the mass of the adsorbent was increased, the surface pores of AC-Fe_3O_4-SiO_2-PEI was too low to capture the Cr(VI) ions. Therefore, the remaining Cr(VI) in solution were reduced to Cr(III).

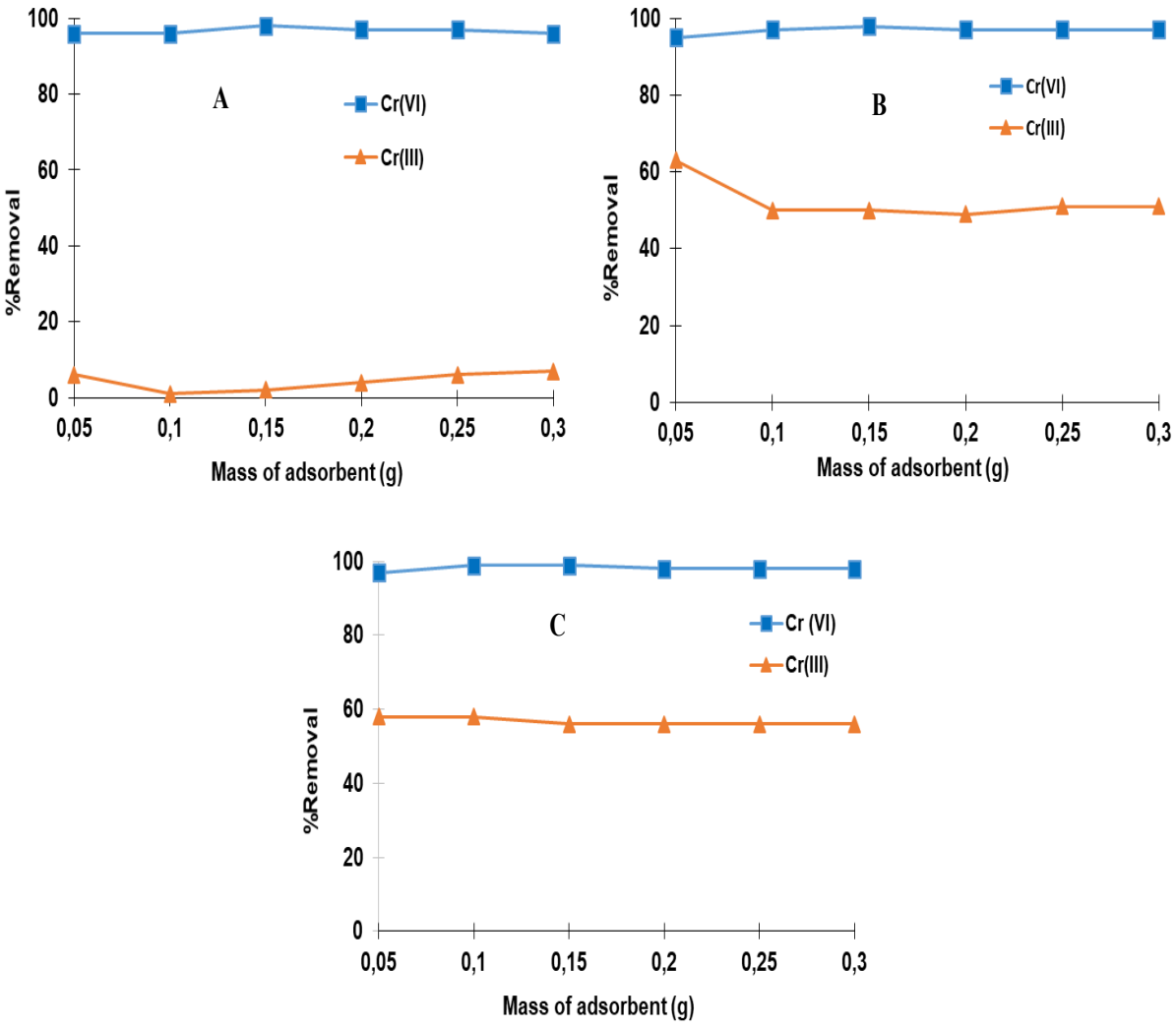

Figure 5.16: Effect of adsorbent mass on the removal of Cr (VI) by A)AC-Fe_3O_4; B) AC-Fe_3O_4-SiO_2 and C) AC-Fe_3O_4-SiO_2-PEI. Experimental conditions: pH 3, 120 min contact time, 2.5 mg/L initial concentration, 45°C temperature and 30 mL solution volume.

5.2.5 Reusability studies

The reusability studies of the adsorbents were investigated by agitating known amounts of adsorbent into known concentrations and volume of Cr(VI) ions. The loaded adsorbents were then transferred into two different desorbing media *i.e.*, 0.1 M HCl and 0.1 M NaOH. The initial Cr(VI) solution concentration were 2.5, 5 and 1 mg/L for AC-Fe_3O_4, AC-Fe_3O_4-SiO_2 and AC-Fe_3O_4-SiO_2-PEI, respectively. The desorption process was done within 3 cycle and each time the total Cr concentration was determined. The desorption recovery/ percentage recovery was calculated as follows:

$$\%\text{Recovery} = \frac{amount\ of\ Cr(VI) desorbed\ (\frac{mg}{L})}{amount\ of\ Cr(VI)\ adsorbed\ (\frac{mg}{L})} \times 100\% \qquad \text{(Norouzi et al., 2018b)}$$

For both desorption reagents, the % recovery decreased with an increase in number of desorption cycles. More of the Cr(VI) was desorbed using 0.1 M NaOH as compared to 0.1 M HCl. The highest %Recovery for HCl was between 4 and 7% for all three adsorbents at the first cycle and decreased for the second and third. This was attributed to the adsorption of Cr(VI) being favorable in acidic conditions due to protonation of functional groups on the surface of the adsorbent resulting in increased electrostatic uptake of Cr(VI) ions (Norouzi et al., 2018b). Therefore, the desorption of Cr(VI) in acidic conditions is expected to be less due to rebinding effects (Ntuli and Pakade, 2019). Although HCl showed less desorption recoveries due to its rebinding ability, some pronounced desorption recovery was observed and attributed to protonation of functional groups such as amines, carbonyls by HCl resulting in increased electrostatic interactions (Ntuli and Pakade, 2019). Cr(III) cations therefore undergo repulsion as they interact with increased protonated functional groups of the adsorbent hence desorption is observed. Better desorption recoveries were observed with NaOH solution. The highest desorption recovery was observed with AC-Fe_3O_4-SiO_2-PEI followed by AC-Fe_3O_4 and AC-Fe_3O_4-SiO_2 being the least with the NaOH solution.

This was attributed to deprotonation of PEI in basic media which increases repulsion forces of the basic solution NaOH (Zhao et al., 2016).

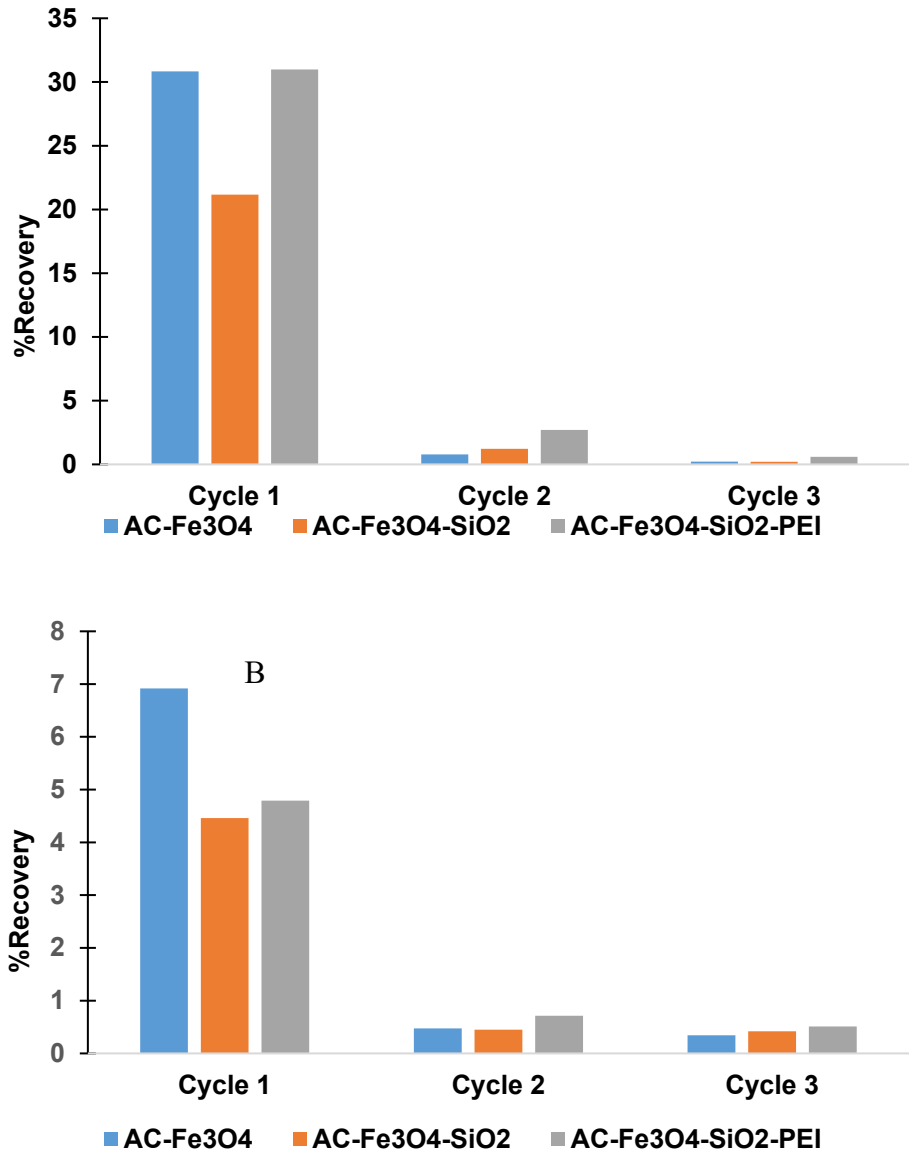

Figure 5.20: Desorption graph of AC-Fe_3O_4 (MNAC-2), AC-Fe_3O_4-SiO_2 (MNAC-3) and AC-Fe_3O_4-SiO_2-PEI (MNAC-6) using A) NaOH and B) HCl.

5.3 ADSORPTION ISOTHERM MODELLING

The equilibrium sorption data of Cr(VI) on AC-Fe_3O_4 at 45℃, AC-Fe_3O_4-SiO_2 at 25℃ and AC-Fe_3O_4-SiO_2-PEI at 45℃ were fitted into Langmuir and Freundlich isotherm models. The results are illustrated in Figure 5.21 and further summarized in Table 5.4. In Figure 5.21a the approximation line of Langmuir lied closer to the data points as compared to the Freundlich estimation.

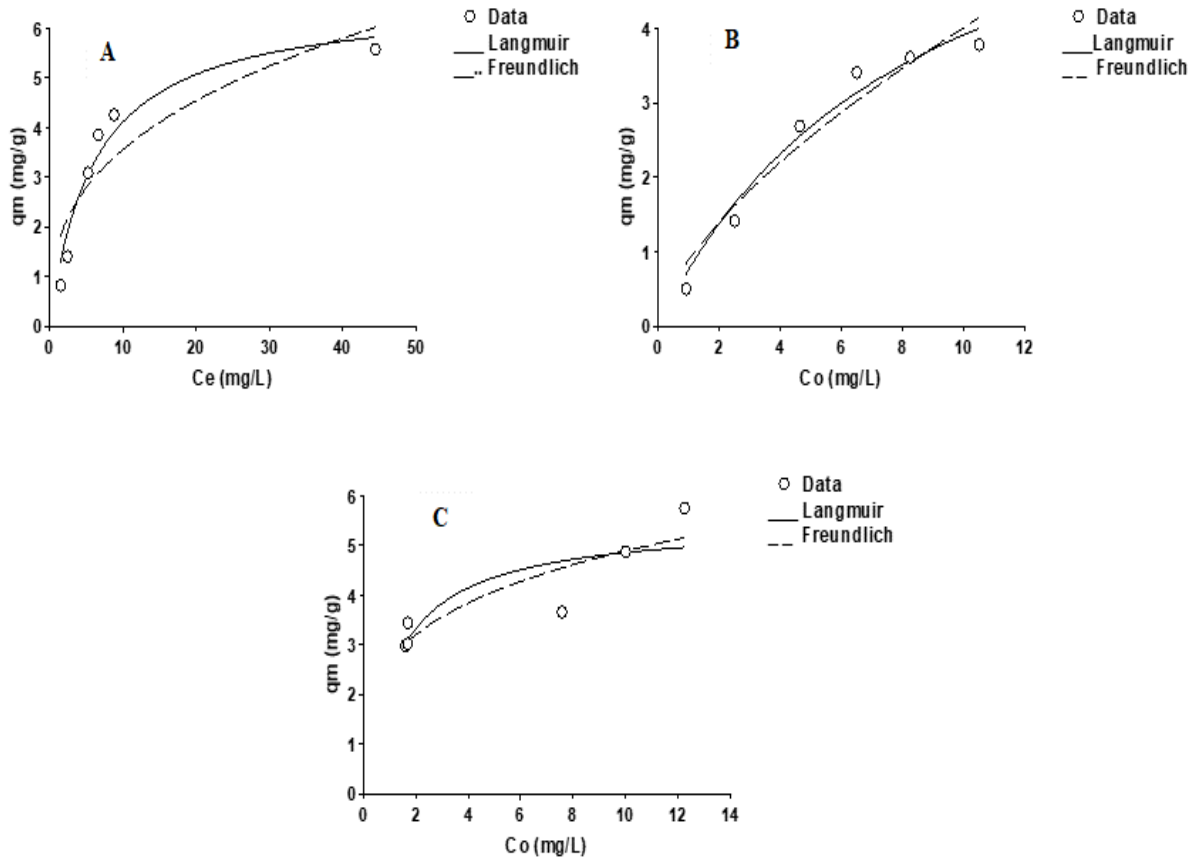

Figure 5.21: Freundlich and Langmuir adsorption isotherms for A) AC-Fe_3O_4; B) AC-Fe_3O_4-SiO_2 and C) AC-Fe_3O_4-SiO_2-PEI.

In fact, the Langmuir isotherm fitting dissected on other data points, proving its accurate estimation. The visual observation was supported by the statistical data shown in Table 5.4. The correlation coefficient (R^2), residual standard error (RSE) and the adsorption capacity (q_m) were used to infer on which isotherm model best fitted the results. The R^2 value for AC-Fe_3O_4 was 0.968 in Langmuir and 0.662 in Freundlich. Similarly, the RSE values were 0.197 and 0.639 in Langmuir and Freundlich, respectively. In this regard, the higher R^2 value and lower RSE in Langmuir concurred with the visual observation that the data was best described by a monolayer, adsorption phenomenon of Langmuir. Also, AC-Fe_3O_4-SiO_2 data fitted to the Langmuir model better using the same reasoning applied above. In addition, the experimental (q_e) and estimated (q_m) adsorption capacity values for AC-Fe_3O_4-SiO_2 were closer to each other for each respective adsorbent. The Langmuir b term ranged between $0 < R_L < 1$ (0.164, 0.332 and 0.713 for AC-Fe_3O_4, AC-Fe_3O_4-SiO_2 and AC-Fe_3O_4-SiO_2-PEI respectively) predicting that the adsorption process was favorable and irreversible (Mashile et al., 2020).

Table 5.4: The Freundlich and Langmuir adsorption isotherm parameters

Isotherms	**Parameters**	**AC-Fe_3O_4**	**AC-Fe_3O_4-SiO_2**	**AC-Fe_3O_4-SiO_2-PEI**
Langmuir isotherm	q_m	6.62	3.92	5.48
$q_e = q_m.b.Ce/(1+b.Ce)$	q_e	5.58	4.40	5.78
	B	0.164	0.332	0713
	R^2	0.975	0.762	0.844
	RSE	0.443	0.878	0.670
Freundlich isotherm	n_f	2.83	2.38	2.67
$q_e = K_f.C_e^{1/n}$	K_f	1.58	1.16	3.81
	R^2	0.897	0.690	0.744
	RSE	0.887	0.982	0.565

5.3.1 Adsorption kinetics

5.3.1.1 Pseudo-first order and second order

The pseudo first order (PFO) and pseudo second order (PSO) were used to study the kinetics of the adsorption processes. Pseudo first order describes the adsorption mechanism occurring through the diffusion of the metal ions onto the adsorbent boundary layer (Geng et al., 2019). The K_1 PFO parameter predicts how fast the adsorption equilibrium is obtained (Wang et al., 2020). A low K_1 value with high C_o values predicts that the adsorption rate is slow (Wang et al., 2020). Although PFO and PSO are empirical models, few physical meanings have been expressed by Wang et al. (2020). It is explained that PFO suggests that the adsorption process occurs at the initial state of the reaction where the t is at 0 min. Pseudo second order on the other hand, predicts the adsorption process occurs at the final stage of the reaction where equilibrium is reached. Another physical meaning predicts that the adsorbent consists of few active sites for PFO concluding that the adsorption process may occur through external diffusion or internal diffusion (Wang et al., 2020). PSO on the other hand predicts that adsorbent consists of relatively abundant active sites. The adsorption capacity data for the prepared adsorbent was drawn as a function of time and fitted to the PFO and PSO as displayed in Figure 5.22. It is observed that the experimental data was best fitted to PSO for all three adsorbents. However, this can be confirmed based on the kinetic parameters outlined in Table 5.5. The correlation coefficient (R^2) and the residual standard error (RSE) were used to conclude which rate model was best fit. PSO had the highest R^2 of 0.974, 0.974 and 0.962 and low RSE values of 0.093, 0.116 and 0.183 for AC-Fe_3O_4, AC-Fe_3O_4-SiO_2 and AC-Fe_3O_4-SiO_2-PEI, respectively.

The closeness of q_m and q_e were also used to reach a conclusive agreement of the best fit to PSO. These observations predict that PSO was best fit to the adsorption of Cr(VI) by AC-Fe_3O_4, AC-Fe_3O_4-SiO_2 and AC-Fe_3O_4-SiO_2-PEI. Even though not conclusive on its own, the PSO predicts the adsorption process to occur through chemical interactions. Similar inferences relating the PSO and chemisorption processes were made by other researchers (Mashile et al., 2020; Wang and Guo, 2020).

5.3.1.2 Elovich model

Elovich model is an empirical model mostly applied to chemisorption data (Tran et al., 2016) It can be suggested that the activation time increases with adsorption time and that the adsorption process occurs over a heterogeneous surface (Wang and Guo, 2020). The high R^2 value and the RSE values obtained as compared to those of the PFO and PSO supported that the adsorption occurred through chemisorption. The α constants therefore describes the initial adsorption rate constant and the β describes the extant at which the surface is covered (desorption rate) (Mashile et al., 2020). The high α shows that the adsorption process is slow which could be obtained by either by internal or external diffusion (Wang and Guo, 2020).

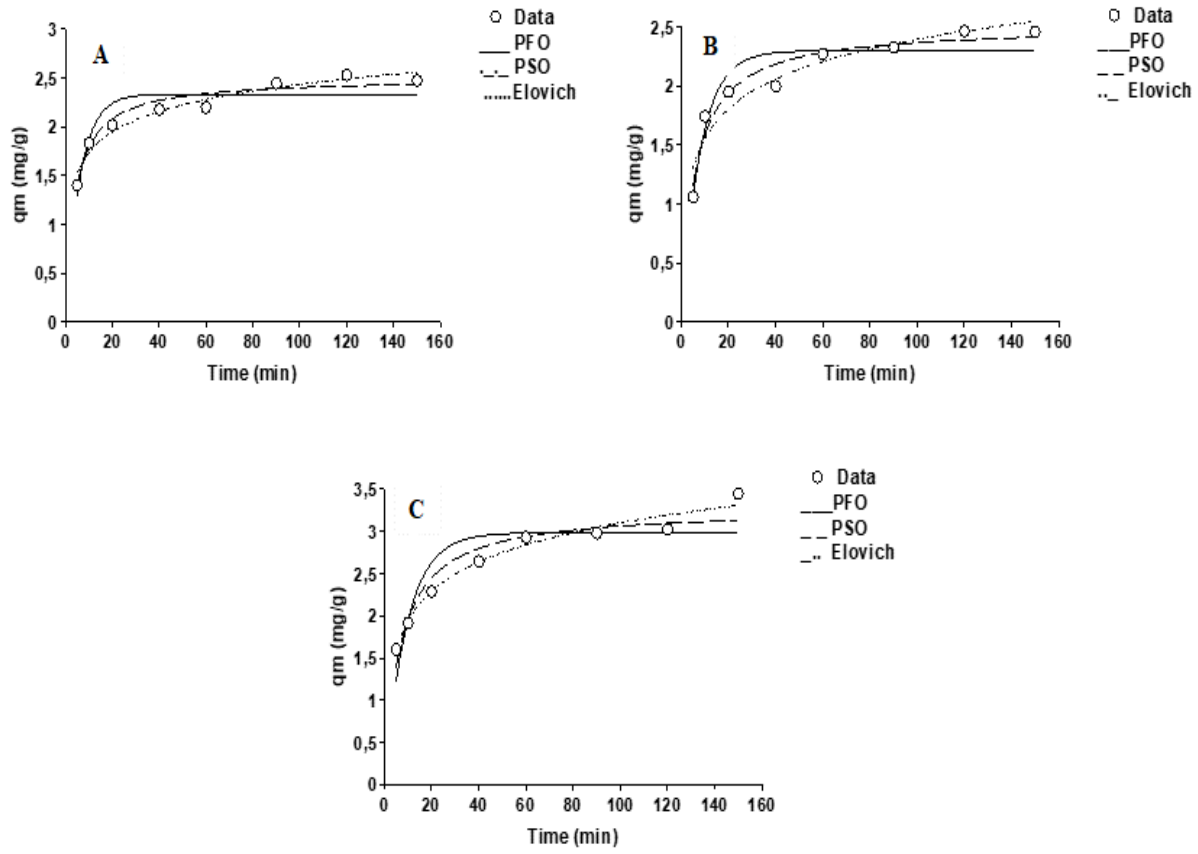

Figure 5.22: Pseudo-first order, second order and Elovich modelling for A) AC-Fe_3O_4; B) AC-Fe_3O_4-SiO_2 and C) AC-Fe_3O_4-SiO_2-PEI.

5.3.1.3 Intra-particle diffusion

Adsorption process occurs through various stages which involve the transportation of the adsorbate from solution to the surface of the adsorbent. The four stages mainly being (i) bulk transportation (direct transfer of the adsorbent into adsorbate solution) occurring immediately after exposure of adsorbent particles to the adsorbate solution, this process is fast and cannot be used to conclude the reaction mechanism; (ii) film diffusion/ external diffusion, a slow process which involves the transportation of the adsorbate molecules through a hydrodynamic boundary layer or film to the external surface of the adsorbent; (iii) the intra-particle diffusion/ internal diffusion (slow) which involves the diffusion of adsorbate molecules to the inner pores of the adsorbent, and lastly, (iv) adsorption (fast) which involves the adsorption of the

adsorbate to the active sites on the surface of the adsorbent (Wang and Guo, 2020), (Tran et al., 2017).

To determine the rate controlling step, a plot qt vs $t^{0.5}$ (Figure 5.23) was used. The plot q_t vs $t^{0.5}$ exhibited multiple linearity displaying that intra-particle diffusion is not the only rate controlling step in the adsorption process. This means that the rate of reaction was controlled by both film diffusion through a boundary layer and by intra-particle diffusion (Mashile et al., 2020).

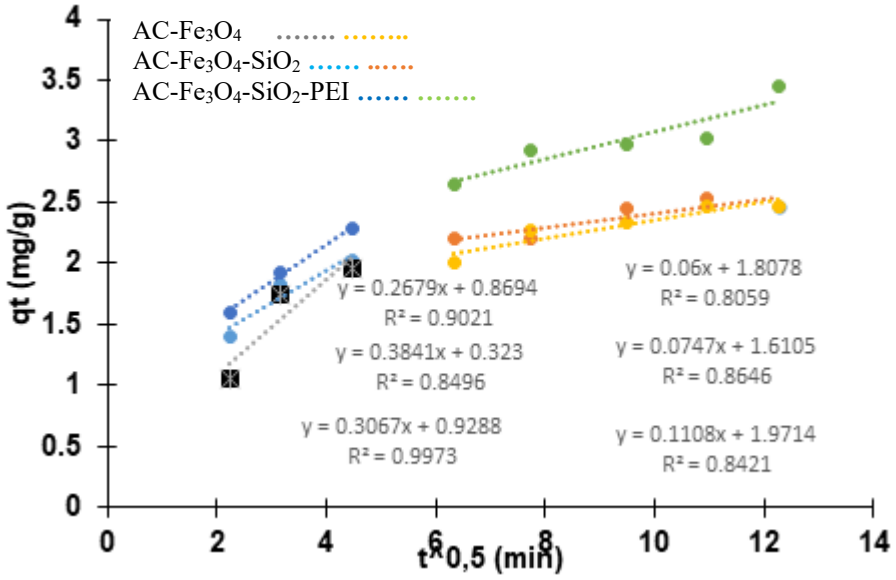

Figure 5.17: Intra-particle diffusion graph of AC-Fe_3O_4, AC-Fe_3O_4-SiO_2 and AC-Fe_3O_4-SiO_2-PEI.

Table 5.5: Kinetics isotherm parameters of AC-Fe_3O_4, AC-Fe_3O_4-SiO_2 and AC-Fe_3O_4-SiO_2-PEI.

Isotherms	**Parameters**	**AC-Fe_3O_4**	**AC-Fe_3O_4-SiO_2**	**AC-Fe_3O_4-SiO_2-PEI**
Pseudo-first order (PFO)	q_t (mg/g)	2.33	2.30	2.98
	q_m(mg/g)	2.53	2.47	2.98
$q_t = q_e(1-exp^{-k_1 t})$	K_1 (1/min)	0.161	0.123	0.106
	R^2	0.911	0.942	0.891
	RSE	0.170	0.170	0.305
Pseudo-second order (PSO)	q_m (mg/g)	2.49	2.51	3.27
	K_2 1/[(g(mg/min)]	0.099	0.068	0.045
$q_t = t.k_2.q_e^2/(1+k_2.q_e)$	R^2	0.974	0.974	0.962
	RSE	0.093	0.116	0.183
Intra-particle diffusion	K_d (mg/(g.$min^{0.5}$))	0.268	0.384	0.307
	C	2.02	1.95	2.29
	R^2	0.9021	0.850	0.997
Elovich	β (mg/g)	3.28	2.20	1.96
	α (mg/g.min)	9.04	2.41	2.25
	R^2	0.976	0.914	0.988
	RSE	0.090	0.149	0.100

5.4 THERMODYNAMIC STUDIES

The thermodynamic parameters such as the Gibb's energy (ΔG^o), enthalpy change (ΔH^o) and entropy change (ΔS^o) were calculated and are portrayed in Table 5.6. All the Gibb's energy (ΔG^o) values were found to be negative for all the prepared adsorbents at the three different temperatures. These negative values signified a spontaneous nature of the adsorption process. The spontaneity of the adsorbents did not follow any trend however, AC-Fe_3O_4 and AC-Fe_3O_4-SiO_2 were highly spontaneous at 298 K followed by 318 K as compared to 308 K. For AC-Fe_3O_4-SiO_2-PEI showed decrease in ΔG^o as temperature was increased. This displays that the

uptake of Cr(VI) ions by AC-Fe_3O_4-SiO_2-PEI were facilitated by higher temperatures. Negative ΔG^o values indicates more energetically favorable adsorption (Tran et al., 2016). Similarly, Zhao et al. (2016) presented a trend of ΔG^o decreasing with increased temperatures concluding that the uptake of Cr(VI) was temperature dependent. The positive enthalpy change (ΔH^o) represents an endothermic reaction. Positive ΔH^o depicts that the adsorption process adsorbs heat energy from its surroundings therefore displaying chemisorption processes (Tran et al., 2016). Chemisorption has been reported to occur over high activating energies (>400 kJ) and increased temperatures (Qiu et al., 2015). The ΔS^o value describes the randomness with $\Delta S^o > 0$ being less random and $\Delta S^o < 0$ being more random. The positive entropy change (ΔS^o) reflected increased randomness between the adsorbent and the solution. The ΔS^o can also be used to depict whether the adsorption process follows an associative or dissociative mechanism which can be concluded based on the positive or negative ΔS^o values (Tran et al., 2016). The positive ΔS^o in this aspect depicts that the adsorption process displayed a dissociative mechanism.

Table 5.6: Thermodynamics parameters of AC-Fe_3O_4, AC-Fe_3O_4-SiO_2 and AC-Fe_3O_4-SiO_2-PEI at different temperatures.

Adsorbents	T (K)	Ln(K_c)	$\Delta G°$(J/mol)	$\Delta H°$(J/mol)	$\Delta S°$
AC-Fe_3O_4	298	4.29	-12121.3	45717.2	114.13
	308	3.79	-9699.53		
	318	3.74	-9897.07		
AC-Fe_3O_4-SiO_2	298	3.42	-8468.66	12497.6	1.6909
	308	3.01	-7828.43		
	318	3.11	-8210.11		
AC-Fe_3O_4-SiO_2-PEI	298	1.32	-3217	5482	29.11
	308	1.30	-3318		
	318	1.46	-3864		

5.5 COMPARISON OF ADSORPTION CAPACITIES

The adsorption capacity is one of the important parameters used to judge the performance of adsorbents. In this study, the adsorption capacities of AC-Fe_3O_4, AC-Fe_3O_4-SiO_2 and AC-Fe_3O_4-SiO_2-PEI were compared to literature values as displayed in Table 5.7. The results should be treated with caution because the different preparation and modification methods adopted for each adsorbent make it impossible to do a direct comparison. However, it can be observed from Table 5.7 that most studies reported optimum performance in acidic media (pH 1-5). In acidic media, more of the Cr(VI) are removed due to increased ion exchange and electrostatic interactions between the negatively charged Cr ion species and the protonated functional groups on the surface of the adsorbent (Niazi et al., 2018).

In the present study, AC-Fe_3O_4 had highest adsorption capacity as compared to the AC-Fe_3O_4-SiO_2 and AC-Fe_3O_4-SiO_2-PEI probably due to the involvement of Fe^{2+}/Fe^{3+} playing dual roles of electrostatic attraction of Cr(VI) and reduction of Cr(VI) to Cr(III). This could have been made possible by the fact that in AC-Fe_3O_4 the Fe^{2+}/Fe^{3+} species were in/ near the surface proximity allowing for faster reaction with Cr(VI), while for AC-Fe_3O_4-SiO_2 and AC-Fe_3O_4-SiO_2-PEI the iron species were shielded by a layer of silica. Although PEI is rich in amine groups which are favorable for removal uptake of Cr(VI) through electrostatic attraction, it has been reported that high loading of PEI may reduce the adsorption sites on the adsorbent's surface further resulting in reduced adsorption capacities (Geng et al., 2019). Maybe that is the reason why lower adsorption capacities were observed with PEI loaded adsorbents as compared to magnetic adsorbents. Nonetheless, the adsorption capacities reported in the present study were similar to those reported by Zhong et al. (2018) and Larraza et al. (2012). Table 5.7 also reveals that there still existed a challenge in producing biocarbon-based adsorbents with high adsorption capacity for Cr(VI), meaning that research is needed to explore other possible carbon-based adsorbents.

Table 5.7: Comparison of adsorption capacities of Cr(VI) by different adsorbents as to AC-Fe_3O_4, AC-Fe_3O_4-SiO_2 and AC-Fe_3O_4-SiO_2-PEI.

Adsorbents	**pH**	**Co (mg/L)**	**q_m (mg/g)**	**References**
Magnetic biochar	3	100	8.35	Zhong et al., 2018
MBC/PPy	3	10	19.23	Yang et al., 2018
Magnetic biochar (MMABC)	3	10	25.27	Zhang et al., 2018
Fe_3O_4-PEI800-MNT	1-9	10-25	8.77	Larraza et al., 2012
Fe_3O_4-PEI25000-MNT	1-9	10-25	7.69	Larraza et al., 2012
AC-Fe_3O_4	3	5	6.62	This study
AC-Fe_3O_4-SiO_2	1	5	3.92	This study
AC-Fe_3O_4-SiO_2-PEI	1	5	5.48	This study

CHAPTER 6:
CONCLUSION AND RECOMMENDATIONS

6.1 CONCLUSIONS

Iron oxide functionalized polyethyleneimine coated activated carbon-silica composites were successfully synthesized and characterized using FTIR, TGA, BET, elemental analysis, XRD, SEM, EDS, XPS, zeta potential and TEM. These characterization techniques were employed to study the surface morphology, porosity, chemical and physical changes on the surface of the prepared adsorbents. Elemental analysis revealed that the %C and %H decreased as Fe_3O_4 nanoparticles were functionalized on the surface of the AC due tp high atomic mass ratio of FE and O relative to C and H. The % residual increased with 38% confirming the presence of Fe and O as other elements present on the surface of the AC. The %C and %H increased as SiO_2 was incorporated on the surface of the AC-Fe_3O_4 attributed to the attachment of CH_3-CH_2- chains of the TEOS. Increased %N of 3% and %H of 6% as the PEI was attached on the surface of the AC-Fe_3O_4 was attributed to the attachment of NH_2 branches of the PEI.

BET revealed that the surface area decreased as functionalization occurred on the surface of the AC. This was attributed to deposits of Fe_3O_4, SiO_2, GPS and PEI into the pores of the AC. This was supported by decreased pore volumes with each functionalization step. The AC-Fe_3O_4-PEI displayed surface areas below 1 nm attributed to complete blockage of the AC pores by the

gelatinous character of the PEI. All the pore sizes were above 2nm displaying mesoporous character of the adsorbents.

SEM displayed change in morphology as functionalization occurred. The AC-KOH displayed irregular shapes with large pores of the AC. AC-Fe_3O_4 displayed small white deposits inside the large pores which were attributed to those of the precipitated Fe_3O_4. As SiO_2 was incorporated to the surface of the AC-Fe_3O_4, a more amorphous surface was displayed. A more amorphous structure was displayed for AC-Fe_3O_4-SiO_2-PEI with almost no pores visible predicting that the porous structure of the AC was completely covered up by the gelatinous PEI.

The FTIR displayed characteristic peaks at 1054, 791, 533 cm^{-1} attributed to those of the symmetric Si-OH, asymmetric Si-O-Si and vibrating stretches of the Fe-O respectively. The primary amine groups were displayed at 1092 and 1030 cm^{-1}. The presence of these peaks indicates successful attachment of the aimed ligands.

The XRD exhibited 5 characteristic peaks at 2Ɵ at 30°, 35°, 48° and 65° related to 220, 311, 400, 511 and 440 planes of the Bragg's reflections. These characteristic peaks correlated those of the magnetite reference of a job card 00-019-0629 pointing to efficacious attachment of the Fe_3O_4 nanoparticles. As hydroxylation occurred, the intensity of characteristic peaks decreased suggesting that the adsorbent lost its crystallinity. The AC-Fe_3O_4-SiO_2-PEI displayed one peak at 20° attributed to the amorphous character of the PEI. The XPS confirmed the presence of Fe, Si, C, O and N atoms in the sample, signaling the successful attachment of the ligands to the active carbon. However, the deconvolution of N peak revealed presence of azides and cyanide nitrogen

instead of amines from PEI. Further interrogative experiments to understand this transformation will be undertaken.

The batch adsorption process was best fitted to Langmuir adsorption model based on the high R^2 values and low RSE values obtained indicating that the adsorption process occurred over a monolayer with homogenous coverage. Lastly, it was difficult to conclusively decide whether any of the chemisorption or physisorption mechanism was dominant because the lower pore size and surface pointed out to the possibility of physisorption interaction while the kinetics data and thermodynamic data pointed out to chemisorption. The thermodynamics parameters also revealed that the adsorption process was of spontaneous nature and endothermic. The prepared activated carbon adsorbents demonstrated promising adsorption capacities and can be used as adsorbents for the removal of Cr(VI) from water.

6.2 RECOMMENDATIONS

- Different chemical reagents such as HNO_3 or $KMnO_4$ can be used for pre-treatment of AC for improved modification.
- Different acid solutions may be used for hydroxylation which are less harsh compared to the piranha solution for grafting of OH- groups on the surface of the adsorbent which will allow ease attachment of different ligands.
- Varying the AC:PEI ratio where the AC is larger than the PEI to provide more porous, larger surface preventing total blockage by PEI.
- Using cross-linkers for attachment of amino groups.
- Application to real world samples using solid phase microextraction technique.

REFERENCES

AÇıKYıLDıZ, M., GÜRSES, A. & KARACA, S. 2014. Preparation and characterization of activated carbon from plant wastes with chemical activation. *Microporous and Mesoporous Materials,* 198**,** 45-49.

ADIO, S. O., ASIF, M., MOHAMMED, A.-R. I., BAIG, N., AL-ARFAJ, A. A. & SALEH, T. A. 2019. Poly (amidoxime) modified magnetic activated carbon for chromium and thallium adsorption: Statistical analysis and regeneration. *Process Safety and Environmental Protection,* 121**,** 254-262.

AIGBE, U. O., DAS, R., HO, W. H., SRINIVASU, V. & MAITY, A. 2018. A novel method for removal of Cr(VI) using polypyrrole magnetic nanocomposite in the presence of unsteady magnetic fields. *Separation and Purification Technology,* 194**,** 377-387.

AL-GHOUTI, M. A. & DA'ANA, D. A. 2020. Guidelines for the use and interpretation of adsorption isotherm models: A review. *J Hazard Mater,* 393**,** 122383.

ALTUNAY, N., YILDIRIM, E. & GURKAN, R. 2018. Extraction and preconcentration of trace Al and Cr from vegetable samples by vortex-assisted ionic liquid-based dispersive liquid-liquid microextraction prior to atomic absorption spectrometric determination. *Food Chem,* 245**,** 586-594.

BAI, B., MI, X., XIANG, X., HEIDEN, P. A. & HELDT, C. L. 2013. Non-enveloped virus reduction with quaternized chitosan nanofibers containing graphene. *Carbohydr Res,* 380**,** 137-42.

BETZY, N. T. & GEORGE, S. C. 2015. Production of activated carbon from natural sources. *iMedPub Journals,* 1**,** 1-5.

CAI, W., LI, Z., WEI, J. & LIU, Y. 2018. Synthesis of peanut shell based magnetic activated carbon with excellent adsorption performance towards electroplating wastewater. *Chemical Engineering Research and Design,* 140**,** 23-32.

CHEN, Q., ZHU, R., ZHU, Y., LIU, J., ZHU, L., MA, L. & CHEN, M. 2016. Adsorption of polyhydroxy fullerene on polyethylenimine-modified montmorillonite. *Applied Clay Science,* 132-133**,** 412-418.

CHEN, S., WANG, J., WU, Z., DENG, Q., TU, W., DAI, G., ZENG, Z. & DENG, S. 2018. Enhanced Cr(VI) removal by polyethylenimine- and phosphorus-codoped hierarchical porous carbons. *J Colloid Interface Sci,* 523**,** 110-120.

CORAZZA, M. Z., SOMERA, B. F., SEGATELLI, M. G. & TARLEY, C. R. 2012. Grafting 3-mercaptopropyl trimethoxysilane on multi-walled carbon nanotubes surface for improving on-line cadmium(II) preconcentration from water samples. *J Hazard Mater,* 243**,** 326-33.

DEMARCHI, C. A., MICHEL, B. S., NEDELKO, N., ŚLAWSKA-WANIEWSKA, A., DŁUŻEWSKI, P., KALETA, A., MINIKAYEV, R., STRACHOWSKI, T., LIPIŃSKA, L., DAL MAGRO, J. & RODRIGUES, C. A. 2019. Preparation, characterization, and application of magnetic activated carbon from termite feces for the adsorption of Cr(VI) from aqueous solutions. *Powder Technology,* 354**,** 432-441.

DOS SANTOS, C. S. L., MIRANDA REIS, M. H., CARDOSO, V. L. & DE RESENDE, M. M. 2019. Electrodialysis for removal of chromium (VI) from effluent: Analysis of concentrated solution saturation. *Journal of Environmental Chemical Engineering,* 7.

DUTTA, D. P. & NATH, S. 2018. Low cost synthesis of SiO2/C nanocomposite from corn cobs and its adsorption of uranium (VI), chromium (VI) and cationic dyes from wastewater. *Journal of Molecular Liquids,* 269**,** 140-151.

EL-SAYED, M. & NADA, A. A. 2017. Polyethylenimine −functionalized amorphous carbon fabricated from oil palm leaves as a novel adsorbent for Cr(VI) and Pb(II) from aqueous solution. *Journal of Water Process Engineering,* 16**,** 296-308.

FATEHI, M. H., SHAYEGAN, J., ZABIHI, M. & GOODARZNIA, I. 2017. Functionalized magnetic nanoparticles supported on activated carbon for adsorption of Pb(II) and Cr(VI) ions from saline solutions. *Journal of Environmental Chemical Engineering,* 5**,** 1754-1762.

FELLENZ, N., PEREZ-ALONSO, F. J., MARTIN, P. P., GARCÍA-FIERRO, J. L., BENGOA, J. F., MARCHETTI, S. G. & ROJAS, S. 2017. Chromium (VI) removal from water by means of adsorption-reduction at the surface of amino-functionalized MCM-41 sorbents. *Microporous and Mesoporous Materials,* 239**,** 138-146.

FENG, S. H. & LI, G. H. 2017. Hydrothermal and Solvothermal Syntheses. *Modern Inorganic Synthetic Chemistry.*

GENG, J., YIN, Y., LIANG, Q., ZHU, Z. & LUO, H. 2019. Polyethyleneimine cross-linked graphene oxide for removing hazardous hexavalent chromium: Adsorption performance and mechanism. *Chemical Engineering Journal,* 361**,** 1497-1510.

GOTTIPATI, R. & MISHRA, S. 2016. Preparation of microporous activated carbon from Aegle Marmelos fruit shell and its application in removal of chromium(VI) from aqueous phase. *Journal of Industrial and Engineering Chemistry,* 36**,** 355-363.

HAN, Y., CAO, X., OUYANG, X., SOHI, S. P. & CHEN, J. 2016. Adsorption kinetics of magnetic biochar derived from peanut hull on removal of Cr (VI) from aqueous solution: Effects of production conditions and particle size. *Chemosphere,* 145**,** 336-41.

HE, R., YUAN, X., HUANG, Z., WANG, H., JIANG, L., HUANG, J., TAN, M. & LI, H. 2019. Activated biochar with iron-loading and its application in removing Cr (VI) from aqueous solution. *Colloids and Surfaces A: Physicochemical and Engineering Aspects,* 579.

HLUNGWANE, L., VILJOEN, E. L. & PAKADE, V. E. 2017. Macadamia nutshells-derived activated carbon and attapulgite clay combination for synergistic removal of Cr(VI) and Cr(III). *Adsorption Science & Technology,* 36**,** 713-731.

HU, Y. 2017. Removal of chromium(VI) from aqueous solutions by electrochemical reduction–precipitation. *International Journal of Electrochemical Science***,** 11387-11396.

JAOUADI, M., HBAIEB, S., GUEDIDI, H., REINERT, L., AMDOUNI, N. & DUCLAUX, L. 2017. Preparation and characterization of carbons from β-cyclodextrin dehydration and from olive pomace activation and their application for boron adsorption. *Journal of Saudi Chemical Society,* 21**,** 822-829.

JIANG, X., AN, Q.-D., XIAO, Z.-Y., ZHAI, S.-R. & SHI, Z. 2018a. Mussel-inspired surface modification of untreated wasted husks with stable polydopamine/polyethylenimine for efficient continuous Cr(VI) removal. *Materials Research Bulletin,* 102**,** 218-225.

JIANG, Y., LIU, Z., ZENG, G., LIU, Y., SHAO, B., LI, Z., LIU, Y., ZHANG, W. & HE, Q. 2018b. Polyaniline-based adsorbents for removal of hexavalent chromium from aqueous solution: a mini review. *Environ Sci Pollut Res Int,* 25**,** 6158-6174.

KONONOVA, O. N., BRYUZGINA, G. L., APCHITAEVA, O. V. & KONONOV, Y. S. 2019. Ion exchange recovery of chromium (VI) and manganese (II) from aqueous solutions. *Arabian Journal of Chemistry,* 12**,** 2713-2720.

KUMAR, A. & JENA, H. M. 2017. Adsorption of Cr(VI) from aqueous solution by prepared high surface area activated carbon from Fox nutshell by chemical activation with H 3 PO 4. *Journal of Environmental Chemical Engineering,* 5**,** 2032-2041.

LAWRENCE AROCKIASAMY, D., ALHOSHAN, M., ALAM, J., MUTHUMAREESWARAN, M. R., FIGOLI, A. & ARUN KUMAR, S. 2017. Separation of proteins and antifouling properties of polyphenylsulfone based mixed matrix hollow fiber membranes. *Separation and Purification Technology,* 174**,** 529-543.

LEE, J., PARK, J. A., KIM, H. G., LEE, J. H., CHO, S. H., CHOI, K., JUNG, K. W., LEE, S. Y. & CHOI, J. W. 2020. Most suitable amino silane molecules for surface functionalization of graphene oxide toward hexavalent chromium adsorption. *Chemosphere,* 251**,** 126387.

LEE, M. Y., LEE, J. H., CHUNG, J. W. & KWAK, S. Y. 2018. Hydrophilic and positively charged polyethylenimine-functionalized mesoporous magnetic clusters for highly efficient removal of Pb(II) and Cr(VI) from wastewater. *J Environ Manage,* 206**,** 740-748.

LESAOANA, M., MLABA, R. P. V., MTUNZI, F. M., KLINK, M. J., EJIDIKE, P. & PAKADE, V. E. 2019. Influence of inorganic acid modification on Cr(VI) adsorption performance and the physicochemical properties of activated carbon. *South African Journal of Chemical Engineering,* 28**,** 8-18.

LI, L., FAN, L., SUN, M., QIU, H., LI, X., DUAN, H. & LUO, C. 2013. Adsorbent for chromium removal based on graphene oxide functionalized with magnetic cyclodextrin-chitosan. *Colloids Surf B Biointerfaces,* 107**,** 76-83.

LI, N., CHEN, J. & SHI, Y. P. 2017. Magnetic polyethyleneimine functionalized reduced graphene oxide as a novel magnetic solid-phase extraction adsorbent for the determination of polar acidic herbicides in rice. *Anal Chim Acta,* 949**,** 23-34.

LIANG, Q., GENG, J., LUO, H., FANG, W. & YIN, Y. 2017. Fast and selective removal of Cr(VI) from aqueous solutions by a novel magnetic Cr(VI) ion-imprinted polymer. *Journal of Molecular Liquids,* 248**,** 767-774.

LIU, H., ZHANG, F. & PENG, Z. 2019a. Adsorption mechanism of Cr(VI) onto GO/PAMAMs composites. *Sci Rep,* 9**,** 3663.

LIU, X., TIAN, J., LI, Y., SUN, N., MI, S., XIE, Y. & CHEN, Z. 2019b. Enhanced dyes adsorption from wastewater via Fe3O4 nanoparticles functionalized activated carbon. *J Hazard Mater,* 373**,** 397-407.

LIU, Y.-P., HU, S., WEN, Q., MA, Y.-L., JIANG, Z.-H., TANG, J.-Y. & FU, Y.-H. 2018. Novel γ-lactone derivatives from Trigonostemon heterophyllus with their potential antiproliferative activities. *Bioorganic Chemistry,* 79**,** 107-110.

LUO, T., TIAN, X., YANG, C., LUO, W., NIE, Y. & WANG, Y. 2017. Polyethylenimine-Functionalized Corn Bract, an Agricultural Waste Material, for Efficient Removal and Recovery of Cr(VI) from Aqueous Solution. *J Agric Food Chem,* 65**,** 7153-7158.

MASHILE, G. P., MPUPA, A., NQOMBOLO, A., DIMPE, K. M. & NOMNGONGO, P. N. 2020. Recyclable magnetic waste tyre activated carbon-chitosan composite as an effective

adsorbent rapid and simultaneous removal of methylparaben and propylparaben from aqueous solution and wastewater. *Journal of Water Process Engineering,* 33.

MNIF, A., BEJAOUI, I., MOUELHI, M. & HAMROUNI, B. 2017. Hexavalent Chromium Removal from Model Water and Car Shock Absorber Factory Effluent by Nanofiltration and Reverse Osmosis Membrane. *Int J Anal Chem,* 2017**,** 7415708.

NIAZI, L., LASHANIZADEGAN, A. & SHARIFIFARD, H. 2018. Chestnut oak shells activated carbon: Preparation, characterization and application for Cr (VI) removal from dilute aqueous solutions. *Journal of Cleaner Production,* 185**,** 554-561.

NOROUZI, E., KAMANKESH, M., MOHAMMADI, A. & ATTARAN, A. 2018a. Acrylamide in bread samples: Determining using ultrasonic-assisted extraction and microextraction method followed by gas chromatography-mass spectrometry. *Journal of Cereal Science,* 79**,** 1-5.

NOROUZI, S., HEIDARI, M., ALIPOUR, V., RAHMANIAN, O., FAZLZADEH, M., MOHAMMADI-MOGHADAM, F., NOURMORADI, H., GOUDARZI, B. & DINDARLOO, K. 2018b. Preparation, characterization and Cr(VI) adsorption evaluation of NaOH-activated carbon produced from Date Press Cake; an agro-industrial waste. *Bioresour Technol,* 258**,** 48-56.

NTULI, T. D. & PAKADE, V. E. 2019. Hexavalent chromium removal by polyacrylic acid-grafted Macadamia nutshell powder through adsorption–reduction mechanism: Adsorption isotherms, kinetics and thermodynamics. *Chemical Engineering Communications,* 207**,** 279-294.

OWLAD, M., AROUA, M. K. & WAN DAUD, W. M. 2010. Hexavalent chromium adsorption on impregnated palm shell activated carbon with polyethyleneimine. *Bioresour Technol,* 101**,** 5098-103.

PAKADE, V. E., MAREMENI, L. C., NTULI, T. D. & TAVENGWA, N. T. 2016a. Application of quaternized activated carbon derived from Macadamia nutshells for the removal of hexavalent chromium from aqueous solutions. *South African Journal of Chemistry,* 69.

PAKADE, V. E., NTULI, T. D. & OFOMAJA, A. E. 2016b. Biosorption of hexavalent chromium from aqueous solutions by Macadamia nutshell powder. *Applied Water Science,* 7**,** 3015-3030.

PARLAYICI, S., ESKIZEYBEK, V., AVCı, A. & PEHLIVAN, E. 2015. Removal of chromium (VI) using activated carbon-supported-functionalized carbon nanotubes. *Journal of Nanostructure in Chemistry,* 5**,** 255-263.

PRAJAPATI, A. K., DAS, S. & MONDAL, M. K. 2020. Exhaustive studies on toxic Cr(VI) removal mechanism from aqueous solution using activated carbon of Aloe vera waste leaves. *Journal of Molecular Liquids,* 307.

QIU, B., WANG, Y., SUN, D., WANG, Q., ZHANG, X., WEEKS, B. L., O'CONNOR, R., HUANG, X., WEI, S. & GUO, Z. 2015. Cr(vi) removal by magnetic carbon nanocomposites derived from cellulose at different carbonization temperatures. *Journal of Materials Chemistry A,* 3**,** 9817-9825.

QIU, W., YANG, D., XU, J., HONG, B., JIN, H., JIN, D., PENG, X., LI, J., GE, H. & WANG, X. 2016. Efficient removal of Cr(VI) by magnetically separable CoFe2O4/activated carbon composite. *Journal of Alloys and Compounds,* 678**,** 179-184.

RAI, M. K., SHAHI, G., MEENA, V., MEENA, R., CHAKRABORTY, S., SINGH, R. S. & RAI, B. N. 2016. Removal of hexavalent chromium Cr (VI) using activated carbon prepared from mango kernel activated with H3PO4. *Resource-Efficient Technologies,* 2**,** S63-S70.

REN, L., LIN, H., MENG, F. & ZHANG, F. 2019. One-step solvothermal synthesis of Fe3O4@Carbon composites and their application in removing of Cr (VI) and Congo red. *Ceramics International,* 45**,** 9646-9652.

ROOZBETH, H. H., ARASH, A.-N., WAN, M. A. W. D. & JSAHU, J. N. 2013. Preparation and Characterization of Activated Carbon fromApple Waste by Microwave-Assisted Phosphoric Acid Activation: Application in Methylene Blue Adsorption. *BioResources,* 8**,** 2950-2966.

S, S. & P, S. K. 2018. Influence of ultrasonic waves on preparation of active carbon from coffee waste for the reclamation of effluents containing Cr(VI) ions. *Journal of Industrial and Engineering Chemistry,* 60**,** 418-430.

SETHY, T. R. & SAHOO, P. K. 2019. Highly toxic Cr (VI) adsorption by (chitosan-g-PMMA)/silica bionanocomposite prepared via emulsifier-free emulsion polymerisation. *Int J Biol Macromol,* 122**,** 1184-1190.

SHI, S., YANG, J., LIANG, S., LI, M., GAN, Q., XIAO, K. & HU, J. 2018. Enhanced Cr(VI) removal from acidic solutions using biochar modified by Fe3O4@SiO2-NH2 particles. *Science of the Total Environment,* 628-629**,** 499-508.

SINGH, S. & PRASAD, S. M. 2019. Management of chromium (VI) toxicity by calcium and sulfur in tomato and brinjal: Implication of nitric oxide. *J Hazard Mater,* 373**,** 212-223.

SOLGI, M., NAJIB, T., AHMADNEJAD, S. & NASERNEJAD, B. 2017. Synthesis and characterization of novel activated carbon from Medlar seed for chromium removal: Experimental analysis and modeling with artificial neural network and support vector regression. *Resource-Efficient Technologies,* 3**,** 236-248.

SUN, X., YANG, L., LI, Q., ZHAO, J., LI, X., WANG, X. & LIU, H. 2014. Amino-functionalized magnetic cellulose nanocomposite as adsorbent for removal of Cr(VI): Synthesis and adsorption studies. *Chemical Engineering Journal,* 241**,** 175-183.

TA, T. K. H., TRINH, M.-T., LONG, N. V., NGUYEN, T. T. M., NGUYEN, T. L. T., THUOC, T. L., PHAN, B. T., MOTT, D., MAENOSONO, S., TRAN-VAN, H. & LE, V. H. 2016. Synthesis and surface functionalization of Fe 3 O 4 -SiO 2 core-shell nanoparticles with 3-glycidoxypropyltrimethoxysilane and 1,1′-carbonyldiimidazole for bio-applications. *Colloids and Surfaces A: Physicochemical and Engineering Aspects,* 504**,** 376-383.

TASLIM, BANI, O., IRIANY, ARYANI, N. & KABAN, G. S. 2018. Preparation of Activated Carbon-Based Catalyst from Candlenut Shell Impregnated with KOH for Biodiesel Production. *Key Engineering Materials,* 777**,** 262-267.

TRAN, H. N., YOU, S.-J. & CHAO, H.-P. 2016. Thermodynamic parameters of cadmium adsorption onto orange peel calculated from various methods: A comparison study. *Journal of Environmental Chemical Engineering,* 4**,** 2671-2682.

TRAN, H. N., YOU, S. J., HOSSEINI-BANDEGHARAEI, A. & CHAO, H. P. 2017. Mistakes and inconsistencies regarding adsorption of contaminants from aqueous solutions: A critical review. *Water Res,* 120**,** 88-116.

VALENTIN-REYES, J., GARCIA-REYES, R. B., GARCIA-GONZALEZ, A., SOTO-REGALADO, E. & CERINO-CORDOVA, F. 2019. Adsorption mechanisms of hexavalent chromium from aqueous solutions on modified activated carbons. *J Environ Manage,* 236**,** 815-822.

WANG, J. & GUO, X. 2020. Adsorption kinetic models: Physical meanings, applications, and solving methods. *J Hazard Mater,* 390**,** 122156.

WANG, X., XU, J., LIU, J., LIU, J., XIA, F., WANG, C., DAHLGREN, R. A. & LIU, W. 2020a. Mechanism of Cr(VI) removal by magnetic greigite/biochar composites. *Sci Total Environ,* 700**,** 134414.

WANG, Y., YANG, Q., CHEN, J., YANG, J., ZHANG, Y., CHEN, Y., LI, X., DU, W., LIANG, A., HO, S. H. & CHANG, J. S. 2020b. Adsorption behavior of Cr(VI) by magnetically modified Enteromorpha prolifera based biochar and the toxicity analysis. *J Hazard Mater,* 395**,** 122658.

YAN, Y., AN, Q., XIAO, Z., ZHENG, W. & ZHAI, S. 2017. Flexible core-shell/bead-like alginate@PEI with exceptional adsorption capacity, recycling performance toward batch and column sorption of Cr(VI). *Chemical Engineering Journal,* 313**,** 475-486.

YANG, Y., CHEN, N., FENG, C., LI, M. & GAO, Y. 2018. Chromium removal using a magnetic corncob biochar/polypyrrole composite by adsorption combined with reduction: Reaction pathway and contribution degree. *Colloids and Surfaces A: Physicochemical and Engineering Aspects,* 556**,** 201-209.

YU, J., JIANG, C., GUAN, Q., NING, P., GU, J., CHEN, Q., ZHANG, J. & MIAO, R. 2018. Enhanced removal of Cr(VI) from aqueous solution by supported ZnO nanoparticles on biochar derived from waste water hyacinth. *Chemosphere,* 195**,** 632-640.

ZHANG, S., WANG, Z., CHEN, H., KAI, C., JIANG, M., WANG, Q. & ZHOU, Z. 2018. Polyethylenimine functionalized Fe3O4/steam-exploded rice straw composite as an efficient adsorbent for Cr(VI) removal. *Applied Surface Science,* 440**,** 1277-1285.

ZHAO, D., GAO, X., WU, C., XIE, R., FENG, S. & CHEN, C. 2016. Facile preparation of amino functionalized graphene oxide decorated with Fe3O4 nanoparticles for the adsorption of Cr(VI). *Applied Surface Science,* 384**,** 1-9.